University of Canterbury

Masters Thesis

Calcium Dynamics and Wave Propagation in Coupled Cells

Author:
Allanah Kenny

Supervisors:
Prof. Tim David
Dr. Michael J. Plank

A thesis submitted in fulfillment of the requirements for the degree of Masters in Mathematics

February 29, 2016

Contents

Acknowledgements

First of all thank you to the University of Canterbury and UC HPC for providing me with the funds to go through with all this! Thank you to my supervisors Tim David and Mike Plank – this wouldn't have been possible without you both. Thank you to my wonderful research group at UC HPC: Kathi, Elshin, Jai, Christine, Tim, Michelle, Stewart, Kon. Thank you to all the interns who have come and gone: Philip, Eva, Moritz, Joerik, Dominic, Jan. Thank you to the UC HPC team who put up with us students everyday: Angela, Dan, Francois, Robert, Sung, Vlad, Tony. Thank you to anyone else who I may have forgotten. And finally thank you to my family, friends and partner Valentin, for your continued support of my neverending study.
Thank you!

Abstract

Intercellular waves of calcium (Ca^{2+}) are an important signalling mechanism in a wide variety of cells within the body, crucial for cellular coordination and control. In particular the Ca^{2+} concentration within smooth muscle cells (SMCs) lining the blood vessel walls controls the cell dilation and contraction and thus the vessel radius. The process of functional hyperaemia by which neuronal activity results in a localised response of increased blood flow via the dilation of SMCs is associated with multiple pathologies such as cortical spreading depression (CSD). This process can be modelled by a 'neurovascular unit (NVU)' containing a neuron, astrocyte, and the SMC and endothelial cell (EC) within the vessel wall.

Our research consists of modelling the Ca^{2+} dynamics of a both a single SMC and two coupled SMCs (via an intercellular Ca^{2+} flux) mainly with the minimal nonspatial Goldbeter et al. (1990) cell model. This is compared with the more complex model of a SMC/EC 'unit' which also includes the influence of neuronal stimulation on the SMC. The Ca^{2+} dynamics of both models are found to be similar in structure: the system will be either excitable, nonexcitable or oscillatory depending on a model dependent parameter controlling the rate of inotisol trisphosphate (IP_3) induced Ca^{2+} release into the cell. However the SMC/EC model also produces small amplitude oscillations and bistability when neuronal stimulation is high and the model parameter is low. The behaviour of a coupled cell system is seemingly model independent: in particular an excitable coupled with an oscillatory or two nonidentical coupled oscillatory cells will exhibit qualitatively different behaviour when weakly coupled such as variable amplitude oscillations.

The formation and propagation of Ca^{2+} waves are simulated by the Goldbeter et al. (1990) model in a two dimensional (2D) spatial medium; spatial curvature is then introduced by simulating the model on a torus. When the local dynamics of the medium are spatially constant a new wave solution in the form of a stable wave segment when there is some gradient in Gaussian curvature. When the local dynamics of the medium are spatially varied, spiral waves or apparent spatiotemporal chaos are produced when the rate of diffusion is low and either the surface is strongly curved or the initial conditions (ICs) of the medium are sufficiently inhomogeneous. Based on the similarities in the nonspatial results the spatial Goldbeter et al. (1990) model could provide insight into the behaviour of the corresponding complex spatial SMC/EC model.

Abbreviations

Ca^{2+} calcium

IP_3 inotisol trisphosphate

K^+ potassium

Na^+ sodium

2D two dimensional

AC astrocyte

ATP adenosine triphosphate

BC boundary condition

BK big potassium

BT Bogdanov-Takens

CBF cerebral blood flow

CICR Ca^{2+} induced Ca^{2+} release

CP Cusp

CSD cortical spreading depression

EC endothelial cell

ER endoplasmic reticulum

FHN FitzHugh-Nagumo

FP fixed point

GHK Goldman Hodgkin Katz

IC initial condition

KIR inward rectifying potassium

LC limit cycle

LP limit point

LPC limit point cycle

MPI Message Passing Interface

NE neuron

NVC neurovascular coupling

NVU neurovascular unit

ODE ordinary differential equation

PD Period Doubling

PDE partial differential equation

PLC phospholipase-C

PVS perivascular space

RHS right hand side

SC synaptic cleft

SMC smooth muscle cell

SR sarcoplasmic reticulum

VOCC voltage operated Ca^{2+} channel

VTK Visualisation Toolkit

Chapter 1

Introduction

Intracellular and intercellular calcium (Ca^{2+}) is an important signalling messenger in a wide variety of cells. Many cells in the body are known to exhibit periodic increases in Ca^{2+} concentration level (Wilkins and Sneyd, 1998), otherwise known as Ca^{2+} oscillations. In addition, these cells are also known to exhibit singular 'spikes' in Ca^{2+} in response to external stimulation; this is known as excitable behaviour (Wilkins and Sneyd, 1998). A population of cells, in particular smooth muscle cells (SMCs) lining the arterial wall, are known to support an oscillating wave of Ca^{2+} propagating through the cell population referred to as a 'travelling wave' (Sneyd and Atri, 1993). When a population of cells are known to exhibit excitable behaviour or Ca^{2+} oscillations they are able to support such a travelling wave.

Propagating Ca^{2+} waves through the arterial wall via SMCs are an important signalling mechanism (Meyer and Stryer, 1988) and evidence exists that intracellular and intercellular Ca^{2+} signalling is one of the crucial methods of cellular coordination and control (Wilkins and Sneyd, 1998). For example it is known that synchronised oscillations of Ca^{2+} in a population of SMCs will induce vasomotion, the rhymthic dilation and contraction of the blood vessel wall via the relaxation and contraction of the SMCs. The contraction of a SMC is caused by an increase in Ca^{2+} concentration via the process of Ca^{2+} initiated formation of crossbridges between the myosin and actin filaments of the cell (Hai and Murphy, 1988).

The cerebral cortex, a highly complex component of the human brain composed of folded grey matter, is composed mainly of neurons, glial cells such as astrocytes, and a vast network of blood vessels that provide oxygen and glucose throughout the brain tissue. These blood vessels are composed of a thin layer of endothelial cells (ECs) on the interior surface and an outer layer of SMCs controlling the vessel radius. The process of functional hyperaemia or 'neurovascular coupling (NVC)' is the self regulation of blood flow in the brain; specfically, the relationship between neural activity and the local increase in blood flow to that area caused by dilation in the blood vessels via the SMCs (which is in

turn due to a decrease in Ca^{2+} concentration within the cell). This coupling is achieved through the intercellular communication through ions such as Ca^{2+} and potassium (K^{+}) and signalling molecules such as glutamate and inotisol trisphosphate (IP_3) between a group of cells known as a neurovascular unit (NVU): the neuron, astrocyte, SMC and EC.

Propagating Ca^{2+} waves through a population of SMCs may play a role in pathologies associated with impaired functional hyperaemia such as cortical spreading depression (CSD), migraine, and stroke (Girouard and Iadecola, 2006), as the SMCs effectively control the local supply of oxygen and glucose necessary for cellular function.

The dynamics of Ca^{2+} concentration in a single and two coupled SMC system are investigated in order to further our understanding of the influence that one cell has on another adjacent cell, and consequently the effect their interaction has on the individual cell dynamics. These cells are modelled by a selection of three simple minimal Ca^{2+} cell models based on different fundemental cell mechanisms by Goldbeter et al. (1990), Meyer and Stryer (1988) and Gonzalez-Fernandez and Ermentrout (1994). These models are then compared to a more complex, physiologically realistic and up to date model of both the SMC and adjacent EC based on a model of the so-called 'NVU' describing the process of functional hyperaemia in the brain tissue (Farr and David, 2011; Dormanns et al., 2015). If the dynamics of this complex SMC/EC model are similar to those of a simpler SMC model then this may provide insight into the behaviour of the complex model, of which analysis is more difficult.

The resulting cell dynamics of a single and coupled cell system may in turn further our understanding of the dynamics behind the formation and propagation of Ca^{2+} waves; the spatial and temporal dynamics of a large population of cells in a two dimensional (2D) spatial domain are investigated *in silico* in order to gain insight into the Ca^{2+} signalling through the arterial wall and throughout the brain cortex. This population of cells is simulated using the Goldbeter et al. (1990) model on a 2D spatial domain. The term *in silico* refers to computer simulations of the dynamics of complex biological systems as opposed to *in vivo* or *in vitro*. These simulations can provide insight into observed experimental data.

The concept of spatial curvature is introduced to these simulations as the cerebral cortex composed of folded grey matter is a strongly curved structure and an artery contains areas of strong curvature, in particular at an arterial bifurcation. This is achieved by simulating the Goldbeter et al. (1990) model on a toroidal surface as a torus contains areas of both negative (on the inside of the torus) and positive Gaussian curvature (on the outside of the torus).

1.1 Thesis Overview

The following chapter contains the literature review. Chapter 3 contains our work on extending the SMC model by (Goldbeter et al., 1990) based on Ca^{2+} induced Ca^{2+} release (CICR) into a two coupled cell model and the resulting dynamics, and a brief comparison with two other SMC models by Gonzalez-Fernandez and Ermentrout (1994) and Meyer and Stryer (1988). Chapter 4 extends the work of Farr and David (2011) and Dormanns et al. (2015) by examining a reduced model of their NVU model containing SMC and EC components then coupling two of the resulting SMC/EC units. This complex model is then compared to the previous simple models examined in Chapter 3. Chapter 5 contains analysis on the generic excitable FitzHugh-Nagumo (FHN) model and Goldbeter SMC model simulated on a flat two dimensional spatial domain. Chapter 6 extends our work in Chapter 5 and the work of Kneer et al. (2014) by simulating the FHN and Goldbeter models on a curved surface, namely a torus. Chapter 7 contains the discussion and our final conclusions.

Chapter 2

Literature Review

2.1 Cell Anatomy

Smooth muscle cells (SMCs) are found in the outer walls of various organs and tubes in the body, in particular arteries and veins. Arteries are composed of layers of SMCs and within them endothelial cells (ECs) adjacent to the lumen where the blood flows, as seen in Figure 2.1.

These SMCs are able to contract or relax generating rhythmic dilations and contractions. This behaviour known as vasomotion occurs both *in vitro* and *in vivo* independently of any rhythmic movements in the body such as the heartbeat or the respiratory cycle (Haddock and Hill, 2005). Vasodilation widens the arteries and so increases blood flow to tissue areas in need, while vasoconstriction narrows the arteries and thus is critical to staunching haemorrhage and blood loss. These two mechanisms combined produce vasomotion and are used by the body to regulate blood flow and in some cases maintain mean arterial pressure.

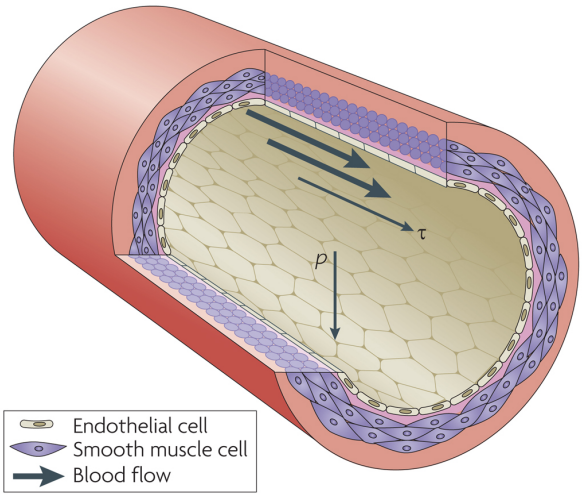

Figure 2.1: A section of artery wall containing SMCs and ECs (Hahn and Schwartz, 2009).

A general eukaryotic cell consists of components including the membrane, the cytosol, the nucleus, and the sarcoplasmic reticulum (SR) or endoplasmic reticulum (ER) which contain large stores of calcium (Ca^{2+}) inside the cell. Ions (and hence electrical current) are able to pass between adjacent cells through channels known as gap junctions. The membrane separates the inside of the cell from the external environment and acts as a capacitor as it can support a potential difference across the membrane (the so called 'membrane potential'). Ions such as Ca^{2+}, potassium (K^+) and sodium (Na^+) travel across the membrane from regions of high to low voltage, and by Fick's Law from regions of high to low concentration. These ions move through passageways from channel proteins where the passageways have selective permeability to allow only certain ions through. In many of these channels, passage is governed by a 'gate' which may open or close in response to chemical or electrical signals. The cytosol is the intracellular fluid that contains a complex mixture of substances such as ions and molecules dissolved in water and makes up the bulk of the cell.

2.2 Calcium Dynamics

In many types of cells Ca^{2+} acts as an important signalling molecule (Wilkins and Sneyd, 1998). In a single cell there are a number of processes governing the Ca^{2+} concentration of the cell cytosol which are able to produce Ca^{2+} oscillations under certain conditions. These oscillations are considered crucial for many cellular processes such as cell reproduction, secretion, and movement (Wilkins and Sneyd, 1998). When the oscillations spread to neighbouring cells this is referred to as a travelling Ca^{2+} wave.

The contraction of SMCs is caused by an increase in cytosolic Ca^{2+} concentration through the process of Ca^{2+} initiated formation of crossbridges between the myosin and actin filaments (Hai and Murphy, 1988). As a result vasomotion is observed when a population of SMCs undergo synchronised Ca^{2+} oscillations.

Cells will either oscillate or remain at a steady state depending on a variety of parameters, some of which are detailed in the following subsections. The main sequence of reactions that takes place to produce Ca^{2+} oscillations is as follows (Wilkins and Sneyd, 1998): The receptor triggered hydrolysis of phosphatidylinositol 4,5-bisphosphate by phospholipase-C (PLC) results in the formation of inotisol trisphosphate (IP_3) which diffuses through the cell cytoplasm and binds to IP_3 receptors located on the SR/ER. IP_3 receptors allow the opening of Ca^{2+} channels which causes a flow of ions in a direction normally dependent on the concentration gradient, leading to an efflux of large amounts of Ca^{2+} from the internal stores. The Ca^{2+} then activates the IP_3 receptors, leading to the release of further Ca^{2+} in an autocatalytic process known as Ca^{2+} induced Ca^{2+} release (CICR). High cytosolic Ca^{2+} concentrations then inactivate the receptor

and Ca^{2+} pumps actively remove Ca^{2+} from the cytosol, pumping it back into the stores or out of the cell until the cell returns to steady state. This process repeats periodically, causing oscillations in the cytosolic Ca^{2+} concentration and other variables such as the membrane potential (voltage) or other ion concentrations.

If a cell is not oscillatory then the Ca^{2+} concentration and other variables will remain at a steady state. If the cell is at a steady state then it may be either excitable or nonexcitable, as the cytosol is an excitable medium with respect to Ca^{2+} release (Wilkins and Sneyd, 1998). If the cell is excitable then for a weak stimulus such as an input of Ca^{2+} to the cytosol, the Ca^{2+} concentration will more or less return directly to the resting state. However for a stronger stimulus above some threshold value the Ca^{2+} concentration will rapidly increase before slowly returning to the resting state, i.e. it emits a spike. If the cell is nonexcitable then no spikes will occur when the cell is stimulated.

In mathematical terminology, an excitable system contains a stable fixed point (FP) (i.e. the resting state), and small perturbations from the FP give rise to trajectories that make small excursions in the phase space or return directly to the FP in a short time period. However, perturbations that exceed some excitation threshold value give rise to trajectories that make a large excursion in phase space before slowly returning to the resting state. In a nonexcitable system any perturbations from the FP will simply return to the FP with no large excursions.

The dynamics of Ca^{2+} in a SMC may be modelled by a set of ordinary differential equations (ODEs) based on conservation of mass, and if the membrane potential of the cell is included, Kirchoff's Law. Minimal SMC Ca^{2+} models may be split into different catagories. For example there are models based on CICR, models based on IP_3 dynamics, and models based on the membrane potential and its effect on the ion fluxes and channels.

2.2.1 CICR based models

Once the Ca^{2+} concentration in the cell cytoplasm rises above some threshold value, the autocatalytic process of CICR takes over and leads to the release of a large amount of Ca^{2+}. Eventually, the high Ca^{2+} concentration shuts off the Ca^{2+} flux and the Ca^{2+} concentration returns to a steady state (Wilkins and Sneyd, 1998). The following model mainly focusses on the process of CICR.

Goldbeter model

The minimal model by Goldbeter et al. (1990) is composed of only two state variables, the cytosolic Ca^{2+} concentration Z and the Ca^{2+} concentration Y in the IP_3 insensitive pool (i.e. the intracellular stores: the SR/ER). When the cell receives an external signal it triggers an increase in IP_3 which is implicitly modelled by an increase in the saturation

function β, leading to a rise in cytosolic Ca^{2+} concentration. A 'bifurcation' occurs when a change in parameter causes a qualitative change in the dynamics of the system. This parameter β may be varied between 0 and 1 in order to achieve different dynamics, e.g. as a bifurcation parameter. The cell variables will either oscillate or tend to a steady state depending on the value of β. The ODEs for this model are as follows.

$$\frac{dZ}{dt} = v_0 + v_1\beta - v_2 + v_3 + k_f Y - kZ \tag{2.1}$$

$$\frac{dY}{dt} = v_2 - v_3 - k_f Y \tag{2.2}$$

with algebraic variables

$$v_2 = V_{M2}\frac{Z^n}{K_2^n + Z^n} \tag{2.3}$$

$$v_3 = V_{M3}\frac{Y^m}{K_R^m + Y^m}\frac{Z^p}{K_A^p + Z^p} \tag{2.4}$$

where v_2 and v_3 are the rate of Ca^{2+} pumping into the internal store and release from the internal store, respectively. v_0 and kZ relate, respectively, to the influx and efflux of Ca^{2+} into and out of the cell. The term $k_f Y$ refers to a nonactivated, leaky transport of Ca^{2+} from the internal stores to the cytosol and the term $v_1\beta$ refers to the flux of Ca^{2+} from the IP_3 sensitive pool.

The parameters are listed in Table 2.1. For further details on the model see Goldbeter et al. (1990). Chapter 3 contains analysis on this model and its extension into a two coupled cell system.

Parameter	Unit	Value	Description
β	–	0 to 1	Saturation function of the IP_3 receptor
v_0	$\mu M s^{-1}$	1	Ca^{2+} influx into the cell
k	s^{-1}	10	Rate of Ca^{2+} efflux out of the cell
k_f	s^{-1}	1	Rate of nonactivated, leaky transport of Ca^{2+} into the internal stores
v_1	$\mu M s^{-1}$	7.3	Rate of Ca^{2+} influx from the IP_3 sensitive pool
V_{M2}	$\mu M s^{-1}$	65	Maximum rate of Ca^{2+} pumping into the internal store
V_{M3}	$\mu M s^{-1}$	500	Maximum rate of Ca^{2+} release from the internal store
K_2	μM	1	Pumping threshold constant
K_R	μM	2	Release threshold constant
K_A	μM	0.9	Activation threshold constant
n	–	2	Pumping cooperativity coefficient
m	–	2	Release cooperativity coefficient
p	–	4	Activation cooperativity coefficient

Table 2.1: Parameter values for the Goldbeter et al. (1990) model

2.2.2 IP_3 based models

In contrast to Section 2.2.1 there have been several models developed to instead focus on the signal molecule IP_3 which plays an important role in the Ca^{2+} dynamics of a cell. IP_3 causes Ca^{2+} channels in the internal stores of cell to open resulting in an influx of Ca^{2+} into the cytosol and hence an increase in cytosolic Ca^{2+} concentration. IP_3 is then removed by hydrolysis or phosphorylation and Ca^{2+} is pumped back into the stores. Ca^{2+} is also taken up by mitochondria and pumped out by transport systems in the cell membrane.

Meyer and Stryer model

The model by Meyer and Stryer (1988) focusses on the dynamics of IP_3 by including the IP_3 concentration as a state variable in contrast to the simpler Goldbeter et al. (1990) model which focussed on the process of CICR. The Meyer and Stryer model contains the following state variables: the cytosolic Ca^{2+} concentration (X), the concentration of IP_3 (Y) and the Ca^{2+} concentration in the internal stores (Z). The ODEs for this model are as follows.

$$\frac{dX}{dt} = J_1 - J_2 - c_6 \left(\frac{X}{c_7}\right)^{3.3} + c_6 \tag{2.5}$$

$$\frac{dY}{dt} = c_4 R \frac{X}{X + K_3} - c_5 Y \tag{2.6}$$

$$\frac{dZ}{dt} = J_2 - J_1 \tag{2.7}$$

with algebraic variables

$$J_1 = c_1 Z \frac{Y^3}{(Y + K_1)^3} \tag{2.8}$$

$$J_2 = c_2 \frac{X^2}{(X + K_2)^2} - c_3 Z^2 \tag{2.9}$$

where J_1 and J_2 are the IP_3 induced efflux of Ca^{2+} from the internal stores and influx of Ca^{2+} into the stores from the cytosol, respectively.

The degree of receptor dependent activation modelled by the parameter R may be varied between 0 and 1 as a bifurcation parameter, determining whether the cell is oscillatory or steady state. For full details of this model see the work of Meyer and Stryer (1988).

2.2.3 Voltage based models

Various other cell models have been constructed that incorporate additional elements and also omit certain elements such as IP_3 and CICR. These models may contain variables such as the membrane potential (voltage) and ions other than Ca^{2+}, or elements such as voltage gated ion channels.

Gonzalez-Fernandez and Ermentrout Model

The model constructed by Gonzalez-Fernandez and Ermentrout (1994) contains no internal stores of Ca^{2+} or any IP_3 dynamics. Instead the focus is on the membrane potential and voltage gated ion channels connecting the cytosol with the outside of the cell through the cell membrane, in particular the voltage gated Ca^{2+} channels and voltage-Ca^{2+} gated K^+ channels. When Ca^{2+} ions enter the cytosol through the voltage-gated channels the cell membrane depolarises, which tends to open the voltage-Ca^{2+}-gated K^+ channels. This results in an outflux of K^+ ions due to the low voltage, and thus the repolarisation of the cell membrane. This in turn closes the Ca^{2+} and K^+ channels and so the membrane returns to its initial state.

The three state variables are the cytosolic Ca^{2+} concentration CAI, the membrane potential V, and the fraction of open voltage-Ca^{2+}-gated K^+ channels N. The ODEs are as follows.

$$\frac{dCAI}{dt} = (-\alpha g_{Ca} m_\infty \cdot (V - v_{Ca}) - k_{Ca} CAI)\,\rho \tag{2.10}$$

$$C\,\frac{dV}{dt} = -g_{Ca} m_\infty \cdot (V - v_{Ca}) - g_K N \cdot (V - v_K) - g_L (V - v_L) \tag{2.11}$$

$$\frac{dN}{dt} = \lambda_n (n_\infty - N) \tag{2.12}$$

with algebraic variables

$$m_\infty = 0.5 \left(1 + \tanh \frac{V - v_1}{v_2}\right) \tag{2.13}$$

$$\rho = \frac{(K_d + CAI)^2}{(K_d + CAI)^2 + K_d B_T} \tag{2.14}$$

$$n_\infty = 0.5 \left(1 + \tanh \frac{V - v_3}{v_4}\right) \tag{2.15}$$

$$\lambda_n = \phi_n \cosh \frac{V - v_3}{2 v_4} \tag{2.16}$$

$$v_3 = -\frac{v_5}{2} \tanh \frac{CAI - Ca_3}{Ca_4} + v_6. \tag{2.17}$$

m_∞ is the equilibrium fraction of open Ca^{2+} channels (where this channel is deemed to be always in equilibrium); ρ is the fraction of cytosolic calcium in its unbuffered form; n_∞ is the equilibrium fraction of open K^+ channels; λ_n is the activation rate constant for the opening K^+ channels; v_3 is the CAI dependent shift on the distribution of K^+ channel open states with respect to membrane potential V.

Gonzalez-Fernandez and Ermentrout introduced a dependence of the parameter v_1 on transmural pressure (the difference in pressure between the inside and outside of the cell). It was suggested that an increase in transmural pressure causes a larger Ca^{2+} transmembrane flux, hence v_1 may be varied as a bifurcation parameter. This parameter determines whether the cells oscillates or tends to a steady state. For full details of this model see the work of Gonzalez-Fernandez and Ermentrout (1994).

2.2.4 More complex models

The preceding minimal models all contain at most 3 state variables and only consider the dynamics in the SMC. However the arterial wall also contains ECs which provide a flux of Ca^{2+} and IP_3 into or out of the SMCs, potentially influencing the SMC dynamics.

One such model of a coupled SMC/EC unit is constructed by Koenigsberger et al. (2005). This 9 dimensional model incorporates IP_3 concentration, membrane potential, the open probability of Ca^{2+}-gated K^+ channels, and Ca^{2+} concentration of both the SMC and EC and their internal stores of Ca^{2+} (the SR and ER, respectively). The important cellular mechanisms governing the Ca^{2+} dynamics in this model are the Ca^{2+} release from IP_3 sensitive stores, the Ca^{2+} uptake in the SR/ER, the Ca^{2+} extrusion from the cytosol (voltage dependent in SMCs), and the leak of Ca^{2+} from the SR/ER. This model effectively combines all important elements from the three minimal SMC models described earlier.

However the model of a so called 'neurovascular unit (NVU)' originally constructed by Farr and David (2011) and later extended by Dormanns et al. (2015) incorporates and updates the SMC/EC model by Koenigsberger et al. (2005). In addition it includes the influence of neuronal activity in the brain on the dynamics of the SMC via the process known as functional hyperaemia, and the effect of the SMC cytosolic Ca^{2+} concentration on the vessel radius, making it a more versatile and physiologically realistic model. The mechanisms behind the important process of functional hyperaemia and the components of the NVU model are detailed in the following section.

2.3 Neurovascular Coupling

The cerebral cortex, a highly complex component of the brain, contains a multitude of blood vessels that provide the brain tissue with oxygen and glucose essential for cellular function. Arteries in the brain are able to regulate their blood supply in response to local changes in a process known as functional hyperaemia. An increase in neuronal activity is followed by a rapid dilation of local blood vessels via the relaxation of the SMCs and hence an increased supply of oxygen and glucose via the blood flow, where the relaxation of the SMCs is caused by a decrease in cytosolic Ca^{2+} concentration. Impaired functional hyperaemia is associated with several pathologies such as Alzheimer's disease, cortical spreading depression (CSD), atherosclerosis, stroke, and hypertension (Girouard and Iadecola, 2006). These begin with a defective relationship between neural activity and the cerebral blood flow (CBF).

Functional hyperaemia is achieved through the process of neurovascular coupling, an intercellular communication system based on ion exchange through pumps and channels and involving neurons, astrocytes (glial cells), SMCs and ECs. Together these cells comprise a NVU (see Figure 2.2).

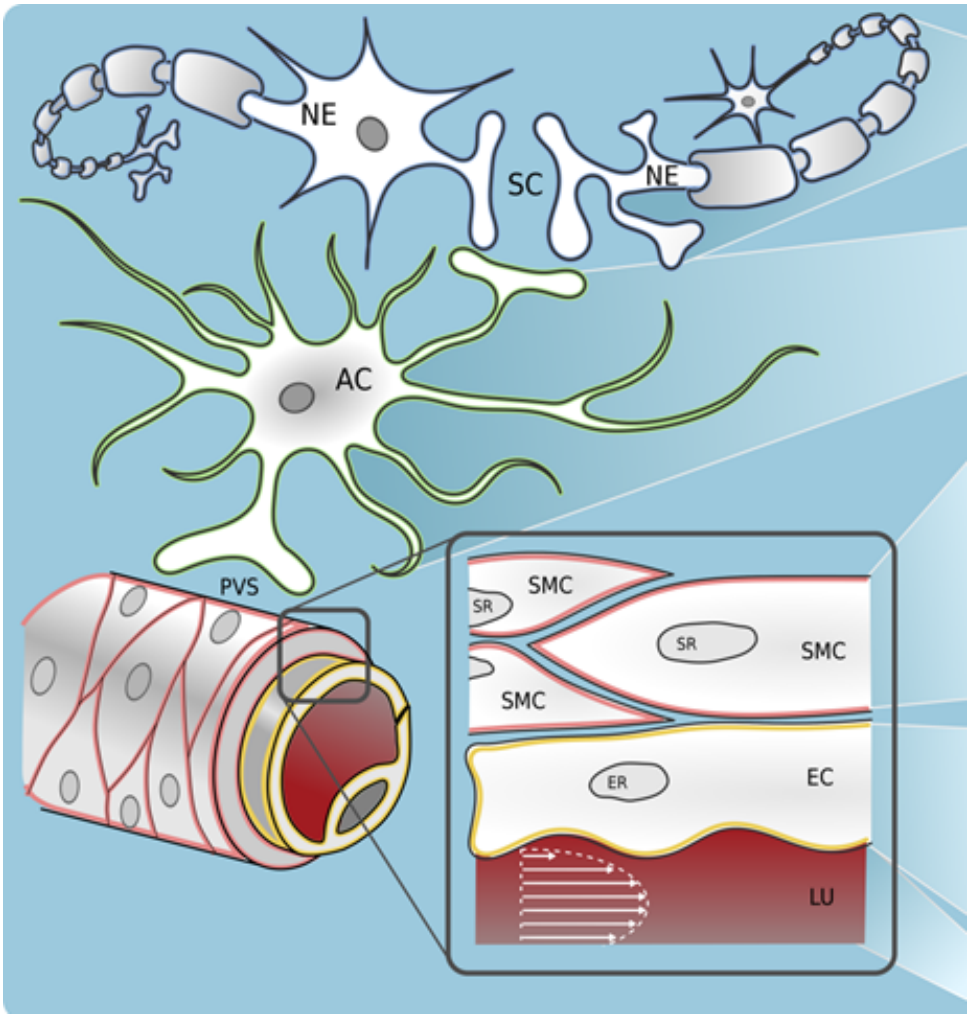

Figure 2.2: An overview of a neurovascular unit (NVU) containing the following cells: neuron (NE), astrocyte (AC), smooth muscle cell (SMC) and endothelial cell (EC), working together to achieve neurovascular coupling: an increase in local blood flow in response to neuronal activity.

The NVU model originally developed at the Bluefern research facility (now UC High Performance Computing) by Farr and David (2011) and later extended by Dormanns et al. (2015) contains a total of 24 state variables and is comprised of the following components: neuron (NE), synaptic cleft (SC), astrocyte (AC), perivascular space (PVS), SMC and EC. The SC is the extracellular space between pre and post synapses on the neuron body; the PVS is the extracellular space between the astrocyte endfoot and the SMC. The SMC component contains the wall mechanics submodule which describes the effect of cytosolic Ca^{2+} concentration on the vessel radius. These components are assembled together using a lumped parameter approach where spatial variations in the compartment are considered negligible, thus allowing intercellular interactions.

The process of neurovascular coupling begins with the release of the neurotransmitter

glutamate at the synapse due to neural activity. This causes K^+ to be released into the synaptic cleft, which is then taken up by the astrocyte via the Na-K pump. Glutamate binds to metabotropic receptors on the astrocyte adjacent to the synaptic cleft; this leads to the release of IP_3 into the cytosol of the astrocyte. The IP_3 stimulates the release of Ca^{2+} from intracellular stores, causing an increase in cytosolic Ca^{2+} concentration. This increase in Ca^{2+} causes AA-derived EETs (signalling molecules) to be produced, and both the Ca^{2+} and EETs gate the big potassium (BK) channels leading from the endfeet of the astrocyte to the PVS. This leads to a release of K^+ into the PVS. This perivascular rise in K^+ gates the inward rectifying potassium (KIR) channels in the SMC causing them to open and leading to a further influx of K^+ into the PVS. This hyperpolarises the SMC membrane, closing the voltage operated Ca^{2+} channels (VOCCs) in the SMC which prevents an influx of Ca^{2+}. The decrease in cytosolic SMC Ca^{2+} mediates the dilation of the blood vessel through the relaxation of the SMC. Therefore the release of glutamate in the synapse leads to the dilation of local blood vessels through a series of mechanisms in the NVU, hence neurovascular coupling (Farr and David, 2011; Dormanns et al., 2015).

The parameter J_{PLC} details the flux of PLC in the EC, effectively controlling the rate of IP_3 production. The extracellular signalling molecule adenosine triphosphate (ATP) has been shown to activate the PLC pathway (Chang et al., 2008) and its concentration is known to vary spatially (Shaikh et al., 2012); hence the parameter J_{PLC} can be varied to simulate different concentration levels of ATP in the lumen adjacent to the EC. Dormanns et al. (2015) showed that the SMC cytosolic Ca^{2+} concentration will oscillate when $J_{PLC} = 0.4$ before and after neuronal stimulation, however when $J_{PLC} = 0.18$ the Ca^{2+} concentration always tends to a steady state.

Neuronal activation is simulated by a release of K^+ and glutamate into the synaptic cleft, together with a corresponding uptake of Na^+ by the neuron. The astrocyte submodel is based on the work of Østby et al. (2009). There are various ion channels and pumps on the astrocyte with ion fluxes in and out of the cell. The SMC/EC submodel is based on the work of Koenigsberger et al. (2005) with various components updated. It is then extended to include a KIR channel into the PVS in order to connect this submodel with the astrocyte submodel. This channel is the only path connecting the SMC/EC submodel with the astrocyte and neuron submodels. In the SMC the wall mechanics submodel is based on the work of Hai and Murphy (1988). It describes the formation of cross bridges between the myosin and actin filaments, and hence the relaxation and contraction of the SMC which will in turn relax or contract the blood vessel wall. It is connected to the SMC/EC submodel by the relationship between SMC cytosolic Ca^{2+} concentration and the active stress of the SMC.

This complex model is altered to focus on the dynamics in the SMC by removing

the neuron and astrocyte compartments and simplifying the neuronal input to a single parameter, then analysed and compared in Chapter 4 with simpler SMC models (detailed in Section 2.2).

2.4 Wave Propagation in Spatial Media

Wave propagation has widespread applications in many fields such as biology and chemistry. One such area of interest is the pathology CSD associated with impaired functional hyperaemia where waves of depolarisation spread throughout the brain cortex. Waves of extracellular K^+ ions are released from depolarized neurons. The high extracellular K^+ concentration depolarises adjacent neurons so that more K^+ is released and the process spreads slowly thoughout the cortex. In particular the phenomenon of Ca^{2+} wave propagation through cells such as SMCs is an area of interest; as stated earlier synchronised oscillations in a population of SMCs will induce vasomotion. Ca^{2+} waves through SMCs may also play a role in other pathologies associated with functional hyperaemia as the SMC is an important component of the NVU, effectively controlling the vessel radius and local blood flow. Hence our interest is in the dynamics behind the formation and propagation of Ca^{2+} waves through a medium such as an arterial wall, or the brain cortex permeated with a network of blood vessels.

2.4.1 Excitable Media

Wave propagation on a surface (i.e. in a two dimensional (2D) spatial system) is possible when the medium is either oscillatory or excitable. An excitable system is characterised by a stable resting state, an excitation threshold and a refractory period. In a spatial medium, when the rate of diffusion (defined as the rate at which a particular substance can spread throughout a particular medium) is high enough, an initial perturbation to the system with conditions above the excitation threshold is able to spread the excitation throughout the medium, triggering the transition from resting to excited state. The different levels of excitability in 2D spatial media are as follows (Kneer et al., 2014):

- Excitable: a wave will propagate and the ends will grow in length
- Sub excitable: a wave will propagate but the ends will shrink in length
- Non excitable: a wave will not propagate at all.

The size of a propagating wave decreases as the system becomes less excitable or as the diffusive strength decreases.

Patterns in spatial excitable media arise from the mutual annihilation of waves when colliding with one another, a property due to the refractory period corresponding to the region immediately behind a travelling wavefront (a.k.a. the 'waveback'). This region is in the recovery phase so it cannot be immediately stimulated by another excitation

wavefront. A spatially-distributed system whose local kinetics is excitable is an excitable medium and the coupling among the locally excitable elements gives rise to a number of distinctive types of wave propagation processes such as Turing patterns and spiral waves (Kapral, 1995).

2.4.2 Spiral Formation

Spiral waves are commonly observed in excitable reaction diffusion systems. They generally emerge in an excitable or oscillatory medium as a result of a wave break (Hill and Morgan, 2014), as spiral rotors (generators of outward rotating spiral waves) can emerge from free ends of a travelling wave front. The rotor sends robust rotating spiral waves outward. The thickness of the wave and tightness of the spiral increases with the excitability of the medium (Sinha and Sridhar, 2014).

Regions of inexcitability can also cause breaks in wave fronts (Weise and Panfilov, 2012), or breaks can be formed as a result of wave interaction. When one wave comes close to a slower travelling wave in front, part of the wave vanishes because of the refractory waveback of the slower wave. This causes a break in the wave and as a result spirals can form.

Some examples of spiral wave formation are the Belousov-Zhabotinskii reaction (Keener, 1986), spiral intercellular waves of Ca^{2+} in slices of hippocampal tissue (Wilkins and Sneyd, 1998), and spiral waves in models of CSD (Gorelova, 1983). Spiral waves will be seen in the results of Chapters 5 and 6.

2.4.3 Fitz-Hugh Nagumo model

The FHN model is a classic generic model for excitable systems with known dynamics (Kneer et al., 2014), first suggested by FitzHugh (1961) and later independently by Nagumo et al. (1962). It is a simplification of the Hodgkin-Huxley model (Hodgkin and Huxley, 1990) and was originally based on a single neuron, mainly used to model spikes and pulses in electrical potential across a neuron. The activator variable u models the fast changes in electrical potential across the axon membrane, while the inhibitor variable v is a slow variable related to the gating mechanism of the membrane channels. In general, the fast variable is called the activator variable, whereas the slow variable is generally called the inhibitor variable.

The model simulated on a two dimensional domain is given by the following partial differential equations (PDEs):

$$\frac{\partial u}{\partial t} = 3u - u^3 - v + D\Delta u \tag{2.18}$$

$$\frac{\partial v}{\partial t} = \varepsilon(u + \beta). \tag{2.19}$$

The parameter $\varepsilon \ll 1$ represents the difference in time scales between the variables u and v. The parameter D controls the rate of diffusion modelled simply by the Laplace operator (i.e. Fick's Law). The parameter β simply determines the stability of the non spatial system; when $\beta < 1$ the system is oscillatory, while for $\beta > 1$ the system is stable. This is due to a supercritical Hopf bifurcation at $\beta = 1$ (Kneer et al., 2014). Note that all variables and parameters of this model are assumed to be nondimensional (including time) as Kneer et al. (2014) do not mention any dimensional units.

When the system is excitable then a wave will propagate outwards from an initial perturbation, when it is subexcitable then a wave will propagate outwards but shrink in length until it disappears, and when it is nonexcitable then no wave will propagate. For approximately $1 < \beta < 1.34$ the system is excitable and for approximately $1.34 < \beta < 1.39$ the system is subexcitable; the larger the parameter β the less excitable the system.

The regions of excitability on a 2D flat surface are given in Figure 2.3 (Kneer et al., 2014). There is some dependence of the level of excitability on the wave size S, where the wave size is defined as the area where the activator u is greater than zero. A critical wave size S^* exists below which the wave is subexcitable and above which the wave is excitable.

Chapter 5 contains our work on the FitzHugh-Nagumo (FHN) and Goldbeter spatial models simulated on a flat surface.

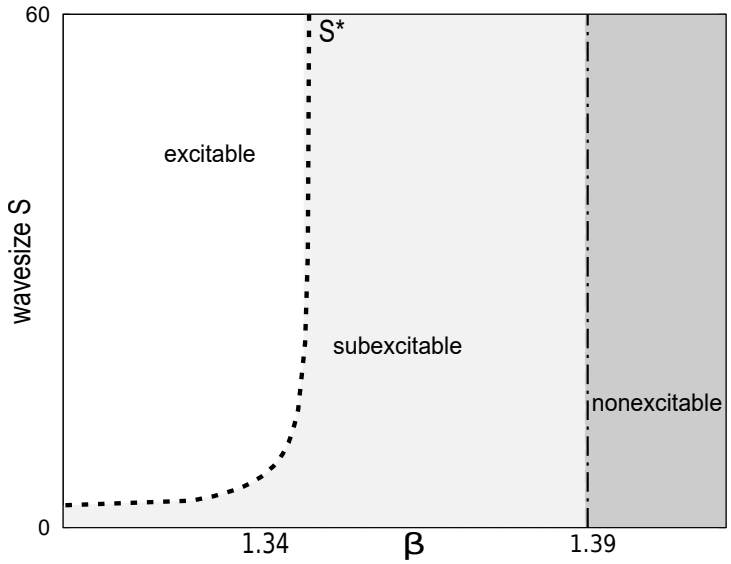

Figure 2.3: The different domains of excitability of the FHN model for $D = 0.12$ on a flat 2D spatial medium. The dotted line represents the critical wave size S^* below which a wave will shrink in length and above which a wave will grow in length. Adapted from Kneer et al. (2014).

2.5 Geometry

Ca^{2+} wave formation and propagation is an important area of interest, however the areas in which these waves propagate are rarely flat surfaces. The Gaussian curvature of a surface is intuitively defined as the amount an object deviates from being flat; for example a convex lens or a sphere has a positively curved surface, while a concave lens has a negatively curved surface. In reality arteries and arterioles are curved structures, in particular the surface is negatively curved at an arterial bifurcation where the artery splits in two. In addition, the cerebral cortex is composed of tightly folded grey matter and as such also contains areas of strongly positive and negative curvature. Various pathologies are associated with impaired functional hyperaemia, in particular the pathology CSD where waves of depolarisation spread throughout the brain cortex. The aspect of curvature in a spatial domain is one not always incorporated into spatial models, however as shown by Kneer et al. (2014) it can have a noticable effect on the dynamics of wave propagation. The work of Kneer et al. (2014) and our work in Chapter 6 use a torus to represent a curved surface as it contains areas of both positive and negative Gaussian curvature.

The surface of a torus in the Euclidean space $\mathbb{R}^3$ can be parameterised by coordinates (θ, φ) as follows:

$$(\theta, \varphi) \mapsto \begin{pmatrix} (R + r\cos\theta)\cos\varphi \\ (R + r\cos\theta)\sin\varphi \\ r\sin\theta \end{pmatrix} = \begin{pmatrix} x \\ y \\ z \end{pmatrix}, \tag{2.20}$$

where $\theta, \varphi \in [0, 2\pi)$ and R and r are the major and minor curvature radii respectively. The torus is visualised in Figure 2.4. The outside of the torus corresponds to $\theta = 0$ and the inside corresponds to $\theta = \pi$. The Gaussian curvature at a point (θ, φ) on a torus surface is a function of θ:

$$\Gamma(\theta) = \frac{\cos\theta}{r(R + r\cos\theta)} \tag{2.21}$$

and may be either positive or negative. The curvature is visualised in Figure 2.5.

2.5.1 Toroidal Coordinates

In addition to the standard coordinates (θ, φ) there exists the so-called toroidal coordinates $(\tilde{\theta}, \tilde{\varphi})$. This is a global isothermal orthgonal coordinate system, that is, coordinates where the metric is locally conformal to the Euclidean metric. Using these coordinates the surface of a torus may be mathematically interpreted as a flat medium with a spatial coupling dependent only on θ. A parameterisation is isothermal if the derived coordinate system is orthogonal and conformal. The following formulation follows that of Kneer et al. (2014).

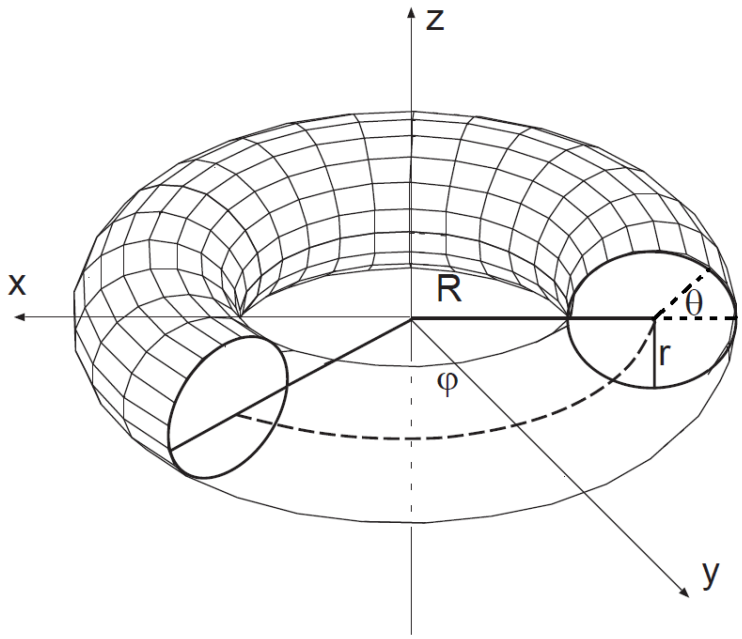

Figure 2.4: Visualisation of a torus in $\mathbb{R}^3$ with coordinates (θ, φ), where R and r are the major and minor curvature radii (Kneer et al., 2014).

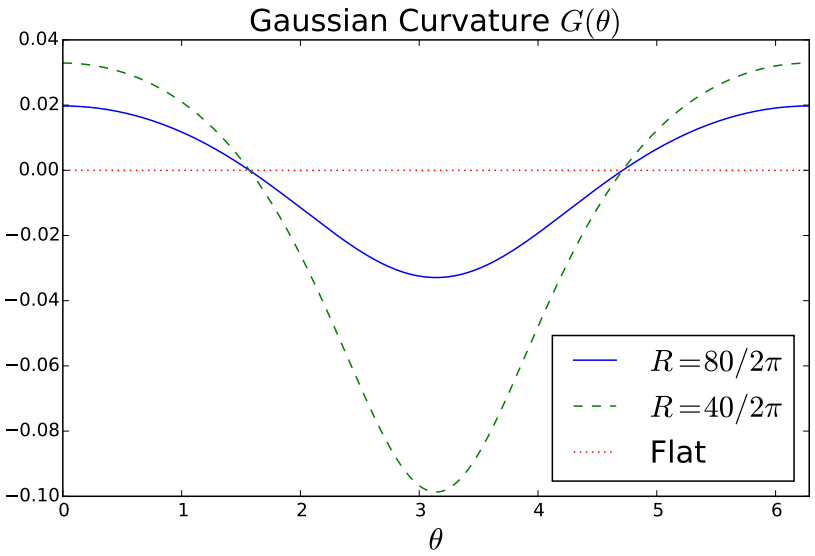

Figure 2.5: Gaussian curvature on a flat surface, and weakly curved ($R = 80/2\pi$) and strongly curved ($R = 40/2\pi$) tori.

The Laplace-Beltrami operator for a parameterisation $f : \alpha^i \mapsto x^j$ is given by

$$\Delta_{LB} = \sum_{i,k} \frac{1}{\sqrt{g}} \frac{\partial}{\partial \alpha^i} \left(g^{ik} \sqrt{g} \frac{\partial}{\partial \alpha^k} \right), \tag{2.22}$$

where J is the Jacobian matrix of f, $G = J^T J$, $g = \det G$, and g^{ik} are the elements of G. The components g^{ik} are

$$g^{ik} = \sum_j \frac{\partial f_j}{\partial \alpha^i} \frac{\partial f_j}{\partial \alpha^k} =: \left\langle \frac{\partial f}{\partial \alpha^i} \middle| \frac{\partial f}{\partial \alpha^k} \right\rangle. \tag{2.23}$$

A parameterisation f of a 2D manifold in 3D space,

$$f : (\alpha^1, \alpha^2) \mapsto \begin{pmatrix} x \\ y \\ z \end{pmatrix} \tag{2.24}$$

is orthgonal if, for $i \neq k$,

$$\left\langle \frac{\partial f}{\partial \alpha^i} \middle| \frac{\partial f}{\partial \alpha^k} \right\rangle = 0, \tag{2.25}$$

and conformal if

$$\left\langle \frac{\partial f}{\partial \alpha^i} \middle| \frac{\partial f}{\partial \alpha^i} \right\rangle = \left\langle \frac{\partial f}{\partial \alpha^k} \middle| \frac{\partial f}{\partial \alpha^k} \right\rangle. \tag{2.26}$$

Hence the Laplace-Beltrami operator for an isothermal parameterisation in two spatial dimensions is

$$\Delta_{LB} = \sum_{i,k} \frac{1}{\sqrt{g}} \frac{\partial}{\partial \alpha^i} \frac{\partial}{\partial \alpha^k} \delta^{ik} \tag{2.27}$$

$$= \sum_i \frac{1}{\sqrt{g}} \frac{\partial^2}{\partial {\alpha^i}^2} = \frac{1}{\sqrt{g}} \Delta, \tag{2.28}$$

where the Kronecker delta δ^{ik} is defined by

$$\delta^{ik} = \begin{cases} 0 & i \neq k \\ 1 & i = k \end{cases} \tag{2.29}$$

and Δ is the Laplace operator for a Euclidean space. The isothermal toroidal coordinates are given by

$$(\tilde{\theta}, \tilde{\varphi}) \mapsto \begin{pmatrix} \dfrac{a \sinh \eta \cos\left(\dfrac{\tilde{\varphi}}{\sinh \eta}\right)}{\cosh \eta - \cos \tilde{\theta}} \\ \dfrac{a \sinh \eta \sin\left(\dfrac{\tilde{\varphi}}{\sinh \eta}\right)}{\cosh \eta - \cos \tilde{\theta}} \\ \dfrac{a \sinh \tilde{\theta}}{\cosh \eta - \cos \tilde{\theta}} \end{pmatrix} = \begin{pmatrix} x \\ y \\ z \end{pmatrix}, \tag{2.30}$$

with

$$a = \sqrt{R^2 - r^2} \tag{2.31}$$

$$\eta = \tanh^{-1}\left(\frac{a}{R}\right). \tag{2.32}$$

The coordinates $(\tilde{\theta}, \tilde{\varphi})$ in terms of (θ, φ) are

$$\tilde{\theta}(\theta) = \cos^{-1}\left(\frac{R}{r} - \frac{a^2}{r(R + r\cos\theta)}\right) \cdot \begin{cases} +1 & \theta \geq 0 \\ -1 & \theta < 0 \end{cases} \tag{2.33}$$

$$\tilde{\varphi}(\varphi) = \varphi \sinh\eta. \tag{2.34}$$

This coordinate systems yields

$$g_{\tilde{\theta},\tilde{\theta}} = g_{\tilde{\varphi},\tilde{\varphi}} = \sqrt{g} = \frac{a^2}{(\cosh\eta - \cos\tilde{\theta})^2}. \tag{2.35}$$

Thus the Laplace-Beltrami operator may be written as

$$\Delta_{LB} = \frac{(\cosh\eta - \cos\tilde{\theta})^2}{a^2}\left(\frac{\partial^2}{\partial\tilde{\theta}^2} + \frac{\partial^2}{\partial\tilde{\varphi}^2}\right). \tag{2.36}$$

We define the coupling strength as

$$C(\theta) = \frac{(\cosh\eta - \cos\tilde{\theta})^2}{a^2} \tag{2.37}$$

given in Figure 2.6. For further details on the derivation of this coordinate system see Kneer et al. (2014).

A reaction diffusion system simulated on a torus will have some diffusion term $D\Delta u$ for some diffusing variable u. This diffusion term may be written in toroidal coordinates, i.e.

$$D\Delta u = DC(\theta)\left(\frac{\partial^2 u}{\partial\tilde{\theta}^2} + \frac{\partial^2 u}{\partial\tilde{\varphi}^2}\right) \tag{2.38}$$

so that $DC(\theta)$ is effectively the spatially varying rate of diffusion on a torus. The Gaussian curvature of a surface has a dramatic effect on the rate of diffusion as shown in the following section.

2.5.2 Effect of Geometry on Fitz-Hugh Nagumo model

The FHN model was simulated on a curved surface with spatially constant parameter β by Kneer et al. (2014) with the following parameter values: $D = 0.12$, $\varepsilon = 0.36$. All variables used (including time) are seemingly dimensionless as no units are ever mentioned in their work. In Chapter 6 we extend their results by simulating both the FHN and Goldbeter models on a curved surface with spatially constant and linearly varied dynamics via the parameter β.

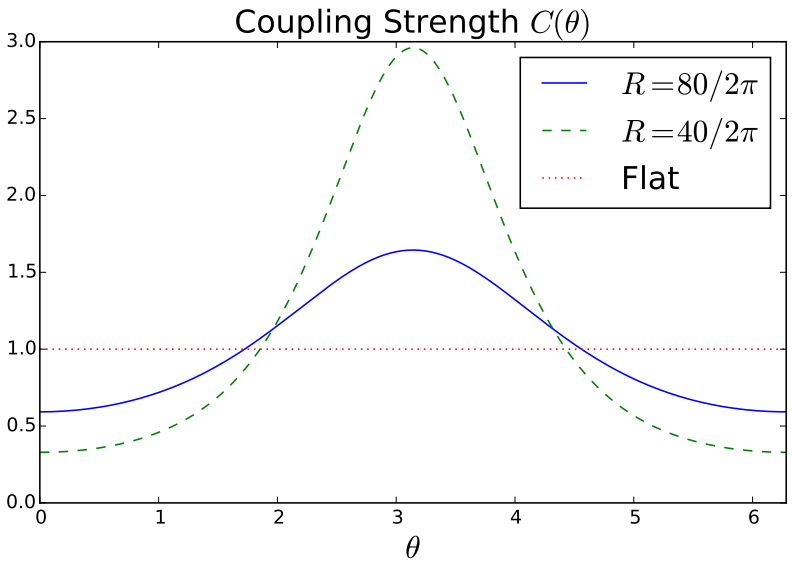

Figure 2.6: Coupling strength $C(\theta)$ defined as (2.37) on a flat surface, weakly curved $(R = 80/2\pi)$ and strongly curved $(R = 40/2\pi)$ torus. The coupling strength is highest on the inside of the torus $(\theta = \pi)$ and lowest on the outside $(\theta = 0)$. The strongly curved torus has a larger gradient in $C(\theta)$.

Kneer et al. (2014) generated propagating waves from an initial perturbation simulated by an increase in the values of the initial conditions (ICs) in a small rectangular area in terms of (θ, φ) on the torus surface. For the majority of the spatial domain the ICs were set to the stable state u_s, v_s and the rectangular area simulating to the initial perturbation was set to $u_s + 2, v_s + 1.5$ corresponding to a supra-threshold excitation.

As with a flat surface, when β in is the nonexcitable domain an initial perturbation will not propagate. When β is subexcitable an initial perturbation will propagate but retract in length, and when β is excitable a perturbation will grow to a ring wave.

A consequence of the curvature dependent rate of diffusion is that an initial perturbation centred on the inside of the torus (where diffusion is highest) will be more inclined to grow in the θ-direction. $DC(\theta)$ will be higher at the centre of the perturbation than at the ends so that the diffusion in the θ-direction is directed outwards, enhancing the growth of the open ends as the wave propagates in the φ-direction. Conversely, an initial perturbation centred on the outside of the torus will be more inclined to retract. This means that the excitable domain for an inside torus wave is slightly larger than on a flat medium, while it is slightly smaller for an outside torus wave; hence the surface curvature effectively extends the regime of propagating excitation waves beyond the threshold of flat surfaces.

An increase in the Gaussian curvature of a torus causes a greater coupling strength (and hence greater diffusion) on the inside and lower diffusion rate on the outside, and a larger gradient in diffusion rate over the toroidal surface (see Figure 2.6). Greater

diffusion causes an increase in wave velocity and hence excitability, therefore an area of strongly negative curvature will have a larger excitable domain and the opposite for an area of strongly positive curvature.

The spatially varying diffusion also leads to additional stable wave solutions for the FHN model on a torus, namely a stable propagating wave segment with temporally constant wave size and shape (Figure 2.7a) and an oscillating wave segment whose wave size oscillates periodically in a self-sustained way (Figure 2.7b). These solutions do not exist on a flat surface because there is no variation in the rate of diffusion over the surface when there is no spatial curvature. The solutions only exist for β in a small subregion of the excitable domain and only on the outside of the torus where the surface is postively curved. A wave centred on the outside of the torus has lower diffusion rate at the centre ($\theta = 0$) than at its ends, causing enhanced retraction of the wave ends as it propagates in the φ-direction. At the same time, when β is in the excitable parameter regime then a perturbation will grow in length. The stable wave segment and stable oscillating wave segment exist due to the balance between β induced growth (excitability) and retraction induced by thespatially varied rate of diffusion; these two are effectively in equilibrium and produce the two wave solutions in Figures 2.7a, 2.7b. These figures have been reproduced with the numerical code used in Chapters 5, 6 to validate our code and resulting simulations. Note that there also exist propagating wave segments on the inside of the torus when β is subexcitable but this solution is unstable and was found via mathematical analysis by Kneer et al. (2014).

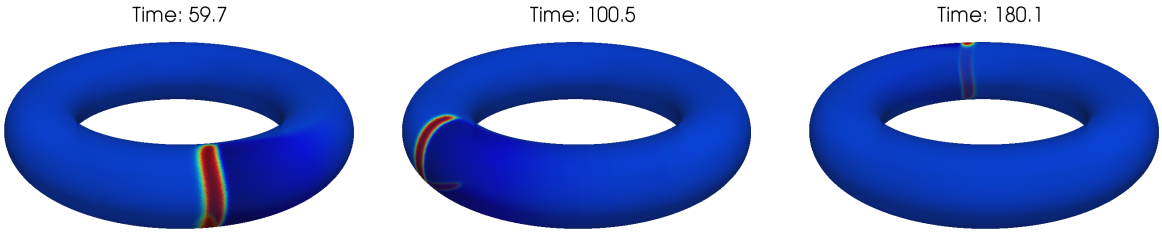

(a) Stable wave segment of constant wave size and shape, $\beta = 1.322$.

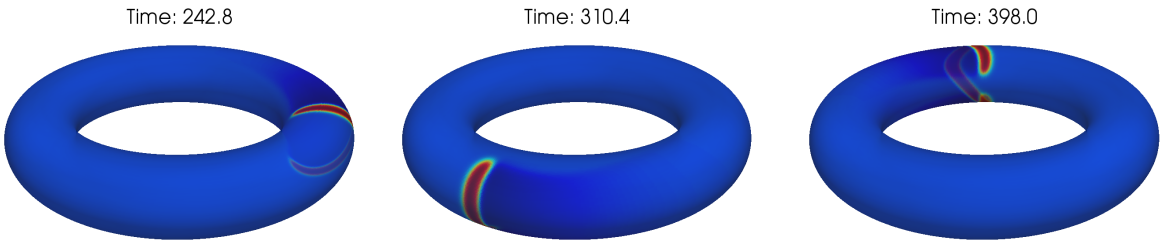

(b) Wave segment oscillating in size, $\beta = 1.32$.

Figure 2.7: Propagating wave segments of activator concentration $u(t, \theta, \varphi)$ moving clockwise on a torus with major radius $R = 80/2\pi$ and minor radius $r = 20/2\pi$. Generated using the FHN model with $D = 0.12$ using the code implemented in Chapters 5 and 6.

Chapter 3

Goldbeter Model

In this chapter we analyse the model constructed by Goldbeter et al. (1990) detailing the dynamics of calcium (Ca^{2+}) in a cell and which specifically focusses on the intracellular process of Ca^{2+} induced Ca^{2+} release (CICR). This model is explained in detail in Section 2.2.1 and contains the state variables Z, the cytosolic Ca^{2+} concentration, and Y, the Ca^{2+} concentration in the internal stores of the cell. The system is first nondimensionalised in order to remove any dependence on units and as there are only two variables we can analyse the nullclines of the system. We then vary the parameter β to perform a bifurcation analysis and the single cell model is then extended to include two cells coupled together with some nondimensional coupling strength D. We vary the parameter β for each cell and analyse how the dynamics change with the coupling strength D by considering the changing trajectories in the phase space and the power spectra of each cell.

3.1 Method

The single cell and coupled cell systems are solved in Matlab using ODE45. The time series graphs, nullcline diagrams, trajectory plots, and power spectra are all produced in Matlab. The bifurcation analysis is achieved using the continuation package AUTO (Champneys et al., 2002).

3.1.1 Coupled Cell Model

For the coupled cell model we consider two adjacent cells coupled by the gap junctions connecting the cytosol of the two cells. There are two cells hence two sets of the single cell model, using Z_1, Y_1 for cell 1 and Z_2, Y_2 for cell 2. We let β_1 be the saturation function for cell 1 and similarly β_2 for cell 2.

A linear diffusion term modelling the flux of Ca^{2+} from cell to cell is added to the ordinary differential equations (ODEs) for Z_1 and Z_2 which mimics Fick's law where ions

move from high to low concentrations. This coupling term is $d(Z_2 - Z_1)$ for cell 1 and similarly $d(Z_1 - Z_2)$ for cell 2. This parameter d is the rate of diffusion of Ca^{2+} from one cell to the other (a.k.a. the coupling strength) with units of s^{-1}.

For a row of cells the flux of Ca^{2+} comes from its two adjacent cells; hence the total flux for a cell i in a row of cells is

$$d(Z_{i+1} - 2Z_i + Z_{i-1}).$$

If we let $d = P/h^2$ where $h = 50\ \mu m$ is the length of a smooth muscle cell (SMC) and letting x be the spatial variable we can regard the above as

$$P\frac{Z_i(x+h,t) - 2Z_i(x,t) + Z_i(x-h,t)}{h^2},$$

which is a discrete approximation to

$$P\frac{\partial^2 Z}{\partial x^2}$$

as $h \to 0$. Here P plays the role of the effective Ca^{2+} diffusivity. Values for this diffusion coefficient P are known for various substances and are typically measured in $cm^2 s^{-1}$. However, at the present time no precise value for the effective diffusion coefficient for Ca^{2+} has been found so a range of values for $d = P/h^2$ is considered. If $d = 0$, then there is effectively no coupling and the cells are independent of one another.

There is no change to the equations for Ca^{2+} in the stores ($Y_1,\ Y_2$) as the gap junctions connect only the cytosol of each cell.

3.1.2 Non-dimensionalisation

In order to remove the dependence on units and hence gain a better understanding of the magnitude of the parameters we non-dimensionalise the equations of the system. The following parameters and variables are defined:

$$\tau = k_f t,\ \overline{v_1} = \frac{v_1}{v_0},\ \overline{VM_2} = \frac{VM_2}{v_0},\ \overline{VM_3} = \frac{VM_3}{v_0}, \overline{k} = \frac{k}{k_f},\ Z = \frac{k_f}{v_0}z,\ Y = \frac{k_f}{v_0}y.$$

Then the non-dimensional single cell system becomes

$$\frac{dZ}{dt} = 1 + \overline{v_1}\beta - v_2 + v_3 + Y - \overline{k}Z, \tag{3.1}$$

$$\frac{dY}{dt} = v_2 - v_3 - Y, \tag{3.2}$$

with

$$\overline{v_2} = \overline{VM_2}\frac{(\frac{v_0}{k_f}Z)^n}{K_2^n + (\frac{v_0}{k_f}Z)^n}, \tag{3.3}$$

$$\overline{v_3} = \overline{VM_3}\frac{(\frac{v_0}{k_f}Y)^m}{K_R^m + (\frac{v_0}{k_f}Y)^m}\frac{(\frac{v_0}{k_f}Z)^p}{K_A^p + (\frac{v_0}{k_f}Z)^p}. \tag{3.4}$$

To nondimensionalise the coupled cell system we define $D = \frac{d}{k_f}$ where k_f is the time constant of the nonactivated leaky transport of Ca^{2+} from the store into the cytosol. The nondimensional coupled system is given by:

$$\frac{dZ_1}{dt} = 1 + \overline{v_1}\beta_1 - \overline{v_2} + \overline{v_3} + Y_1 - \overline{k}Z_1 + D(Z_2 - Z_1), \tag{3.5}$$

$$\frac{dZ_2}{dt} = 1 + \overline{v_1}\beta_2 - \overline{v_2} + \overline{v_3} + Y_2 - \overline{k}Z_2 + D(Z_1 - Z_2), \tag{3.6}$$

$$\frac{dY_1}{dt} = \overline{v_2} - \overline{v_3} - Y_1, \tag{3.7}$$

$$\frac{dY_2}{dt} = \overline{v_2} - \overline{v_3} - Y_2, \tag{3.8}$$

with equations 3.3, 3.4 for each cell. From here on we drop the overline for all variables for ease of use.

3.2 Single Cell Results

This section details our results for the single cell model constructed by Goldbeter et al. (1990). We can reproduce their results where the system variables oscillate for mid range of β and tend to a steady state for low and high β, see Figure 3.1.

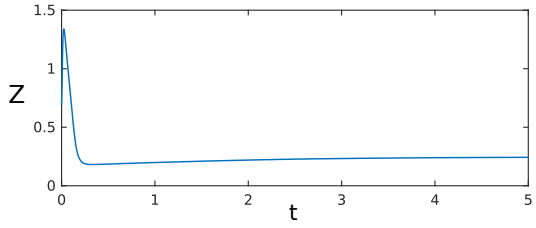

(a) $\beta = 0.2$: Stable (excitable).

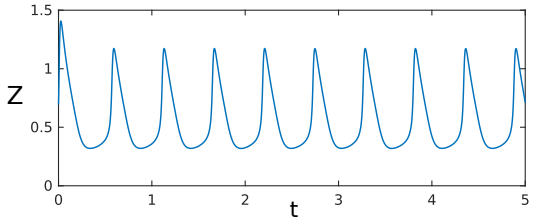

(b) $\beta = 0.6$: Oscillatory.

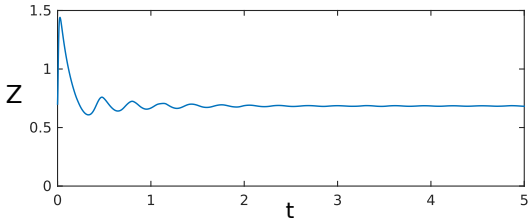

(c) $\beta = 0.8$: Stable (nonexcitable).

Figure 3.1: Time series plots of the cytosolic Ca^{2+} concentration Z of the Goldbeter model for different values of β.

Plotting the nullclines and the variable Z against Y in the phase plane with time as a parametric variable can provide further insight into the structure of the system dynamics. The nullclines of a system are where the derivatives are equal to zero. In the Goldbeter model these are the Z-nullcline $\frac{dZ}{dt} = 0$ and Y-nullcline $\frac{dY}{dt} = 0$. The fixed points are

where the nullclines intersect. In a 2 dimensional system the nullclines can be represented by curves on a 2D plot, as in Figure 3.2 for different values of β. As the parameter β only appears in the Z equation the Y nullcline (red) will remain constant while the Z nullcline (blue) will change with β.

The system will be either oscillatory or stable, but within the stable domain we can be more precise – a nonspatial stable system is either nonexcitable or excitable. Recall that an excitable system contains a stable fixed point (FP) and an excitation threshold above which trajectories make a large excursion in phase space. When β is between approximately 0.13 and 0.29 then the system is excitable (Figures 3.1a, 3.2b). When the initial conditions (ICs) are located to the right of both nullclines then the so called excitation threshold is exceeded and the trajectory experiences a large excursion, followed by a slow path along the Z nullcline before arriving at the stable fixed point. This gives the distinctive shape of the time series plot containing the initial spike in Z followed by a slow refractory period as it tends to the stable FP. The system is not considered excitable for β less than 0.13, for example $\beta = 0.1$ (Figure 3.2a), despite the similar nullcline structure and trajectories to the case where $\beta = 0.2$. This is because the FP of the system is relatively lower and the Z nullcline higher when $\beta = 0.1$ (in comparison to $\beta = 0.2$); consequently the threshold is too high to be considered excitable.

When the system is oscillatory (Figures 3.1b, 3.2c) then any trajectories tend to the stable limit cycle (LC). When β is large (Figures 3.1c, 3.2d) then all trajectories tend to a spiral attracting fixed point. The system is nonexcitable here because there is no threshold above which the system will undergo a relatively large excursion in the phase space.

The qualitative changes in behaviour between stable and oscillatory indicate bifurcations in the system, therefore the parameter β is varied as a bifurcation parameter. To investigate these bifurcations the continuation package AUTO is implemented to create a bifurcation diagram with β ranging from 0 to 1 plotted against the cytosolic Ca^{2+} concentration Z in Figure 3.3.

For low values of β the systems settles to a steady state with a low cytosolic Ca^{2+} concentration. This is represented by the line of stable FPs (black solid line). At $\beta = 0.28895$ there is a supercritical Hopf bifurcation (red square) at which point the stable FP becomes unstable (black dashed line) and generates a stable LC. The two red lines originating at this Hopf bifurcation represent the maximum and minimum amplitude of the stable LCs. The LCs immediately after this bifurcation are small amplitude followed by an extremely steep increase in amplitude shown in Figure 3.4; the cause of this sharp incline has not yet been determined. At $\beta = 0.77427$ there is another supercritical Hopf bifurcation where the stable LC and unstable FP effectively collide, leaving a stable FP. From this point on the system again tends to a steady state.

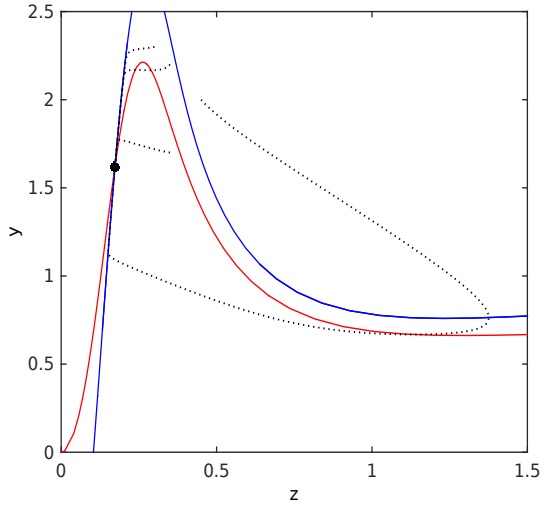

(a) $\beta = 0.1$: Stable.

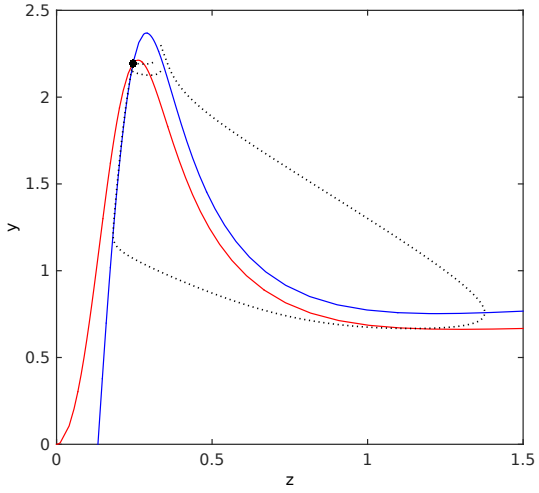

(b) $\beta = 0.2$: Stable (excitable).

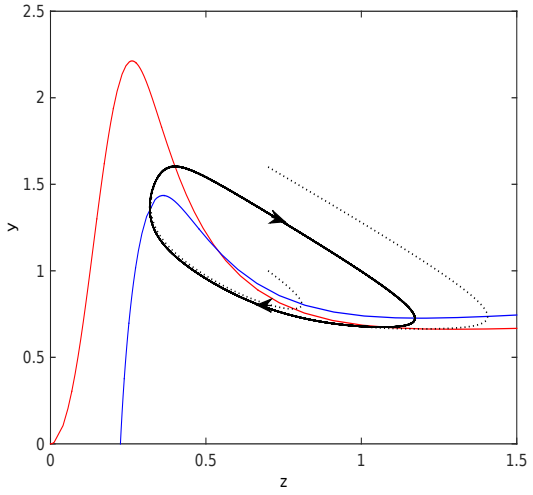

(c) $\beta = 0.6$: Oscillatory.

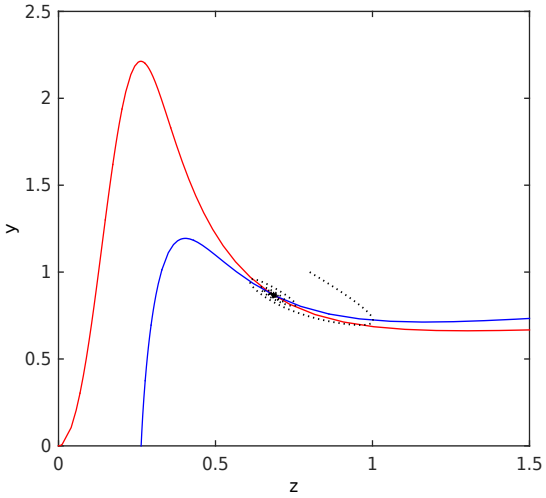

(d) $\beta = 0.8$: Stable (spiral attractor).

Figure 3.2: The (Z, Y) phase space of the single cell system using the Goldbeter et al. (1990) model. The nullclines (blue: $\frac{dZ}{dt} = 0$, red: $\frac{dY}{dt} = 0$), sample trajectories (black dotted) and limit cycles (LCs) (black solid are shown for various values of β. The dynamics qualitatively change when β is varied.)

The period of oscillations is shown in Figure 3.5. The steep increase in period corresponds to the small amplitude LCs; again the cause of this steep increase is unknown. The period then smoothly decreases as β increases.

Goldbeter et al. (1990) found the oscillatory region to be $\beta \in [0.291, 0.775]$ where the period is greatest at $\beta = 0.291$ and decreases as β increases. Our more accurate numerical analysis gives the oscillatory region $\beta \in [0.28895, 0.77427]$, with a small amplitude region $[0.28895, 0.28948]$ where the period increases with β, and the large amplitude region $[0.28948, 0.77427]$ where the period decreases with β.

The excitability of the model is also shown in Figure 3.3. When β is either very low or very high the system is nonexcitable, when β is in the oscillatory domain the system oscillates, and when β is in the excitable/subexcitable domains then the system experiences a large excursion in phase space when perturbed from the FP, i.e. a small increase in Ca^{2+} results in a large spike of Ca^{2+} concentration. The small subexcitable domain is essentially the same as the excitable domain for nonspatial and one dimensional spatial systems; however in the two dimensional (2D) spatial systems discussed in Chapters 5, 6 a wave will propagate in an excitable medium but will shrink in length in a subexcitable medium. Hence for the remainder of this chapter the subexcitable subdomain will no longer be referenced but is included in the excitable domain.

3.3 Coupled Cell Results

In this section we couple two cells via their gap junctions where cell 1 has the parameter β_1 and cell 2 has β_2. Physiologically, adjacent cells must be similar so we only consider cells with either identical β or similar values of β. There are 3 different domains of behaviour dependent on β (seen in Figure 3.3), namely nonexcitable, excitable, and oscillatory. We consider identical cells with the same β, cells in the same domain, and cells in neighbouring domains.

The maximum value of the coupling coefficient D used in the following analysis is relatively large. When modelling nonidentical cells, quite different β values and a large range of D are used to effectively exaggerate the dynamics occuring between the state with no coupling ($D = 0$) and eventual synchronisation. In reality, we would find cells with much closer parameter values and hence need much lower D to synchronise. This means our range of D is not physiologically chosen, it is simply large enough to clearly observe the different dynamical states that occur.

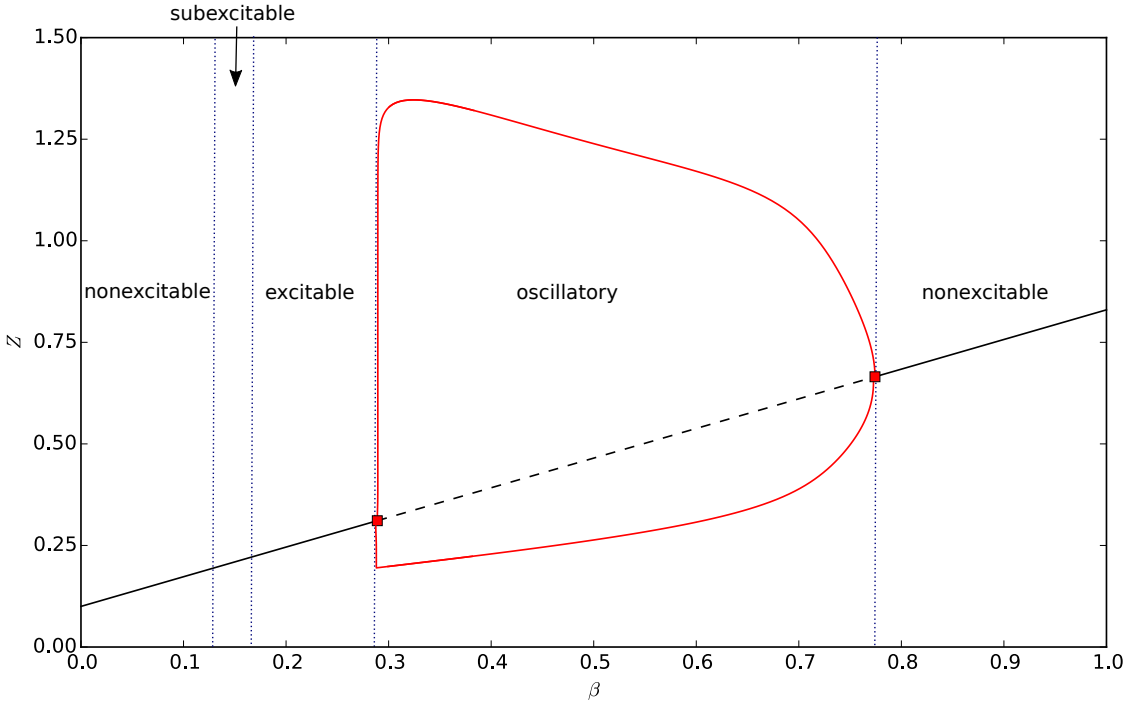

Figure 3.3: Bifurcation diagram of the Goldbeter et al. (1990) model with β varied against the cytosolic Ca^{2+} concentration Z, also containing the excitability domains.
Red square: supercritical hopf bifurcation, black solid: stable FP, black dashed: unstable FP, Red solid: stable LC.

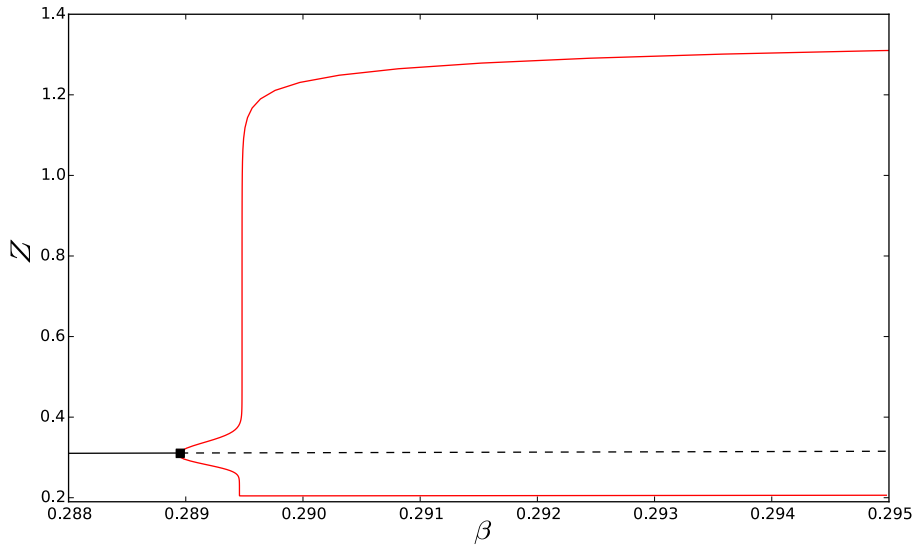

Figure 3.4: Closer view of Figure 3.3 around the left Hopf bifurcation at $\beta = 0.28895$. There is a rapid increase in the amplitude of oscillations after the bifurcation.

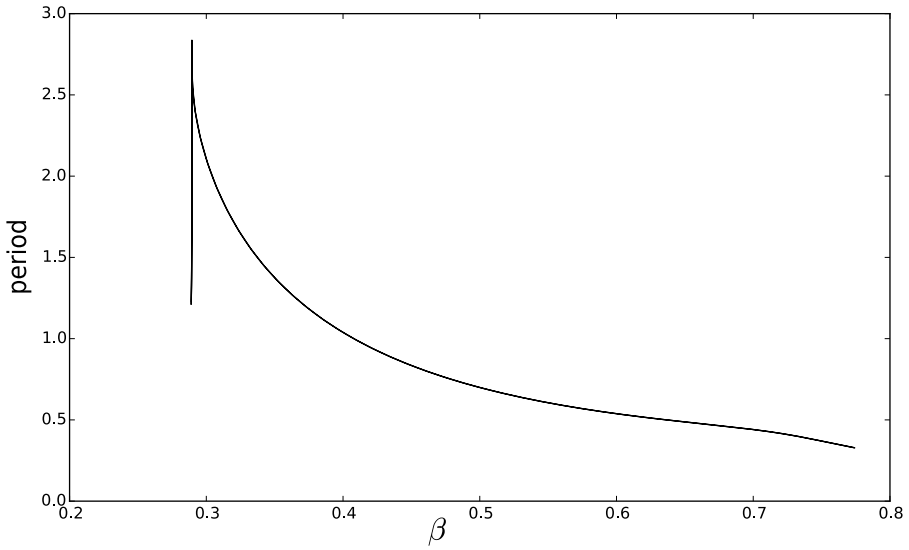

Figure 3.5: Period of the LCs found in the bifurcation diagram of the Goldbeter et al. (1990) model in Figure 3.3. There is a rapid increase in period corresponding to the small amplitude LCs shown in Figure 3.4.

3.3.1 Coupled Cells in the Same Domain

Two identical cells produce no interesting behaviour; the basic behaviour of both cells is the same as when uncoupled. In reality adjacent cells may have intrinsic differences in their behaviour or experience different environmental conditions, thus it is of much greater physiological importance to understand the dynamics of nonidentical coupled cells.

Two nonexcitable cells or two excitable cells with similar β will have the same basic behaviour as when they are uncoupled, with the respective stable FPs of the cells moving closer together in the phase space as the coupling strength D increases. However two oscillatory cells will display more complex behaviour when coupled together. As each cell has two corresponding state variables we can plot the trajectory of each cell in its respective (Z, Y) phase space with time as a parametric variable (plotting the trajectory after some time so that we may ignore any initial transient behaviour) for multiple values of D.

When plotting the set of trajectories the ICs are taken from the previous case so that it simulates increasing the coupling strength gradually from 0 (or alternatively smoothly decreasing the coupling strength to 0). This results in trajectories continuing down a set of FPs or LCs instead of jumping to a different attracting state if another such state exists. Because of this there may be additional stable FPs or LCs present in the phase space for values of D greater than 0; however as our trajectories continue down a set of stable solutions we do not encounter these other stable states if they do exist.

Consider two oscillatory cells with $\beta_1 = 0.4$, $\beta_2 = 0.5$. When uncoupled cell 1 will oscillate with greater amplitude and period than cell 2 (see Figures 3.3, 3.5). The trajectories for each cell are shown in Figure 3.6. When uncoupled ($D = 0$) the cells oscillate independently, represented by a simple LC trajectory. When coupled together ($D > 0$) the flux of Ca^{2+} from cell to cell will interfere with the oscillations causing the cells to both oscillate with variable amplitude, represented by additional 'loops' in the trajectory. This produces amplitude modulated oscillations as seen in Figure 3.7, where the amplitude of oscillations is effectively a function of time instead of constant. As the coupling strength D increases the intercellular flux of Ca^{2+} becomes larger and as a result more 'loops' are added to the cell trajectories. Finally when the coupling strength is strong enough the cells synchronise and act as one, oscillating with the same frequency and similar amplitude corresponding to a simple LC in the phase space.

These oscillations can be viewed as a 'signal' composed of one or more frequencies, either in the time domain (as in Figure 3.7) or in the frequency domain. By using a Fourier transform we can decompose a signal into a series of sinusoidal functions with different frequencies and the distribution of these frequencies is called the power spectrum. For example a simple sine wave will decompose into a single frequency with the power of the frequency corresponding to the amplitude of the wave. Using a Fourier transform of the cytosolic Ca^{2+} concentration Z of each cell we are able to examine their power spectra and thus analyse the distribution of power among the frequencies that make up these oscillatory 'signals'. This provides an additional technique to analyse the change in behaviour as the cells are coupled. Figure 3.8 shows the power spectra of each oscillatory cell at different coupling strengths.

When the cells are uncoupled ($D = 0$) their respective power spectra are completely independent (Figure 3.8a). By increasing the coupling to $D = 1$ we find that the distribution of power among the frequencies of the cells are irregular, indicating that the cells are exhibiting complex behaviour (Figure 3.8b). With strong coupling ($D = 2.5$) the power spectra of the two cells are almost identical with differences only in power (Figure 3.8c). This indicates the cells have become synchronised. The only difference when the cells are synchronised is the amplitude of the frequency spikes, so to clearly see the level of synchronisation we examine the difference in power between the cells.

As both the trajectories and frequency distributions of the cells qualitatively change as the coupling increases, we expect some form of 'frequency bifurcation' to occur where the cells begin to synchronise. To see this we plot the difference between the power spectra of the two cells (cell 1 minus cell 2) for varying coupling strength D in Figure 3.9. The colour represents the difference in power between the cells, with red representing the frequencies at which cell 1 has greater amplitude and black representing the frequencies at which cell 2 has greater amplitude.

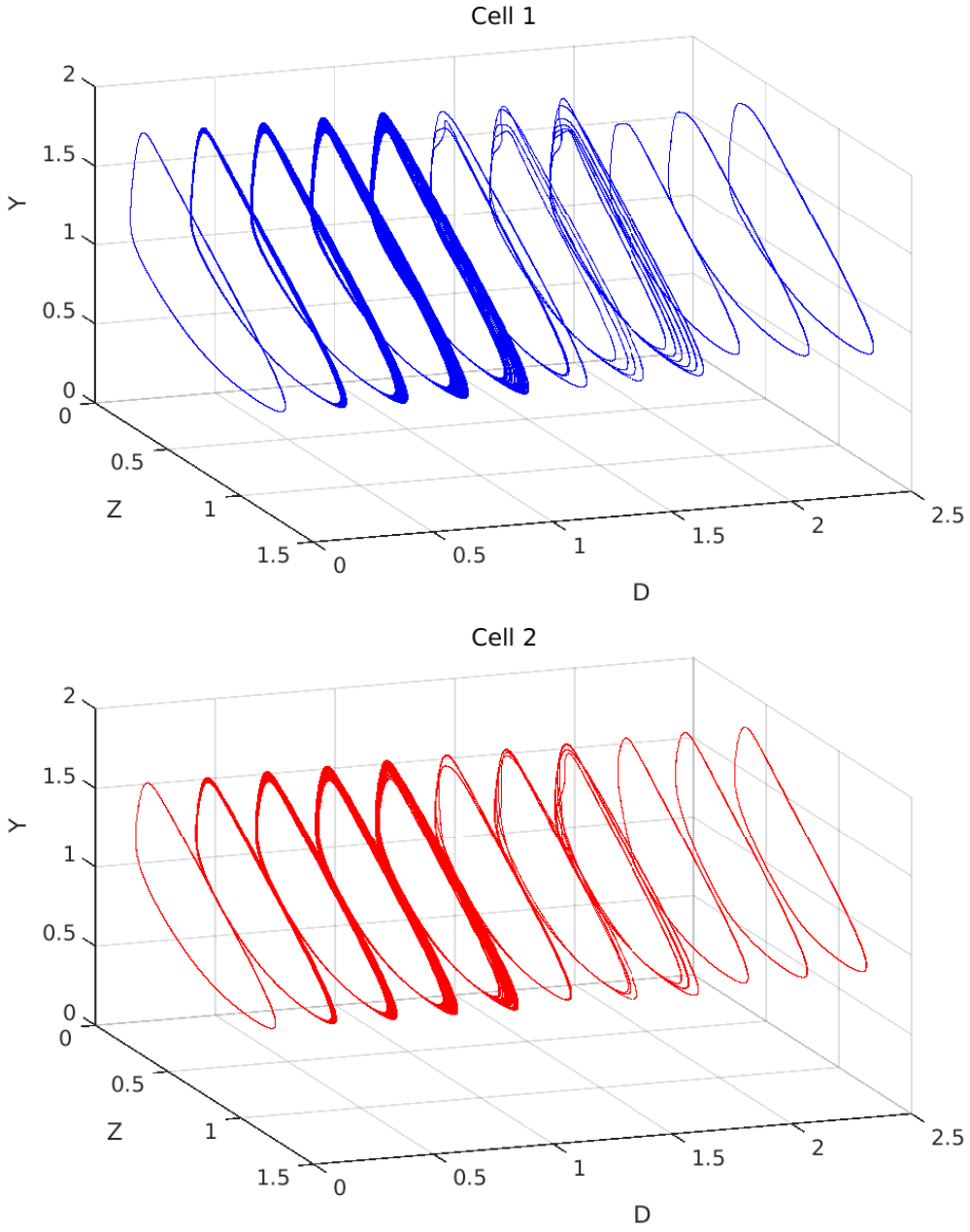

Figure 3.6: Trajectories in the respective (Z, Y) space of two coupled oscillatory cells with $\beta_1 = 0.4$, $\beta_2 = 0.5$.

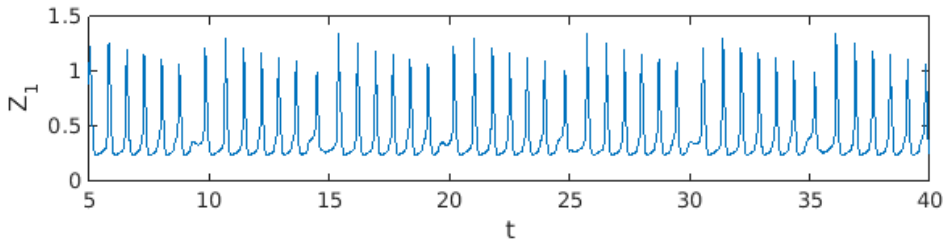

Figure 3.7: Variable amplitude oscillations in cytosolic Ca^{2+} concentration Z of cell 1 with $\beta_1 = 0.4$, $\beta_2 = 0.5$, $D = 1.8$.

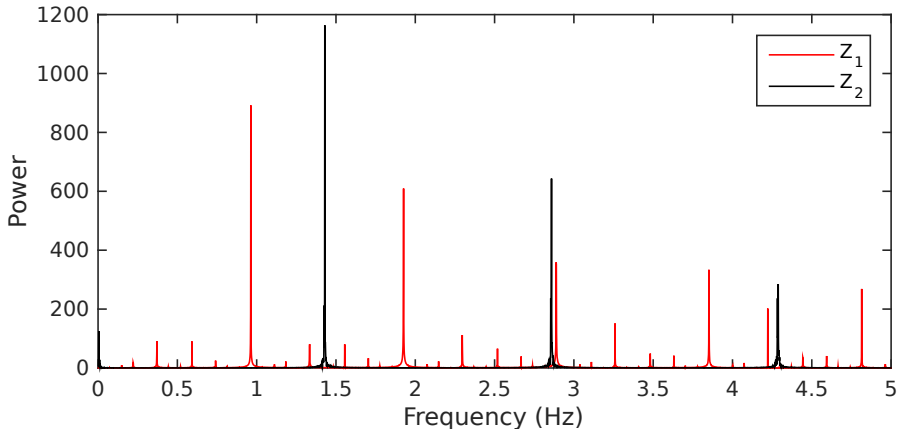

(a) $D = 0$.

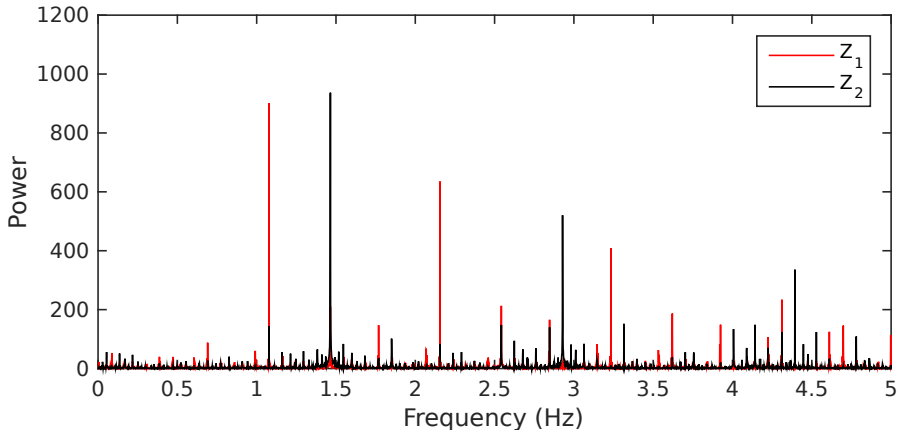

(b) $D = 1$.

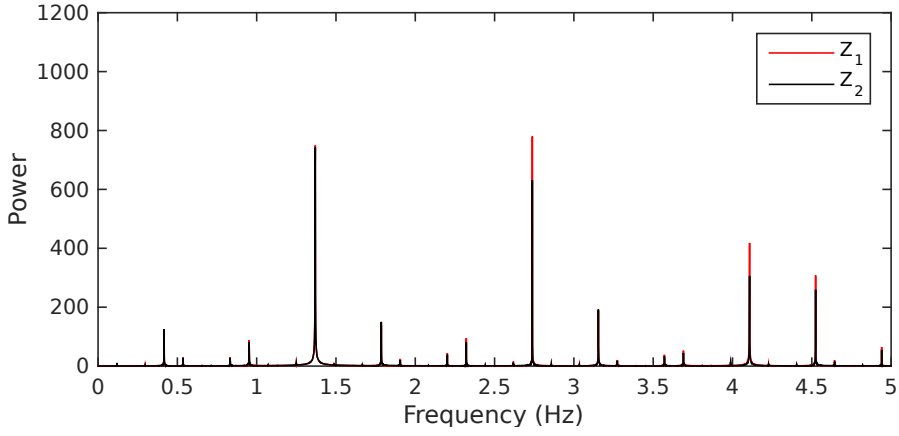

(c) $D = 2.5$.

Figure 3.8: Power spectrum diagrams of two oscillatory cells with $\beta_1 = 0.4$ (red), $\beta_2 = 0.5$ (black) for different coupling strength D. The cells are independent when uncoupled, oscillate with variable amplitude when weakly coupled and synchronised when strongly coupled.

At $D = 0$ there are pairs of points in black and red indicating the independent frequencies of the two uncoupled cells. As the coupling increases additional frequencies are introduced, corresponding to additional loops in the trajectories in Figure 3.6 or equivalently additional 'spikes' in the amplitude modulated oscillations in Figure 3.7. These lines of frequency coalesce in groups around approximately $D = 2$ into single frequencies indicating the cells are synchronised, with a difference only in the amplitude of their respective frequencies. Therefore the cells display variable amplitude oscillations for weak coupling, becoming more complex with additional amplitudes as D approaches approximately 2. After this point the cells are synchronised and the difference between them decreases as the coupling increases.

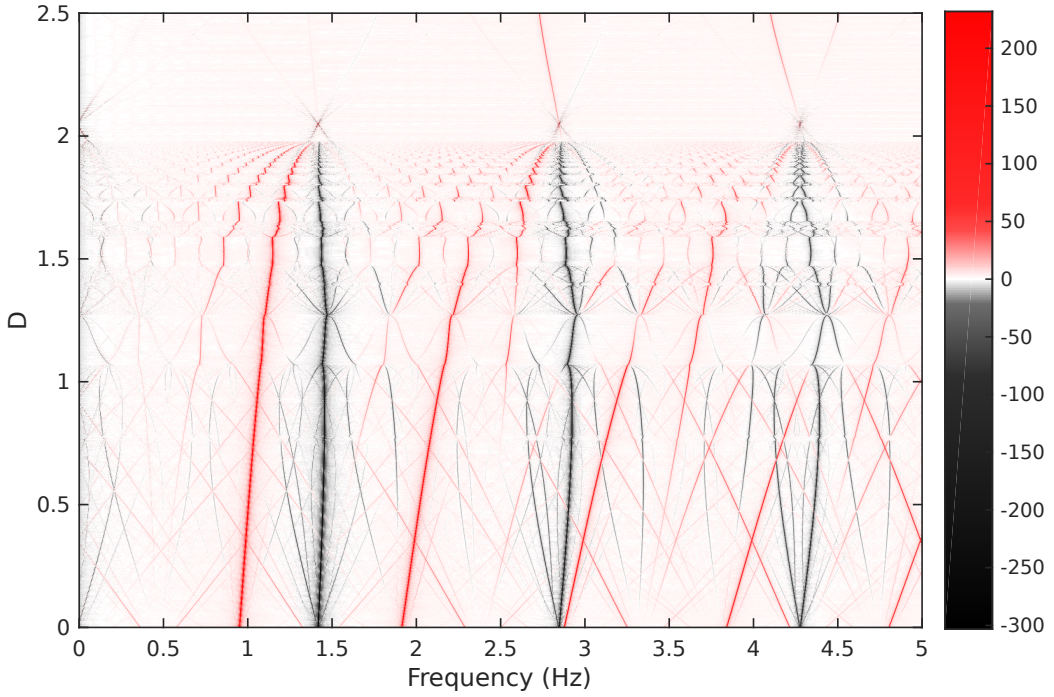

Figure 3.9: The difference in power spectra between two oscillatory cells, $\beta_1 = 0.4$ and $\beta_2 = 0.5$. The cells synchronise when the lines of frequency coalesce at around $D = 2$.

3.3.2 Coupled Cells in Different Domains

In this section we examine the behaviour of two coupled cells from neighbouring domains (excitable, nonexcitable and oscillatory) shown in Figure 3.3.

Excitable and Nonexcitable

Two coupled cells where one is excitable and one is nonexcitable will produce no interesting behaviour as both cells are stable.

Oscillatory and Nonexcitable

Weakly coupling a nonexcitable cell with an oscillatory cell induces a small flux of Ca^{2+} into the nonexcitable cell causing it to immediately oscillate with small amplitude and the same frequency as the oscillatory cell for $D > 0$ in Figure 3.10. As the coupling strength increases the amplitude of oscillations of the nonexcitable cell increases as it becomes more similar in behaviour to the oscillatory cell. Note that the average β of the two cells lies in the oscillatory domain of Figure 3.3 and hence when strongly coupled the cells will both oscillate. If the average β was instead in the nonexcitable domain then the cells would tend to a stable state when strongly coupled.

As the cells always oscillate with the same frequency the power spectra of each cell are identical in frequency distribution and differ only in power.

Oscillatory and Excitable

When coupling an excitable and oscillatory cell the induced behaviour is significantly more interesting. Consider two cells on either side of the left Hopf bifurcation at $\beta = 0.28895$, i.e. one cell in the excitable region and one in the oscillatory region. In this case we take $\beta_1 = 0.25$, $\beta_2 = 0.35$ so that cell 1 is excitable and cell 2 is oscillatory. The trajectories in the phase space of each cell are shown in Figure 3.11.

When weakly coupled the small flux of Ca^{2+} from the oscillatory to the excitable cell will cause the excitable cell to oscillate with small amplitude and the oscillatory cell will remain oscillatory will large amplitude. However once the coupling strength D passes some threshold value the Ca^{2+} flux to the excitable cell will cause its Ca^{2+} concentration to exceed the excitation threshold and the trajectory of the excitable cell will make a large excursion in the phase space in the form of a large amplitude oscillation. This is followed by a small amplitude oscillation as the cell cannot be immediately stimulated into another large excursion by the Ca^{2+} influx because it is in the refractory period after the excitation (see Figure 3.11a at $D = 0.6$). Meanwhile the oscillatory cell oscillates in a double LC, i.e. the trajectory contains two loops in the phase space before periodically repeating.

As the coupling strength increases the small amplitude oscillation of the excitable cell disappears and then the LC effectively loops in on itself creating another small amplitude oscillation, while the oscillatory cell continues to oscillate in a double LC. When strongly coupled (see Figure 3.11a at $D = 2.2$) both cells oscillate with variable amplitude similar to the amplitude modulated oscillations produced by coupled oscillatory cells in Section 3.3.1. After some threshold D these variable amplitude oscillations cease and the cells both oscillate with the same frequency and constant amplitude, indicating synchronisation.

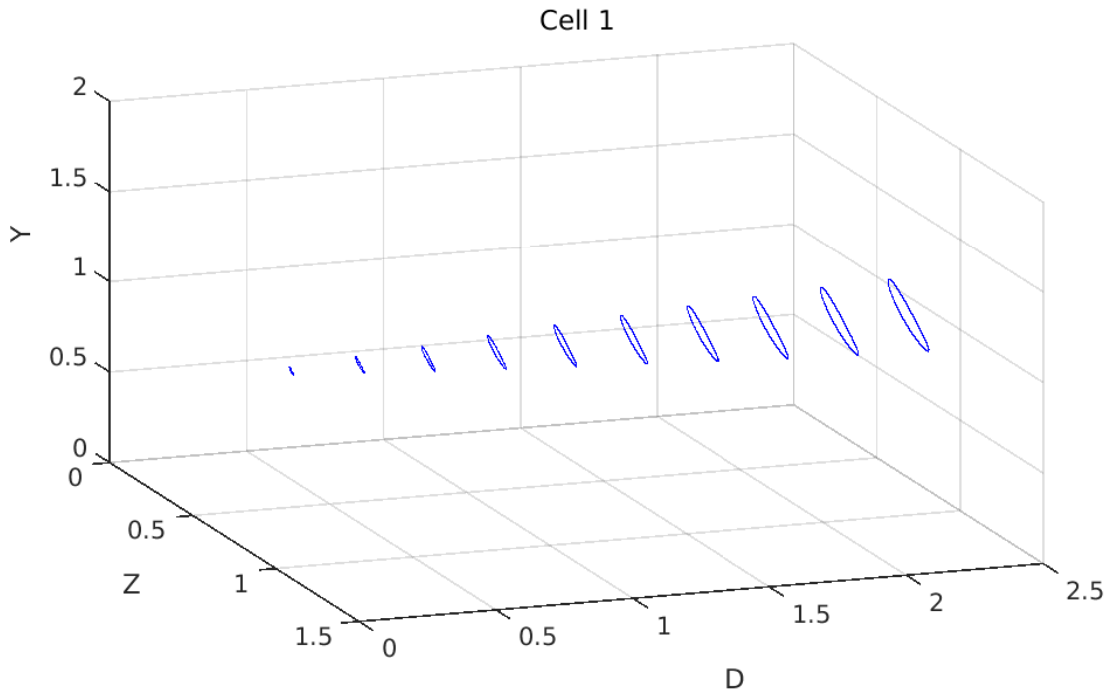

(a) Nonexcitable cell 1 with $\beta_1 = 0.8$

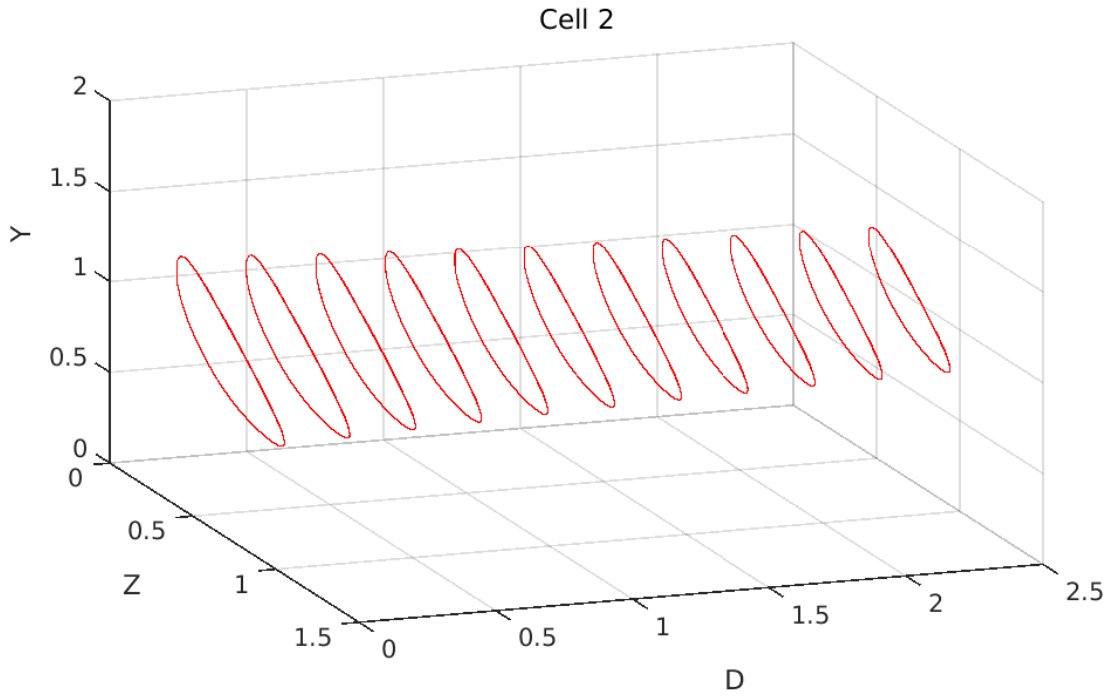

(b) Oscillatory cell 2 with $\beta_2 = 0.7$

Figure 3.10: Trajectories in the (Z, Y) space of each cell. The nonexcitable cell 1 oscillates with the same frequency as cell 1 when coupled due to the Ca^{2+} flux from the oscillatory cell 2. The amplitude of these oscillations increases as the coupling D increases.

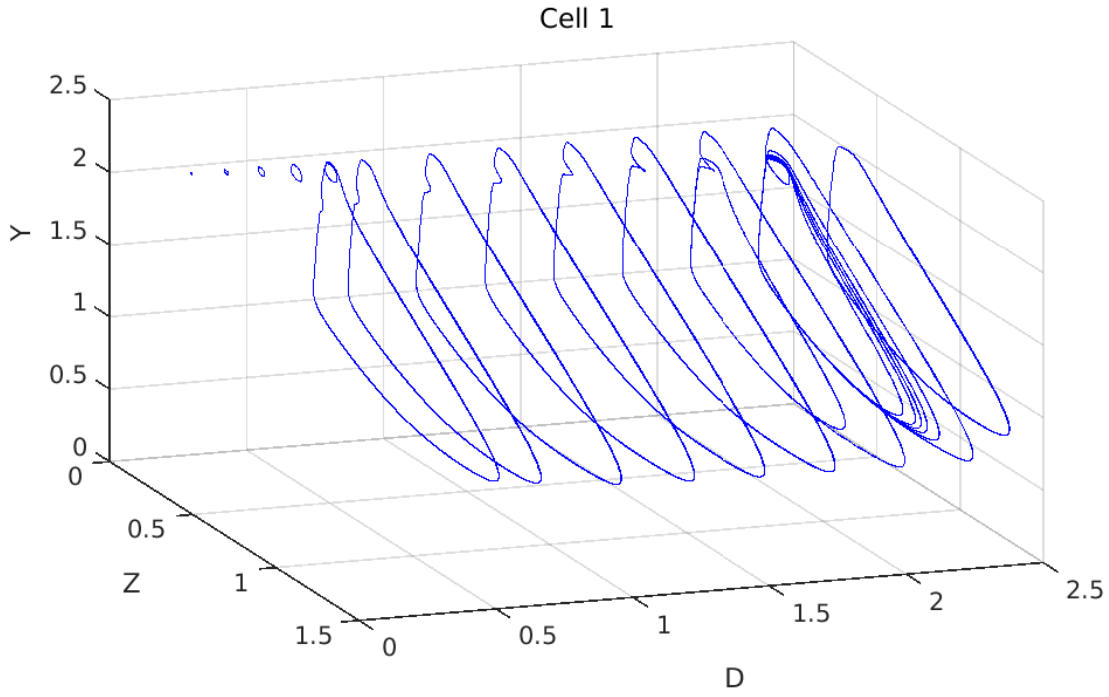

(a) Excitable cell 1 with $\beta_1 = 0.25$

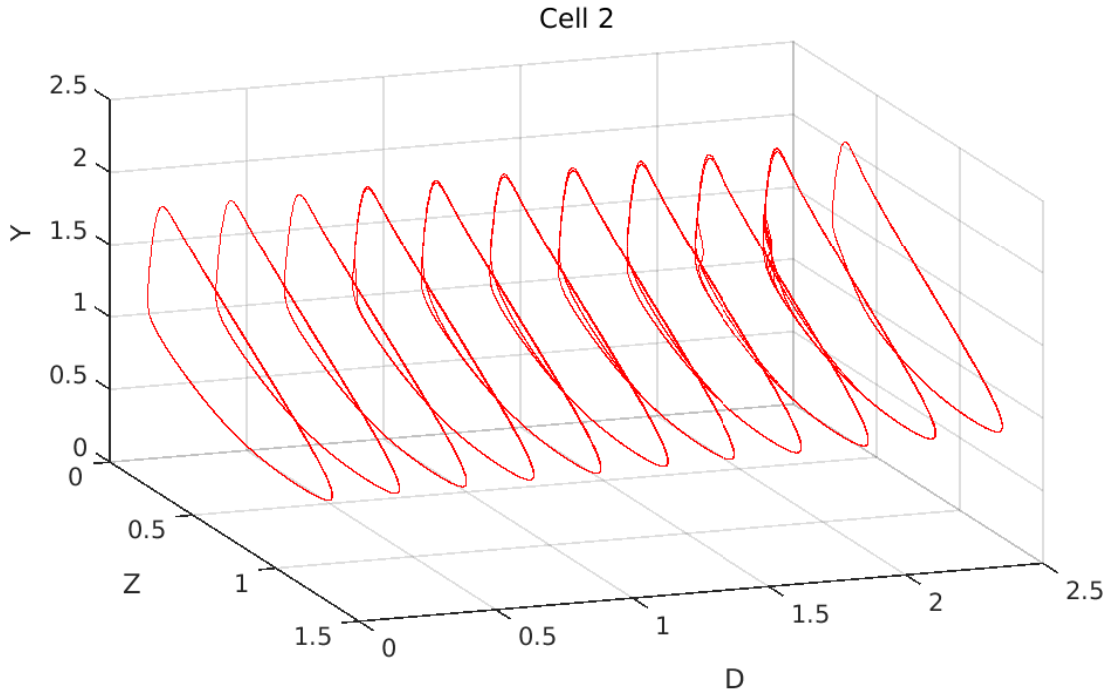

(b) Oscillatory cell 2 with $\beta_2 = 0.35$

Figure 3.11: Trajectories in the (Z, Y) space of each cell. When the coupling strength D reaches some threshold the flux of Ca^{2+} from the oscillatory cell to the excitable cell is enough to exceed the excitation threshold, causing the excitable cell to oscillate with large amplitude. Both cells then oscillate with variable amplitude before synchronising with a common frequency.

To analyse the changing difference between the two cells as the coupling strength is varied we can plot the difference in power spectra of the cytosolic Ca^{2+} concentration Z_1, Z_2 of the two cells (specifically cell 1 − cell 2), shown in Figure 3.12. Note that a non-oscillatory function (e.g. a steady state cell) has a null power spectrum.

For weak coupling up to $D = 0.55$ the frequency distributions of both cells are the same but those of the oscillatory cell 2 have greater power indicated by the black lines, meaning both cells are oscillating with the same frequency and cell 2 with larger amplitude oscillations. In $D \in [0.55, 0.72]$ lies a complex subregion where the excitable cell is transitioning from a small amplitude LC to an alternating small-large amplitude double LC and then to a large amplitude LC, see Figure 3.13. For $D \in [0.72, 2]$ there is little change in the power spectra of each cell. At $D = 2$ additional frequencies are introduced; each discrete jump of frequency in Figure 3.12 adds a loop to the trajectory in Figure 3.14. These frequency spikes coalesce at $D = 2.27$ leaving a simple LC where the cells are synchronised and oscillate with the same frequency. The addition of further frequencies and coalescence into single frequencies is similar to the behaviour of coupled oscillatory cells in Figure 3.9.

3.4 Other Models

Two other models originally constructed by Gonzalez-Fernandez and Ermentrout (1994) and Meyer and Stryer (1988) were given the same analysis by varying the bifurcation parameters v_1 and R respectively (details in Section 2.2). These models also contain an oscillatory domain for mid range values and stable domains for high and low values of their respective parameters. However the bifurcations surrounding this oscillatory domain are different for each model; the Goldbeter model contains two supercritical Hopf bifurcations (see Figure 3.3) where one Hopf bifurcation has an extremely steep increase in both the period and amplitude of oscillations generated by this bifurcation.

The bifurcation diagram produced using the model by Gonzalez-Fernandez and Ermentrout (1994) in Figure 3.15a contains an oscillatory domain enclosed by a Hopf bifurcation on one side and what appears to be a saddle node infinite cycle bifurcation on the other. The latter bifurcation occurs when a LC collides with a saddle point forming a homoclinic orbit with infinite period.

The bifurcation diagram produced using the model by Meyer and Stryer (1988) in Figure 3.15b contains an oscillatory domain enclosed by a Hopf bifurcation on one side and a limit point cycle (LPC) bifurcation on the other side. At this LPC bifurcation the stable LCs generated by the Hopf bifurcation change direction (in terms of the bifurcation parameter R) and become unstable. These unstable LCs then disappear at a subcritical Hopf bifurcation. Hence there is an additional bistable domain where a stable LC, unstable LC and stable FP all exist.

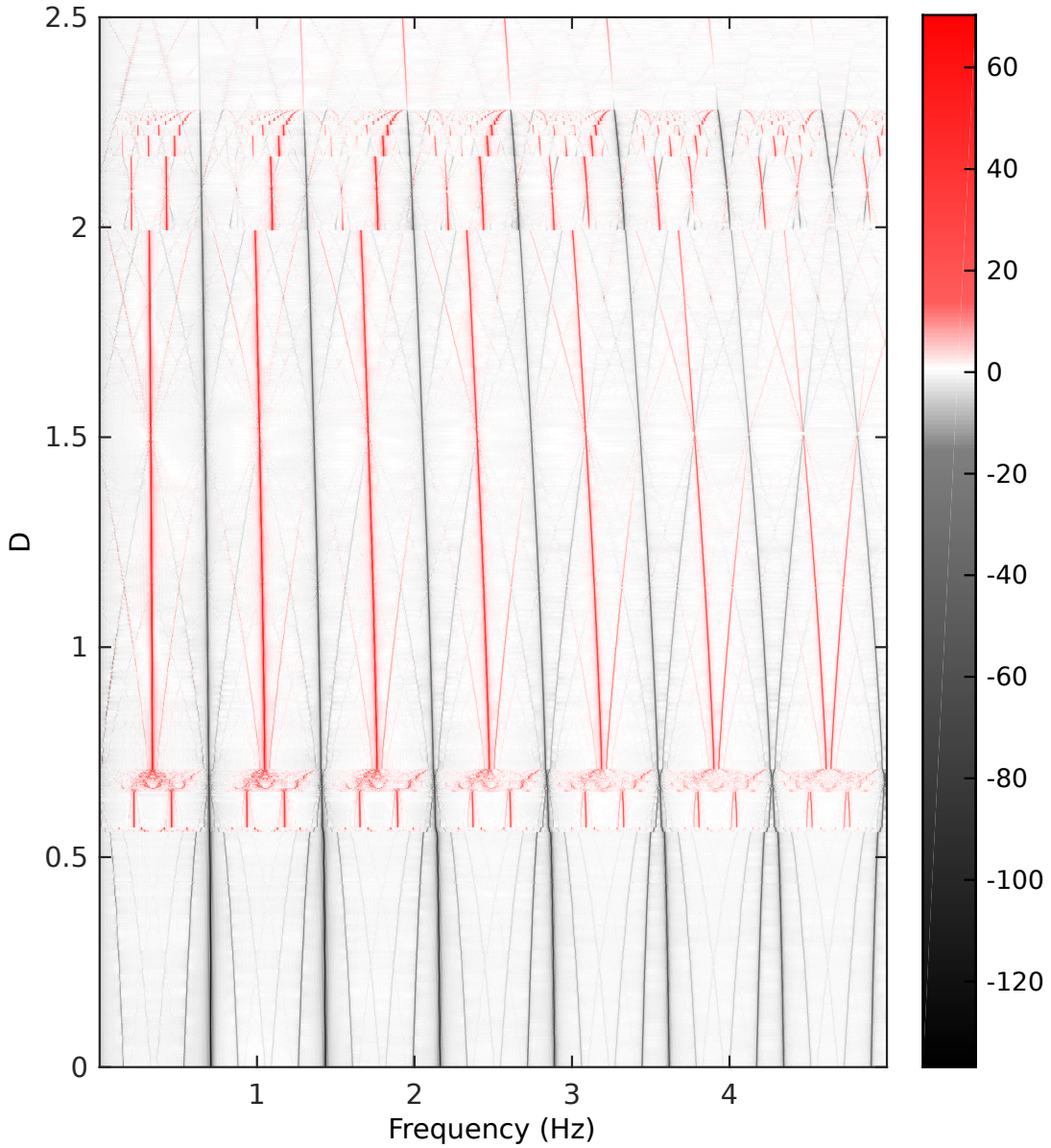

Figure 3.12: The difference in power spectra between an excitable cell 1 and oscillatory cell 2, $\beta_1 = 0.25$ and $\beta_2 = 0.35$. The two transition regions are clearly shown by the complex frequency distributions.

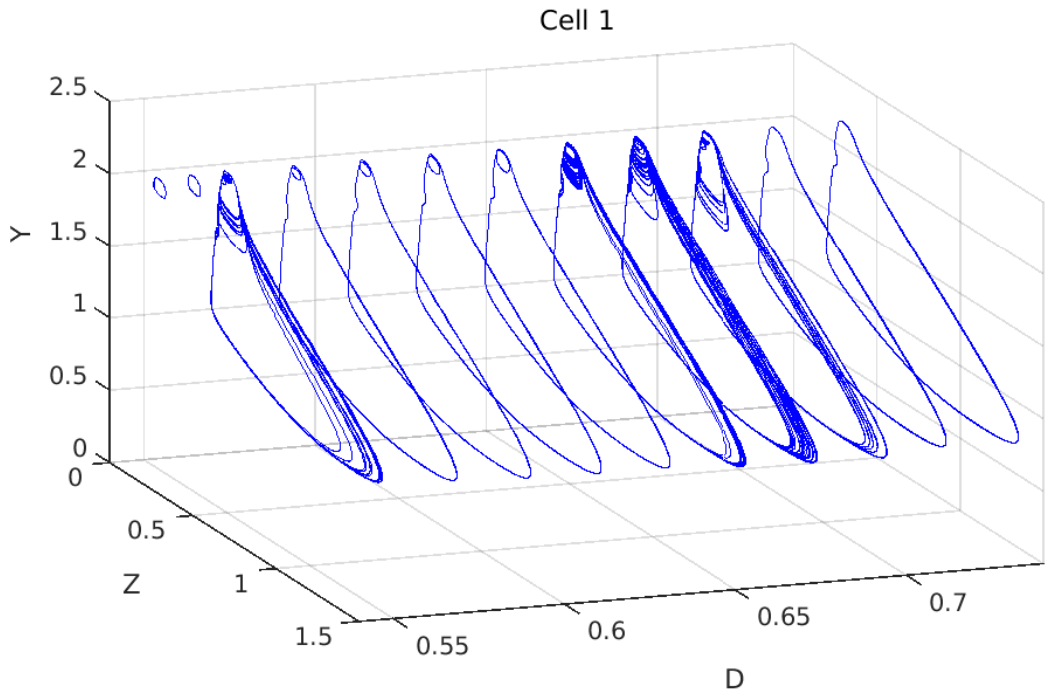

Figure 3.13: Trajectory in the (Z, Y) space of excitable cell 1 with $\beta_1 = 0.25$ and $\beta_2 = 0.35$, for $D \in [0.54, 0.74]$. The behaviour of the cell transitions from small to large amplitude oscillations.

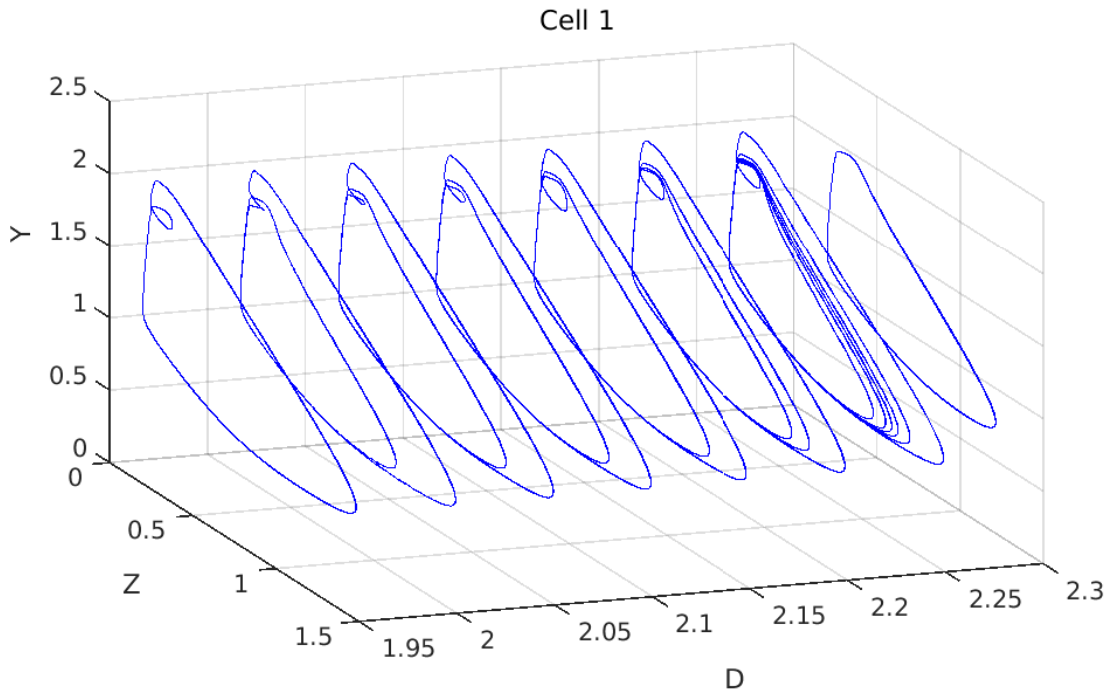

Figure 3.14: Trajectory in the (Z, Y) space of excitable cell 1 with $\beta_1 = 0.25$ and $\beta_2 = 0.35$, for $D \in [1.95, 2.3]$. The behaviour of the cell transitions from variable amplitude to constant amplitude oscillations.

The models by Gonzalez-Fernandez and Ermentrout (1994) and Meyer and Stryer (1988) contain excitable subdomains in the stable domains adjacent to the saddle node infinite cycle and LPC bifurcation respectively, however the exact size and range of these domains have not been calculated.

Extending these models to two coupled cells produces similar behaviour to the results in Section 3.3, i.e. two coupled oscillatory cells will produce amplitude modulated oscillations, and an excitable cell coupled with an oscillatory cell will transition from small amplitude to variable amplitude and then large amplitude oscillations as the coupling strength increases as in Figure 3.11. Hence the behaviour observed by two coupled cells is a feature occuring in all Ca^{2+} dynamics cell models analysed so far.

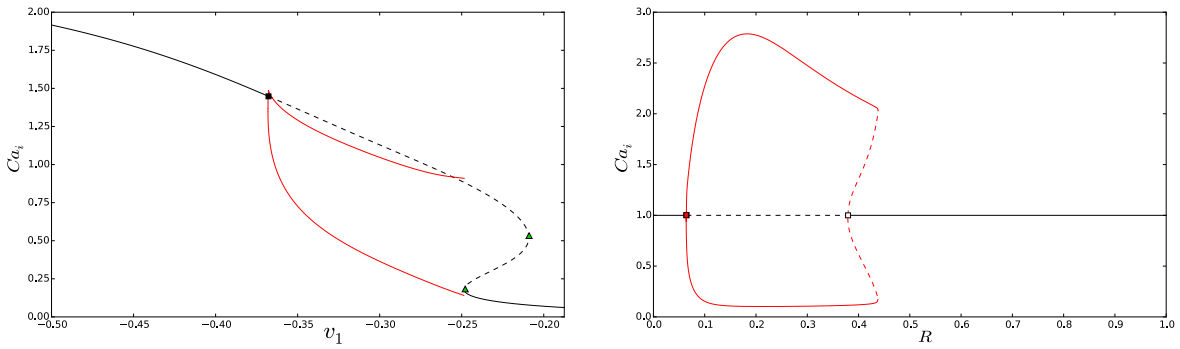

(a) Model by Gonzalez-Fernandez and Ermentrout (1994) with bifurcation parameter v_1

(b) Model by Meyer and Stryer (1988) with bifurcation parameter R

Figure 3.15: Bifurcation diagrams (with cytosolic Ca^{2+} concentration on the Y axis) of additional Ca^{2+} cell models detailed in Section 2.2. Both models contain an oscillatory domain for mid values of their respective parameters and an excitable domain adjacent to (specifically to the right of) the oscillatory domain. Black solid line: stable FP, black dashed line: unstable FP, red solid line: stable LC, red dashed line: unstable LC Red square: supercritical Hopf, white square: subcritical Hopf, green square: limit point (LP) bifurcation.

3.5 Summary

When varying the parameter β of Goldbeter et al. (1990) model (where β corresponds to the saturation function of the inotisol trisphosphate (IP_3) receptor and hence controls the rate of IP_3 induced Ca^{2+} release from the internal stores into the cytosol), the system will be either excitable, nonexcitable or oscillatory (see Figure 3.3). The excitability of the system is partly due to the shape of the nullclines in Figure 3.2; the nullclines determine the excitation threshold and location of the stable FP of the system.

When coupling together two cells with identical β values with some coupling strength D, the cells retain their original dynamics. Likewise two nonidentical nonexcitable, two nonidentical excitable, or an excitable coupled with a nonexcitable cell will retain the

dynamics of their uncoupled state. However an oscillatory coupled with a nonexcitable cell will cause the nonexcitable cell to oscillate with small amplitude when weakly coupled; their behaviour when strongly coupled is dependent on the dynamics of a cell with the average β value of the two cells. Two nonidentical oscillatory cells will experience variable amplitude oscillations when weakly coupled, and synchronise by oscillating with constant amplitude and frequency when strongly coupled. An oscillatory and excitable cell coupled together will cause the excitable cell to oscillate with small amplitude when weakly coupled. When the coupling strength exceeds some threshold value the Ca^{2+} flux from the oscillatory cell will be high enough to exceed the excitation threshold of the excitable cell, causing it to alternate between large and small amplitude oscillations. As the coupling strength increases both cells oscillate with variable amplitude and synchronise when strongly coupled. These coupled cell dynamics occur for each of the three SMC models.

Chapter 4

NVU Based SMC/EC Model

In this chapter the complex model of a neurovascular unit (NVU) constructed by Farr and David (2011) and extended by Dormanns et al. (2015) is adapted to model only the smooth muscle cell (SMC) and endothelial cell (EC) compartments, as the focus of this thesis is on the calcium (Ca^{2+}) dynamics in the SMC. This model and the process of neurovascular coupling (NVC) are detailed in Section 2.3. From here on we refer to a single SMC and EC as a SMC/EC unit. A single unit with the neuronal signal on or off is modelled by varying K_p, the K^+ concentration in the perivascular space (PVS). Including the process of functional hyperaemia into a SMC/EC model via this parameter K_p increases the versatility of the model while only adding a single additional flux from the PVS into the SMC/EC unit. Two adjacent units are then coupled via gap junctions in the SMCs and the parameters J_{PLC} and K_p are varied to produce different dynamics.

This SMC/EC model is compared to the minimal SMC Ca^{2+} models analysed in Chapter 3, in particular the simplest model based on Ca^{2+} induced Ca^{2+} release (CICR) by Goldbeter et al. (1990).

4.1 Method

The single and coupled systems are solved in Matlab using ODE15s, a solver for stiff systems such as the following model. A stiff system can intuitively be defined as a system containing multiple time scales. The more commonly used solver ODE45 is unsuitable for stiff systems as it can be numerically unstable unless the step size is extremely small, leading to a longer runtime.

The trajectory plots are all produced in Matlab and consist of the trajectories (plotted after some period of time so any transient behaviour may be ignored) of each unit as a projection of the phase space onto the (Ca_i, s_i) space. The bifurcation analysis is achieved using the continuation package AUTO (Champneys et al., 2002).

4.1.1 SMC/EC Model

The SMC/EC model based on the NVU model removes the neuron (NE), synaptic cleft (SC) and astrocyte (AC) compartments reducing the number of state variables from 24 to 14. These variables are: SMC cytosolic Ca^{2+} concentration (Ca_i), SMC Ca^{2+} concentration in the internal stores (s_i), SMC membrane potential (v_i), open state probability of Ca^{2+}-activated potassium (K^+) channels (w_i), SMC cytosolic inotisol trisphosphate (IP_3) concentration (I_i), SMC cytosolic K^+ concentration (K_i), EC cytosolic Ca^{2+} concentration (Ca_j), EC Ca^{2+} concentration in the internal stores (s_j), EC membrane potential (v_j), EC cytosolic IP_3 concentration (I_j), fraction of free phosphorylated cross-bridges (Mp), fraction of attached phosphorylated cross-bridges (AMp), fraction of attached dephosphorylated cross-bridges (AM), and vessel radius (R). The variable K_i (SMC cytosolic K^+ concentration) does not appear in any other differential equation, so if not needed it can be omitted to reduce the number of variables to 13.

The hydrolysis of phosphatidylinositol 4,5-bisphosphate by phospholipase-C (PLC) results in the formation of IP_3 which stimulates the release of Ca^{2+} from the internal stores of the EC. The flux of PLC in the EC is denoted J_{PLC}. This is our bifurcation parameter - when J_{PLC} is varied between 0 and 1 there are qualitative changes in the dynamics of the system.

The only connecting input in the NVU model from the NE, SC and AC compartments to the SMC/EC submodule is K_{p}, the K^+ concentration in the PVS. Neuronal activity causes an increase in K^+ concentration in the SC resulting in an increased K^+ uptake by the AC and consquently an efflux of K^+ into the PVS through the big potassium (BK) channel at the endfeet of the AC. Therefore neuronal activity will cause an increase in K^+ concentration in the PVS and K_p may be used as an input parameter for the neuronal signal in the SMC/EC model. This parameter K_{p} modifies the flux of K^+ through the inward rectifying potassium (KIR) channel at the interface of the PVS and SMC.

K_p has a very slight dependency on J_{PLC} in the full NVU model as follows: when the neuronal signal is on the minimum is $K_p = 9141$, the maximum is $K_p = 9277$, and the average (for $J_{PLC} \in [0, 1]$) is $K_p = 9176$. When the neuronal signal is off the minimum is $K_p = 3381$, the maximum is $K_p = 3404$, and the average (for $J_{PLC} \in [0, 1]$) is $K_p = 3395$. Hence we use $K_p = 9200$ corresponding to having the neuronal signal on and $K_p = 3400$ for neuronal signal off. In Section 4.2.3 it is shown that the bifurcation structure of the model does not qualitatively change within these two ranges.

4.1.2 Coupled SMC/EC Model

The two units are coupled through gap junctions between the SMCs. There are several options for coupling, namely Ca^{2+}, IP_3 and membrane potential V. We find that coupling

only Ca^{2+} is sufficient to induce synchronisation when strongly coupled and complex behaviour when weakly coupled. Adding IP_3 and/or V coupling makes little difference in behaviour and was therefore deemed unnecessary. Coupling with only IP_3 or only V does not allow synchronisation of the coupled units (results not shown). Therefore to couple the two SMC/EC units we include only a flux of Ca^{2+} to and from the SMCs of the coupled system. For simplicity any coupling term between the gap junctions of the two ECs has been omitted as there is no significant difference from just SMC coupling (results not shown).

The Ca^{2+} flux from SMC to SMC is modelled similarly to the coupling fluxes between the SMC and EC:

$$J^{SMC-SMC}_{Ca^{2+}coupling} = D(Ca_{i_1} - Ca_{i_2}), \tag{4.1}$$

where this flux is added or subtracted onto the two SMC Ca^{2+} differential equations:

$$\frac{dCa_{i_1}}{dt} = \ldots - J^{SMC-SMC}_{Ca^{2+}coupling}, \qquad \frac{dCa_{i_2}}{dt} = \ldots + J^{SMC-SMC}_{Ca^{2+}coupling}, \tag{4.2}$$

and D is the coupling coefficient with units of s^{-1}. The physiological value of the parameter D is unknown so a range of values are used.

When we couple two units we mainly consider them with different J_{PLC} values in the EC as in reality adjacent cells are not identical. The same value of K_p is used for both units but later we consider the possibility of two units with different K_p corresponding to different levels of neuronal activity in Section 4.3.3. There is no non-dimensionalisation for this model. As there are 14 variables it is not easily implemented like the previous 2D or 3D models studied in Chapter 3. The coupled SMC/EC model diagram depicting the various compartments and ion channels is shown in Figure 4.1.

4.2 Single SMC/EC Results

The resulting bifurcation diagrams of the system with both $K_p = 3400$ (neuronal signal off) and $K_p = 9200$ (neuronal signal on) are shown in Figure 4.2a for easy comparison. The period of oscillations for both cases are shown in Figure 4.2b.

4.2.1 Signal off ($K_p = 3400$)

The bifurcation diagram of the system with $K_p = 3400$ is denoted by red in Figure 4.2a. For low and high J_{PLC} the system tends to a stable fixed point (FP) while for medium values of J_{PLC} the system oscillates. The qualitative change in behaviour between stable and oscillatory is due to two supercritical Hopf bifurcations that change the stability of the FP from stable to unstable and generate stable limit cycles (LCs).

The period of the oscillations is given in Figure 4.2b, denoted in red. The period increases from the left Hopf and reaches a maximum at approximately $J_{\mathrm{PLC}} = 0.26$

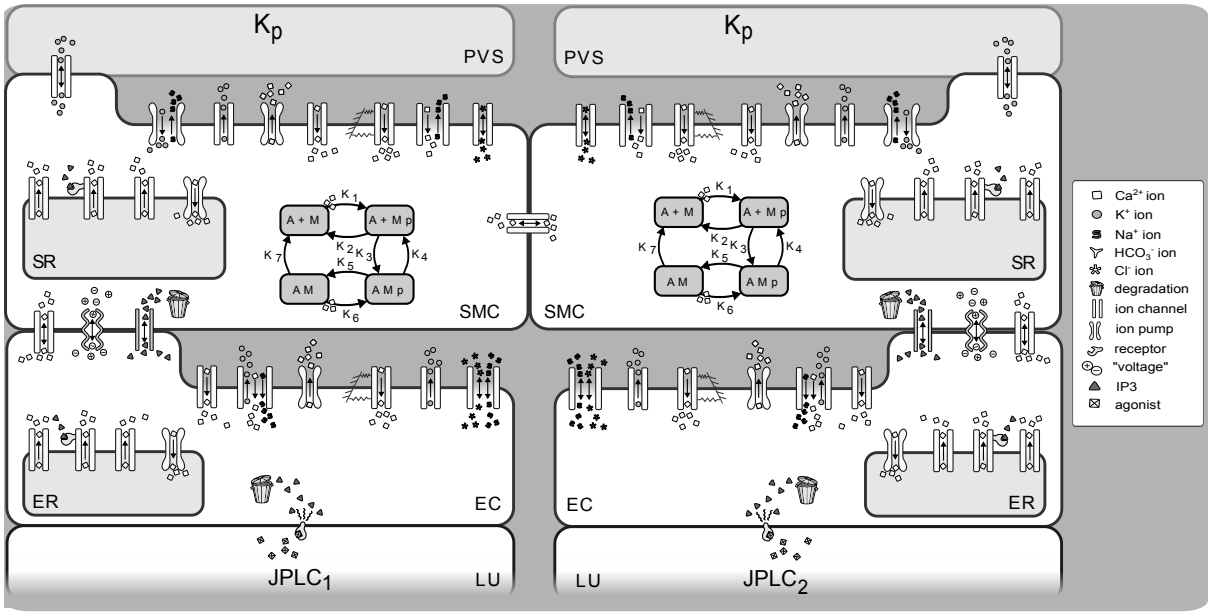

Figure 4.1: Schematic diagram of the SMC/EC coupled model based on the work of Farr and David (2011) and Dormanns et al. (2015). The two SMC/EC units are coupled via an intercellular flux of Ca^{2+} based on Fickian diffusion.

before decreasing as it approaches the right Hopf bifurcation. The period has a range of roughly 9 to 18 seconds.

4.2.2 Signal on ($K_p = 9200$)

The bifurcation diagram of the system with $K_p = 9200$ is denoted by blue in Figure 4.2a. The structure is qualitatively different from the previous case where the neuronal signal is off. The bifurcation diagram is explained as follows. Starting at $Ca_i = 0.217$ for $J_{PLC} = 0$ there is a line of stable FPs that become unstable at a supercritical Hopf bifurcation around $J_{PLC} = 0.06$, which generates a set of small amplitude stable LCs. These LCs then become unstable at a period doubling (PD) bifurcation. This PD bifurcation is a possible source of a stable set of LCs with double the period of the previous stable set of LCs, however this was only discovered towards the end of this research and as such may be determined in future work.

The unstable LCs are terminated when they collide with a line of FPs forming a homoclinic orbit. The line of unstable FPs generated by the Hopf bifurcation (at around $J_{PLC} = 0.06$) reverses direction at a LP bifurcation around $J_{PLC} = 0.14$ while still maintaining unstability. There exists a second line of stable FPs starting from close to $Ca_i = 0$ at $J_{\mathrm{PLC}} = 0$. The FPs become unstable at a supercritical Hopf bifurcation at approximately $J_{PLC} = 0.26$, which generates a set of stable large amplitude LCs. These LCs increase rapidly in amplitude before smoothly decreasing in amplitude as J_{PLC} increases, in a similar fashion to the bifurcation diagram based on the model by

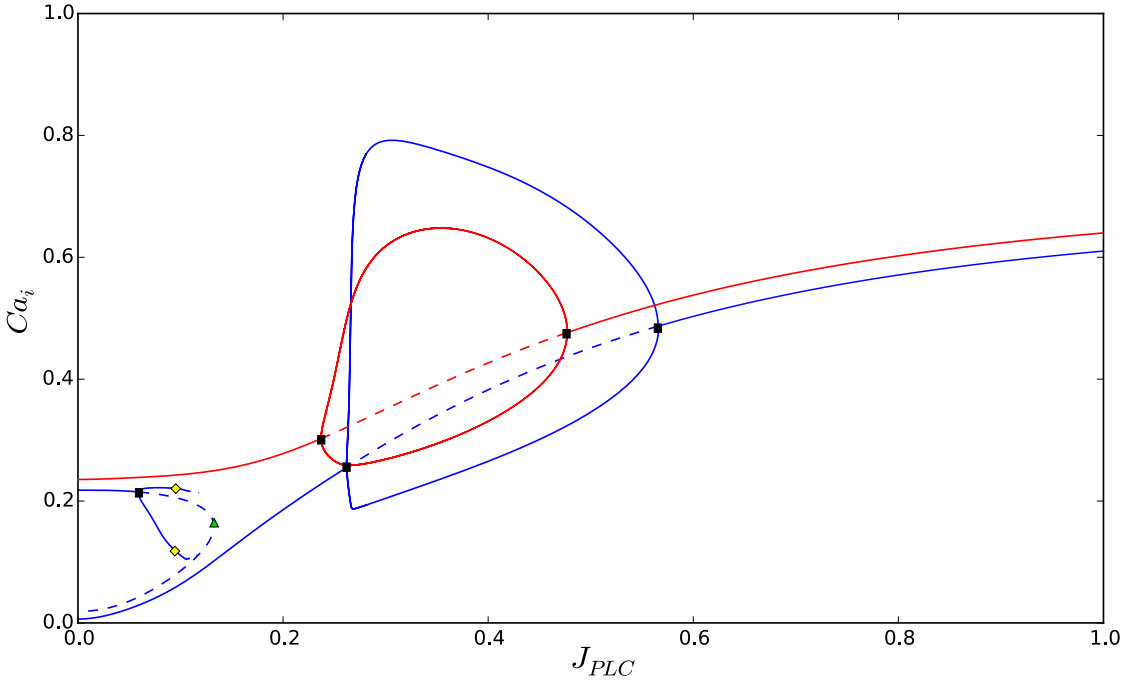

(a) Bifurcation diagram with J_{PLC} as the bifurcation parameter and the cytosolic SMC Ca^{2+} concentration on the Y axis.

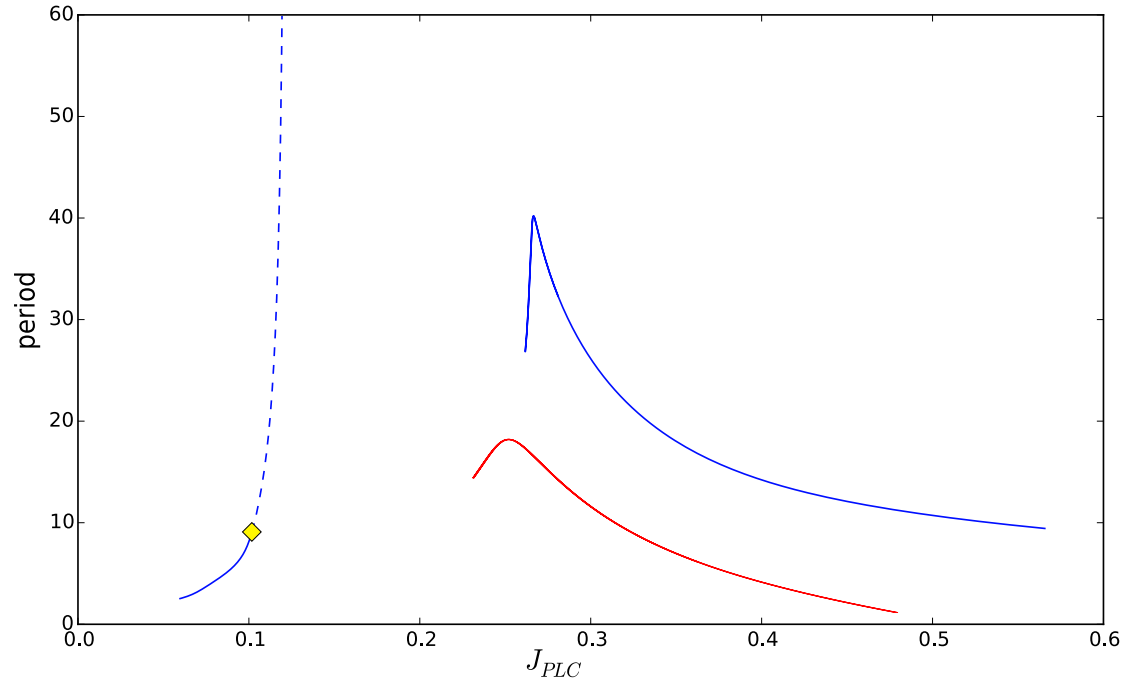

(b) Period of oscillations (note the different x axis scale to Figure 4.2a).

Figure 4.2: Different dynamics of the SMC/EC model (based on the NVU model by Farr and David (2011), Dormanns et al. (2015)) with the parameter J_{PLC} varied and the neuronal input signal either on or off, modelled by a change in the parameter K_p.
Red line: signal off ($K_p = 3400$), blue line: signal on ($K_p = 9200$). Solid: stable, Dashed: unstable. Black square: supercritical Hopf bifurcation, yellow diamond: Period Doubling (PD) bifurcation, green triangle: limit point (LP) bifurcation.

Goldbeter et al. (1990) in Section 3.2. The unstable line of FPs become stable again at a second supercritical Hopf bifurcation at approximately $J_{PLC} = 0.57$, and the stable LCs are terminated.

For small J_{PLC} less than approximately 0.06 there is bistability present as there are two stable FPs that exist. The Ca^{2+} concentration can either settle to a FP at approximately $Ca_i = 0.217$ or at a FP close to $Ca_i = 0$. For J_{PLC} between approximately 0.06 and 0.14 there is bistability present again as there exists one stable FP and one stable LC. The Ca^{2+} concentration will either oscillate with small amplitude or settle to a FP with lower Ca_i. Note that these two bistable domains do not exist when the neuronal signal is off.

The period of oscillations for both the small and large amplitude LCs found when $K_p = 9200$ are given in Figure 4.2b, denoted in blue. The period of the large amplitude LC when the neuronal signal is on has a range of about 10 to 40 seconds, approximately double than when the signal is off. The period of the small amplitude stable LC is less than 10 seconds. However as J_{PLC} approaches approximately 0.12 the period of the small amplitude unstable LC increases to infinity. This is characteristic of a homoclinic orbit where the LCs collide with the line of FPs and disappear. The period for the large amplitude LCs sharply increases from the Hopf bifurcation at $J_{PLC} = 0.26$ and reaches a maximum at approximately $J_{\mathrm{PLC}} = 0.27$, smoothly decreasing as J_{PLC} increases. This is similar to where the neuronal signal is off but with a steeper increase in period after the left Hopf bifurcation.

The sharp increase in amplitude and period of oscillations after the Hopf bifurcation is similar to the bifurcation diagram of the Goldbeter model in Section 3.2, especially when $K_p = 9200$. This suggests that the behaviour of the system for J_{PLC} close to the bifurcation may be similar to the Goldbeter model as well, i.e. the system will be excitable (see Section 2.2 for details on excitability). Simulations (not included) have shown that this is in fact correct, there is an excitable region for J_{PLC} close to the Hopf bifurcation but the exact size and range of this region has not been calculated.

However the system is only weakly excitable when the neuronal signal is turned off ($K_p = 3400$), meaning the 'spike' of Ca^{2+} produced by an initial perturbation to the system (such as a small input of Ca^{2+}) will not be as large as that produced when the neuronal signal is on ($K_p = 9200$). It appears the steeper the increase in amplitude and period of oscillations after the Hopf bifurcation in the SMC/EC model and the SMC model by Goldbeter et al. (1990), the more excitable the system (i.e. a larger range of J_{PLC} where the system is excitable, lower excitation threshold and larger 'spike' produced by an initial perturbation over this threshold).

In general the amplitude and period of Ca^{2+} oscillations in a SMC increase when neuronal activity is increased, however the location of the FPs are higher for the case when the neuronal signal is off. Therefore if a SMC/EC unit is oscillatory, neuronal activity simulated by an input signal will cause the unit to oscillate with greater amplitude and period. However if a SMC/EC unit is steady state then neuronal activity will cause the Ca^{2+} concentration to drop.

4.2.3 Varied K_p

The bifurcation structure for this model is qualitatively different depending on whether the neuronal input signal is on or off, hence by varying the input K_p as second bifurcation parameter the manner in which the structure changes can be revealed. In addition, when the neuronal signal in the full NVU model is turned on or off the increase or decrease in K_p is a smooth process, so it is useful to know the dynamics of the system for other values of K_p within the range of $[3400, 9200]$.

The parameters J_{PLC} and K_p are both varied as bifurcation parameters in $[0, 1]$ and $[3000, 10500]$ respectively, in order to produce a codimension 2 bifurcation diagram detailing the dynamics of the system at a certain point in the (J_{PLC}, K_p) parameter space (e.g. oscillatory, stable, bistable, etc.) and the locations of the codimension 1 bifurcations (e.g. Hopf, LP, etc.). This diagram is shown in Figure 4.3, and Figure 4.4 provides a closer view of the upper left parameter space.

The different domains are colour coded for ease of understanding. A white background indicates a stable region, yellow indicates an oscillatory region, blue indicates a bistable FP region containing two stable FPs, and green indicates a bistable oscillatory/FP region containing a stable FP and a stable LC. The various codimension 1 bifurcations are also colour coded. A Hopf bifurcation is represented by a blue line, a LP bifurcation by a red line, a homoclinic orbit by a green line, and a PD bifurcation by a black line. There exist two codimension 2 bifurcations; the Cusp (CP) bifurcation is denoted by a white triangle and the Bogdanov-Takens (BT) bifurcation is denoted by a white circle. A codimension 2 bifurcation is essentially a 'bifurcation of a bifurcation', i.e. a point in 2 parameter space where a codimension 1 bifurcation qualitatively changes its behaviour. The domains are labelled in black Roman numbers and the areas of K_{p} where the signal is either on or off are denoted by dotted black lines.

The range of K_p with signal on is $[9141, 9277]$ (minimum and maximum values previously given in Section 4.1). This range has qualitatively the same behaviour, namely a bistable FP region and bistable oscillatory/FP region for small J_{PLC} and an oscillatory region for mid J_{PLC}. The range of K_p for signal off is $[3381, 3404]$ and is also qualitatively the same, containing two stable regions for low and high J_{PLC} and an oscillatory region for mid J_{PLC}.

Domains I and III contain a single stable FP and cover the majority of the param-

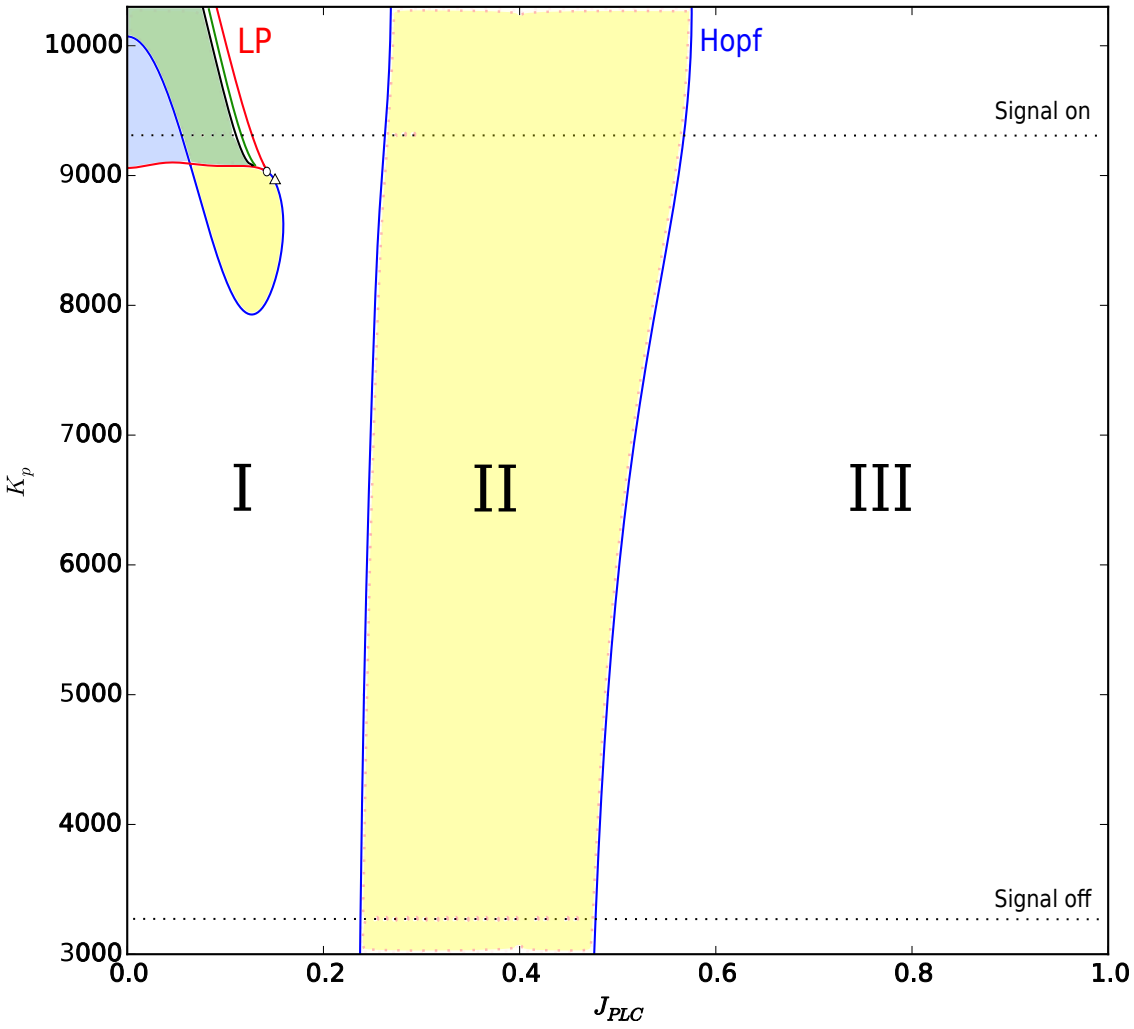

Figure 4.3: Codimension 2 bifurcation diagram of the (J_{PLC}, K_p) parameter space. The space is subdivided into domains of different dynamics by various codimension 1 bifurcations such as Hopf and LP bifurcations. There is an excitable subdomain to the left of the Hopf seperating domain I and II, not shown as the exact size has not been calculated.
White area: stable, yellow area: oscillatory, blue area: bistable FPs, green area: bistable oscillatory/FP. Blue line: supercritical Hopf bifurcation, red line: LP bifurcation.

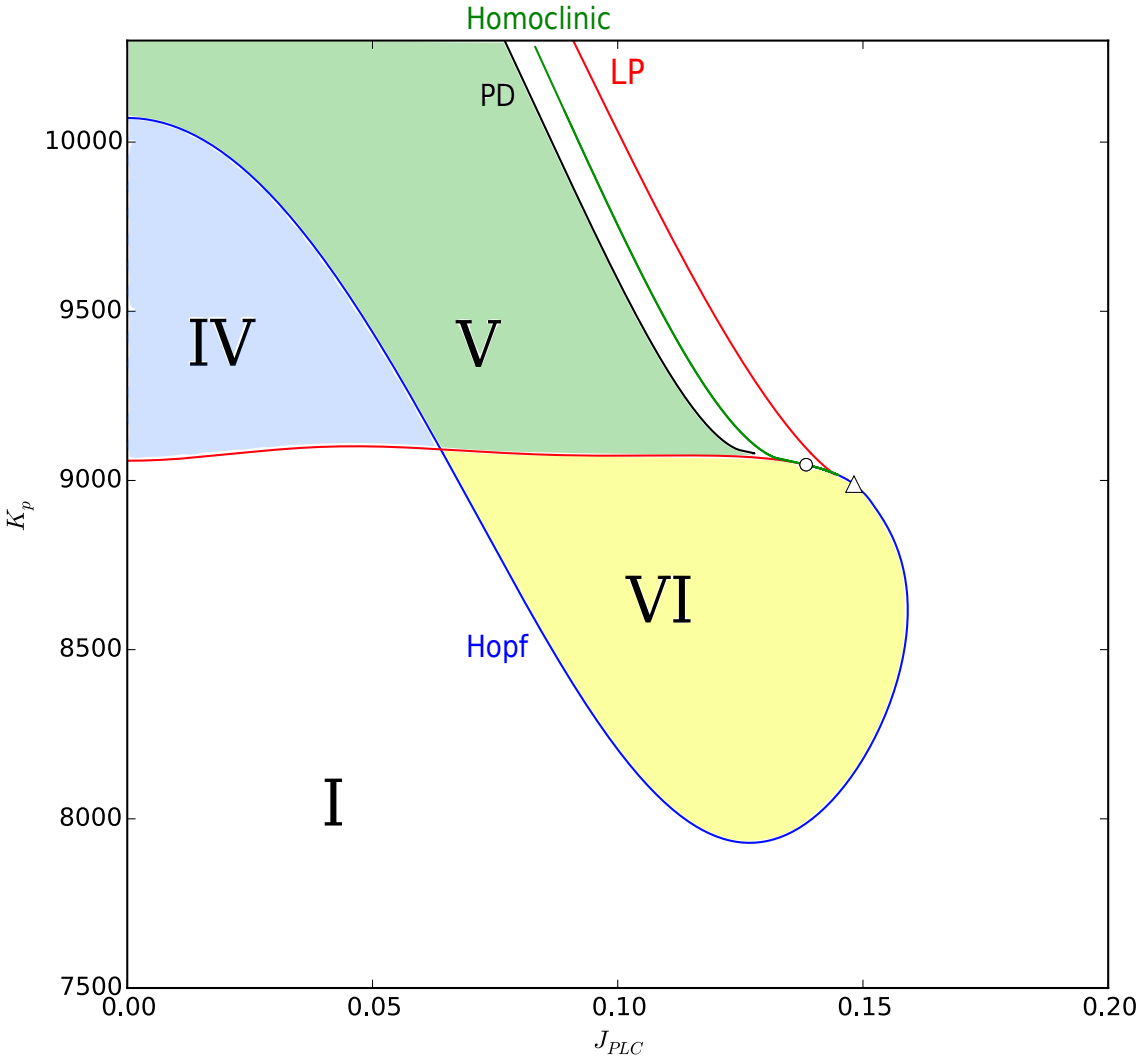

Figure 4.4: Zoomed view of Figure 4.3 for small J_{PLC} and high K_p. This area corresponds to high neuronal activity and low J_{PLC} (i.e. IP_3 production in the EC). There are small amplitude oscillations (green and yellow areas) and bistability (blue area) present. White area: stable, yellow area: oscillatory, blue area: bistable FPs, green area: bistable oscillatory/FP. Blue line: supercritical Hopf bifurcation, red line: LP bifurcation, black line: PD bifurcation, green line: homoclinic bifurcation. White triangle: Cusp (CP) bifurcation, white circle: Bogdanov-Takens (BT) bifurcation

eter space. The large oscillatory domain II contains a stable LC and unstable FP and is separated by two lines of supercritical Hopf bifurcations. The right line of Hopf bifurcations shifts to the right as K_p increases and the left line also shifts slightly to the right. These different domains of stability can result in the system changing behaviour as the neuronal signal (and hence K_p) is varied. For example, a SMC/EC unit with J_{PLC} = 0.5 and the neuronal signal turned off ($K_p = 3400$) will pass from domain III to II via a Hopf bifurcation when K_p is increased (i.e. neuronal signal is turned on), qualitatively changing the behaviour from stable to oscillatory.

Domain II corresponds to the large amplitude oscillations from the bifurcation diagrams in Figure 4.2a. The period, amplitude and maximum value of oscillations all increase as K_p increases. The steepness of the increase in period and amplitude after the left Hopf bifurcation also increases with K_p.

The excitable domain of the system is a subset of domain I adjacent to the Hopf bifurcations seperating domains I and II. The exact range has not been calculated so it is not shown in Figure 4.3.

The area of low J_{PLC} and high K_p (see Figure 4.4) corresponds to high neuronal activity with low IP_3 production in the EC. This is a physiologically relevant case and interesting because these small oscillations present are not found when the neuronal signal (and hence K_p) is low. These oscillations may be due to the stretch activated Ca^{2+} channels in the SMC (see the work of Dormanns et al. (2015) for more details on these channels). When these stretch channels are turned off all bifurcations in the upper left corner of the parameter space in Figure 4.3 disappear, leaving only the stable domain I. There are also stretch activated channels located in the EC. Turning only these off or turning them off in addition to the SMC channels makes no qualitative difference, so it seems only the SMC stretch channels are necessary for the small amplitude oscillations to appear.

In Figure 4.4 there are 4 distinct domains, each with different dynamics. Domain I is the large region with a single stable FP, seen fully in Figure 4.3. Domain IV contains 2 stable FPs and one unstable FP, making it bistable. It is separated from domain I by a line of LP bifurcations, and seperated from domain V by a line of Hopf bifurcations. The line of LP bifurcations sharply changes direction at a CP bifurcation, while the line of Hopf bifurcations is terminated by a BT bifurcation. At this point the Hopf bifurcations become neutral saddles with no noticeable effect on the dynamics.

Domain V contains a stable LC, a stable FP, and 2 unstable FPs. This makes it the second bistable domain as the system can either tend to the stable LC or to the stable FP depending on the initial conditions (ICs). It is separated from the stable domain I by a line of PD bifurcations and from domain VI by the line of LP bifurcations. Finally

domain VI contains a stable LC and 1 unstable FP, making it a purely oscillatory region. It is separated from domain I by Hopf bifurcations.

If we consider a SMC/EC unit with some fixed J_{PLC} and turn the neuronal signal from off to on (smoothly increasing K_p from 3400 to 9200) the general behaviour is as follows. For a unit with low J_{PLC} in domain I, increasing K_p results in either a small decrease in Ca^{2+} or a change in behaviour to small amplitude oscillations, depending on where J_{PLC} lies in the parameter space (Figure 4.3). For an oscillatory unit with mid J_{PLC} in domain II, increasing K_p results in an increase in the period, amplitude and maximum value of Ca^{2+} oscillations. For a unit with high J_{PLC} in domain III, increasing K_p results in only a very small decrease in SMC Ca^{2+} concentration.

4.3 Coupled SMC/EC Results

In this section we consider the coupled SMC/EC model containing two SMCs and two ECs. The neuronal input parameter K_{p} is initially kept the same for each SMC/EC unit and the parameter J_{PLC} controlling the rate of IP_3 production in the EC is varied for each unit. As with the previous models we consider two coupled SMC/EC units with reasonably close J_{PLC} values, as adjacent SMCs will not have any large variation between them. Units with identical J_{PLC}, J_{PLC} in the same domain, and J_{PLC} in different domain are considered. The various domains are of different types: stable (either nonexcitable or excitable), bistable FP, bistable oscillatory/FP, and oscillatory.

4.3.1 Coupled SMC/EC Units in the Same Domain

In this section we consider coupled units with their corresponding J_{PLC} values in the same domain, where the various domains I to VI are shown in Figures 4.3 and 4.4.

Two identical SMC/EC units produce no interesting behaviour; the basic behaviour is the same as when uncoupled. This conforms with the behaviour of identical cells in the previous simpler models studied in Chapter 3.

Stable

Two coupled SMC/EC units in the same stable or bistable FP domain will continue to be stable for any coupling strength D. The FPs of the two units move closer together in the phase space as D increases.

Oscillatory

Figures 4.5 show the behaviour for two coupled oscillatory SMC/EC units in domain II by plotting the trajectories in the (Ca_i, s_i) space for multiple values of the coupling strength

D. Domain II contains large amplitude stable LCs and covers the area in the parameter space where J_{PLC} is mid range. For low coupling strength D the units oscillate with variable amplitude indicated by the additional 'loops' of the trajectory, and for higher coupling strength D the units synchronise and oscillate with the same frequency.

The exact point at which the units synchronise can be seen by plotting the difference in power spectra of the SMC cytosolic Ca^{2+} concentration of each unit for different values of D, where the power spectrum is the distribution of the frequencies that compose an oscillatory function (see Section 3.3.1 for further details on power spectra). The difference in power spectra is shown in Figure 4.6. As the coupling strength D increases more frequencies are introduced corresponding to additional loops in the trajectories. At approximately $D = 0.056$ the lines of frequency coalesce in groups into single frequencies, indicating the cells are synchronised with a difference only in the amplitude of their respective frequencies.

Two coupled oscillatory units in domain VI behave the same way, oscillating with variable amplitude for low coupling and synchronisation occuring for strong coupling. These trajectory plots and the power spectrum graph are very similar to that of two coupled oscillatory SMCs in the previous models of Chapter 3. For a more in depth and detailed analysis of this behaviour refer to Section 3.3.1.

Bistable Oscillatory/FP

Domain V is bistable as it contains both a stable FP and LC, meaning a SMC/EC unit with J_{PLC} and K_{p} in this domain can either be stable or oscillatory depending on the ICs.

Two stable units when coupled will remain stable. One stable unit and one oscillatory unit will in general both oscillate for weak coupling D and when more strongly coupled they both either oscillate or tend to a stable state.

Two oscillatory units in this bistable domain act similarly to other coupled oscillatory units in Section 4.3.1, coupled oscillatory SMCs using the model by Goldbeter et al. (1990) in Section 3.3.1, and coupled oscillatory cells using the two other models discussed in Section 3.4. For weak coupling the units oscillate with variable amplitude as shown in in Figure 4.7. However the trajectories are more complex and the power spectrum graph has additional components, such as the frequency shift around $D = 0.27$ (see Figure 4.8). This is most likely due to the shape of the trajectories when the cells are initially uncoupled at $D = 0$. The SMC Ca^{2+} concentration in the internal store oscillates twice for every oscillation of the SMC cytosolic Ca^{2+} concentration forming a LC in a figure-of-8 shape. This is unlike the previous simple LCs of the oscillatory domains II and VI and is possibly caused by the bistability in this domain that is not present in any other cases.

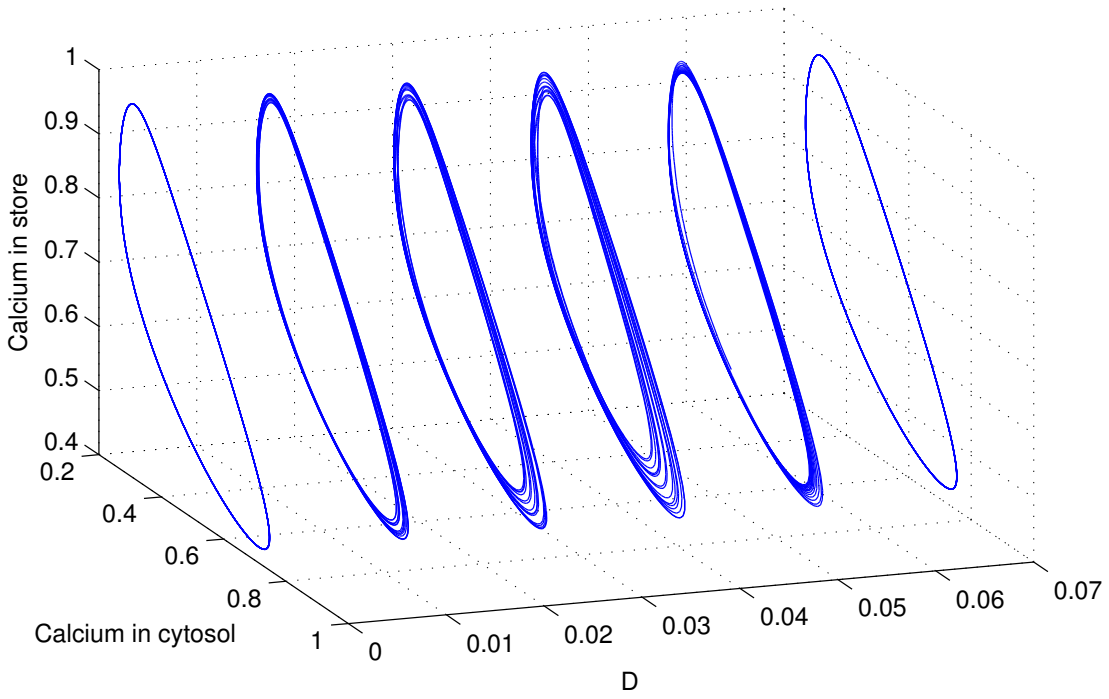

(a) Oscillatory cell 1.

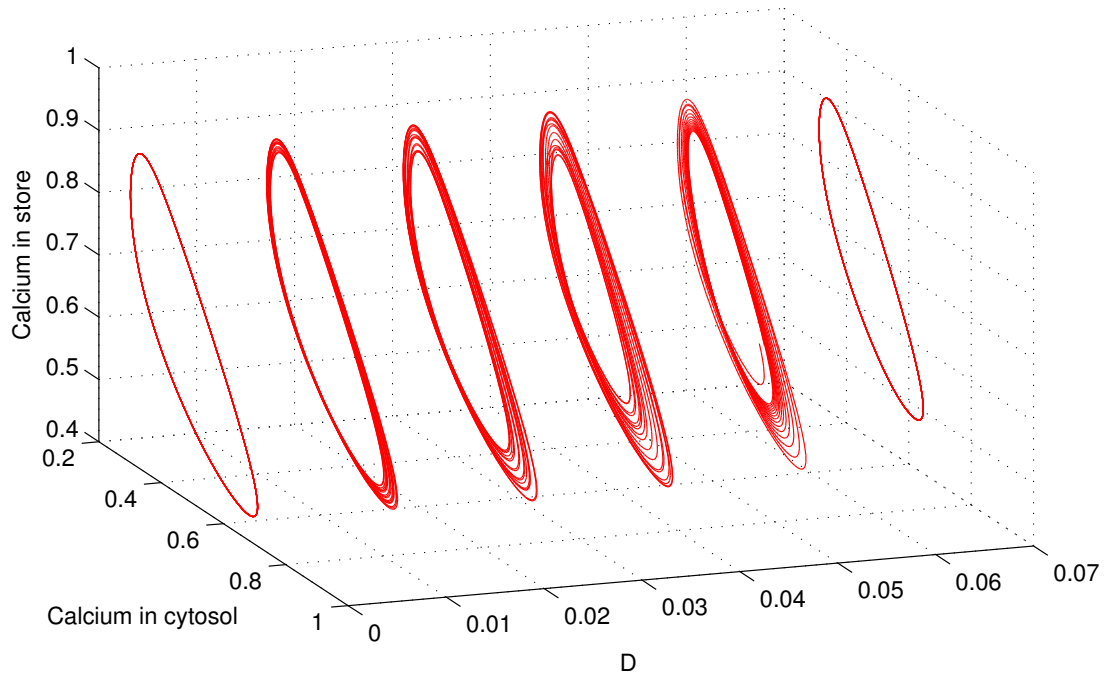

(b) Oscillatory cell 2.

Figure 4.5: Two coupled oscillatory units in domain II with $K_p = 9200, J_{PLC1} = 0.4, J_{PLC2} = 0.45$. The units oscillate with variable amplitude when D is low and synchronise when the coupling strength D is high enough.

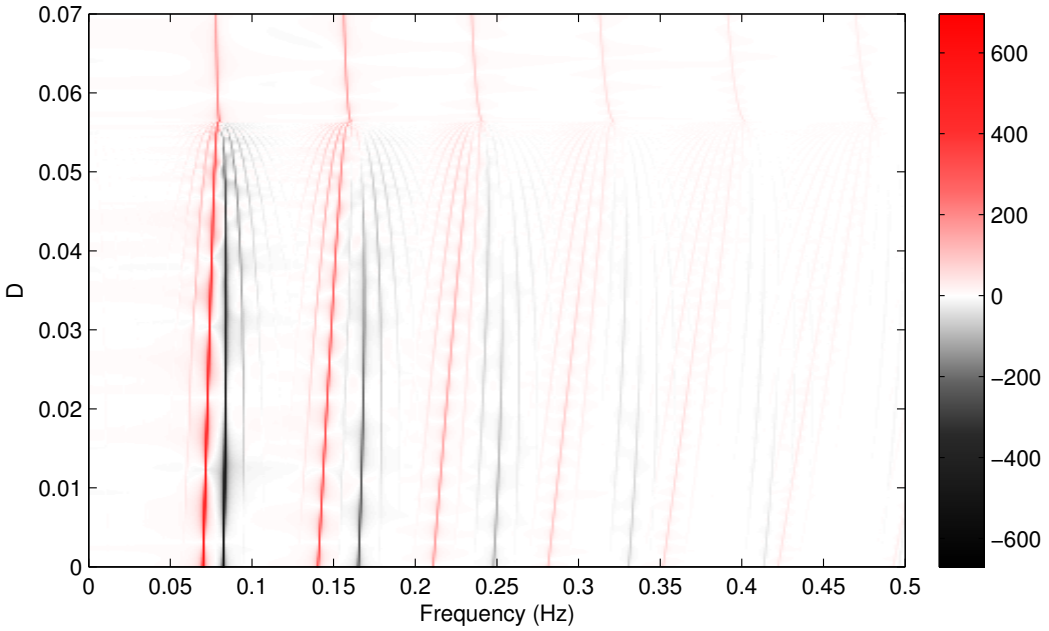

Figure 4.6: The difference in power spectra (unit 1 minus unit 2) between the Ca_i of two oscillatory units in domain II as the coupling strength D varies, where $K_p = 9200, J_{PLC1} = 0.4, J_{PLC2} = 0.45$. The variable amplitude oscillations of Figure 4.5 are represented by additional lines of frequency coalescing at approximately $D = 0.056$ where the units synchronise with identical frequency.

4.3.2 Coupled SMC/EC Units in Different Domains

The different domains of stability can be further categorised into excitable, nonexcitable, and oscillatory. A SMC/EC unit with parameter values for J_{PLC} and K_p in the bistable oscillatory/FP domain V will fall under nonexcitable or oscillatory depending on the ICs. Recall that the excitable domain is a subset of the stable domain I and located directly to the left of the line of Hopf bifurcations seperating domains I and II.

Excitable and Nonexcitable

Two coupled units where one is excitable and one is nonexcitable will produce no interesting behaviour as both are stable. This conforms with the behaviour of an excitable and nonexcitable cell in Section 3.3.2 using the SMC model by Goldbeter et al. (1990).

Oscillatory and Nonexcitable

By weakly coupling two units where one is oscillatory and one is nonexcitable, the flux of Ca^{2+} from the oscillatory into the nonexcitable unit will cause it to immediately oscillate with small amplitude and the same frequency. As the coupling strength D increases the amplitude of oscillations of the nonexcitable cell increases as it becomes more similar to

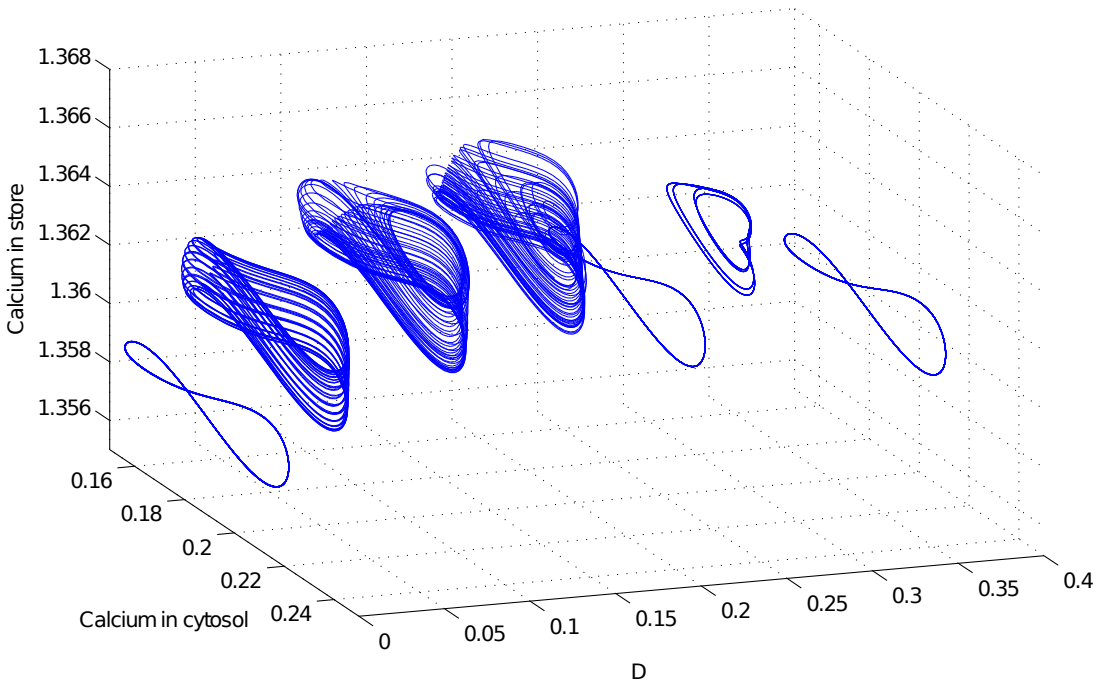

(a) Oscillatory cell 1.

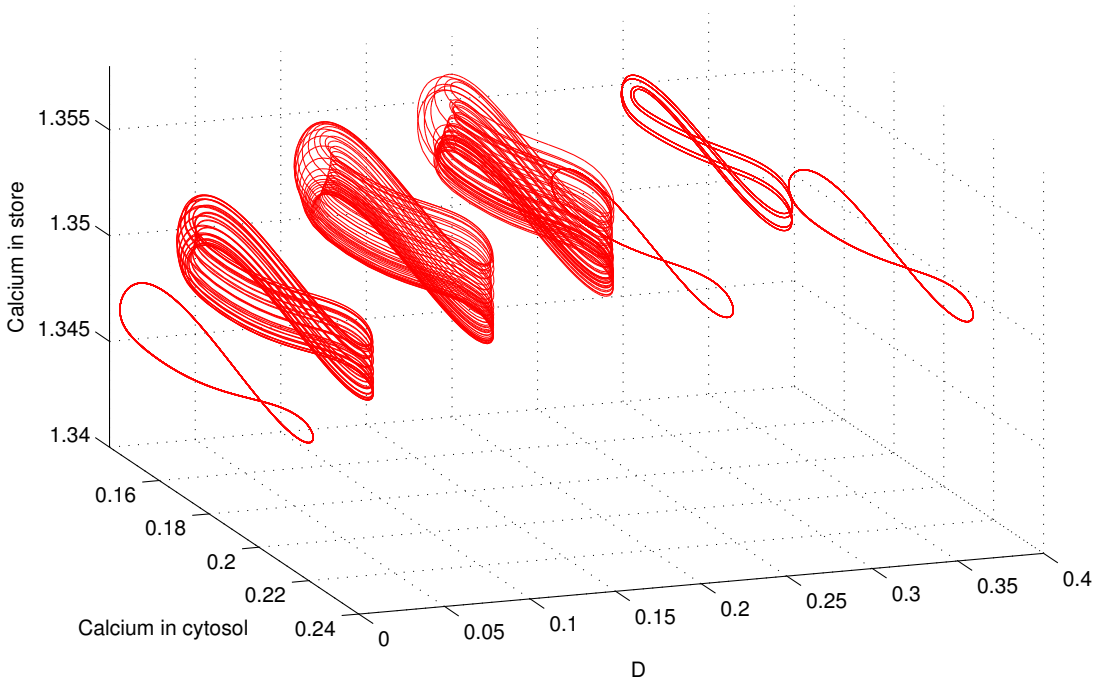

(b) Oscillatory cell 2.

Figure 4.7: Two oscillatory coupled SMC/EC units in the bistable domain V with $K_p = 9200, J_{PLC1} = 0.08, J_{PLC2} = 0.085$. The two units oscillate in a 'figure-of-8' shape when $D = 0$ and oscillate with variable amplitude and complex trajectories, before again oscillating in a 'figure-of-8' shape when the units are synchronised.

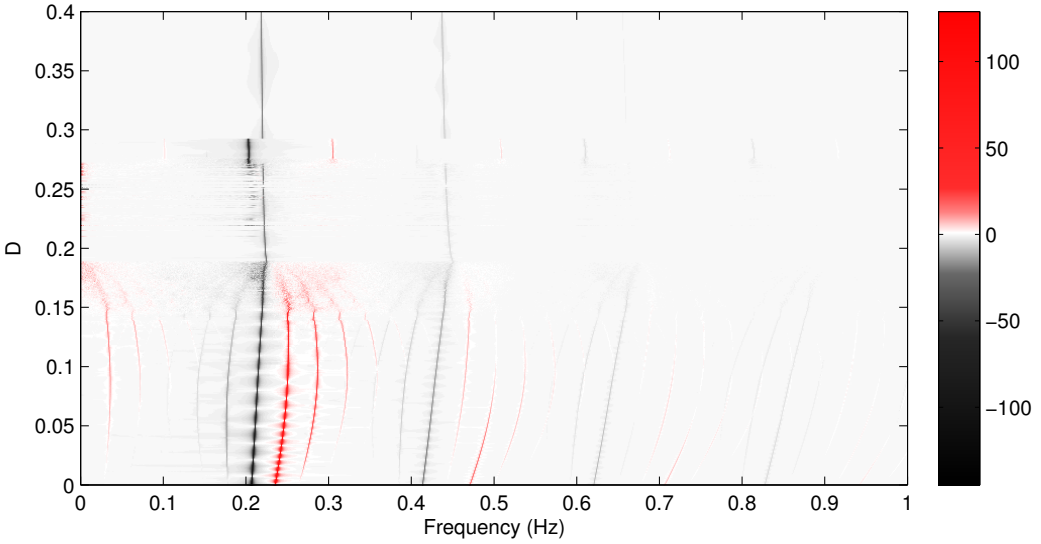

Figure 4.8: The difference in power spectra between the Ca_i of two oscillatory NVUs as the coupling strength D varies, where $K_p = 9200, J_{PLC1} = 0.08, J_{PLC2} = 0.085$. The frequency distribution is similar to Figure 4.6 where the different frequencies coalesce at some threshold value of D and the units synchronise with identical frequency.

the oscillatory cell. If the average J_{PLC} lies in a stable domain then the units will tend to a stable state when strongly coupled, whereas if the average J_{PLC} lies in an oscillatory domain then the units will oscillate when strongly coupled. Again this behaviour conforms with results in Section 3.3.2 using the SMC model by Goldbeter et al. (1990).

Oscillatory and Excitable

Figures 4.9 shows the behaviour of two coupled SMC/EC units where one is oscillatory and one is excitable. The average of the two J_{PLC} values lies in the oscillatory domain II so when the units are strongly coupled they will both be oscillatory.

When the coupling strength is less than $D = 0.02$ the flux of Ca^{2+} from the oscillatory to the excitable unit is small and the excitable unit starts to oscillate with small amplitude. At some threshold value of D the influx of Ca^{2+} to the excitable unit will cause the SMC cytosolic Ca^{2+} concentration to exceed the excitation threshold and the trajectory of the excitable cell will make a large excursion in the phase space in the form of a large amplitude oscillation followed by several smaller amplitude oscillations. By increasing D further both units will oscillate with variable amplitude. At approximately $D = 0.19$ the units synchronise and tend to simple LCs with the same frequency.

These trajectory plots are very similar to that of an excitable and oscillatory cell using the model by Goldbeter et al. (1990); see Section 3.3.2 for a more in depth and detailed analysis of this behaviour.

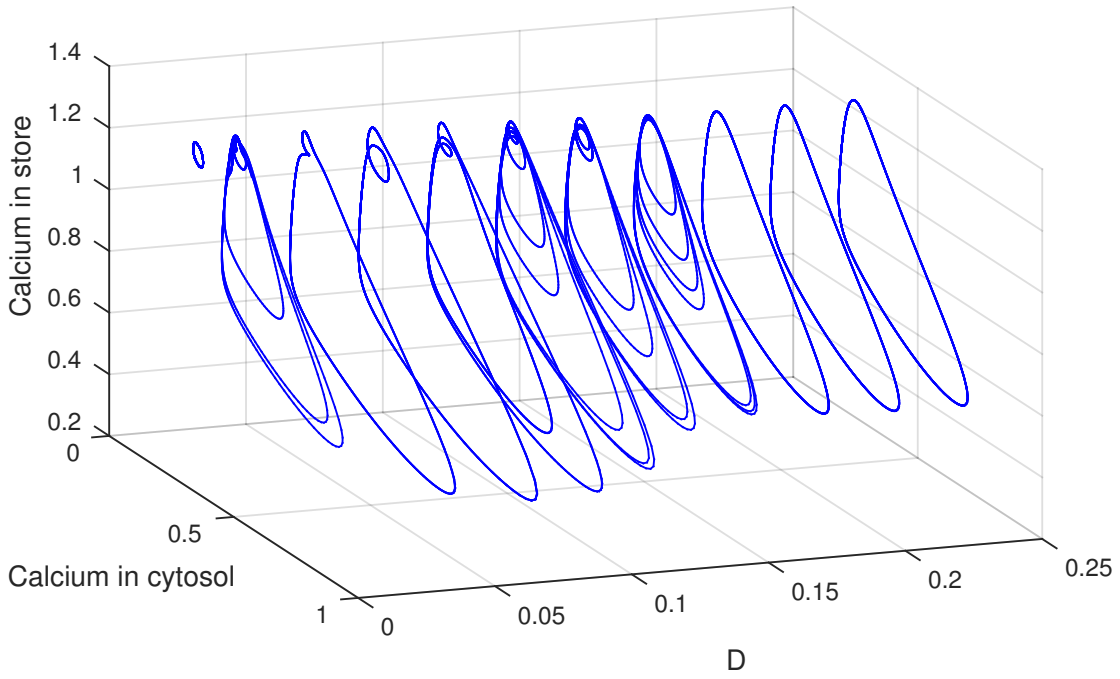

(a) Excitable cell 1.

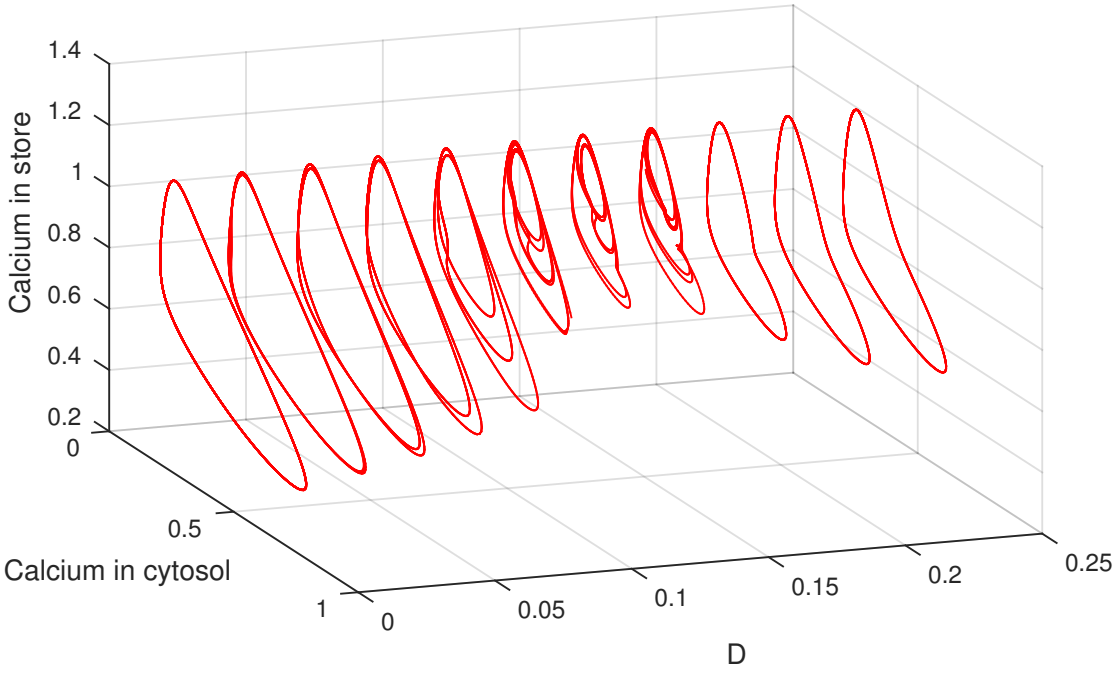

(b) Oscillatory cell 2.

Figure 4.9: Two coupled SMC/EC units from domains I and II with $K_p = 9200, J_{PLC1} = 0.25, J_{PLC2} = 0.3$. When the coupling strength D reaches some threshold the flux of Ca^{2+} from the oscillatory to the excitable unit is enough to exceed the excitation threshold, causing the excitable unit to oscillate with large amplitude. Both then oscillate with variable amplitude before synchronising with a common frequency.

4.3.3 Different K_p

If we consider two coupled SMC/EC units with different values of K_p and hence different levels of neuronal activity, it is trivial to find the behaviour induced by coupling based on the previous cases. To do so simply consider where the J_{PLC} and K_{p} values of each unit lie in the parameter space (Figure 4.3). If they both lie in an oscillatory domain (domains II, V, VI) they will have the corresponding behaviour of two coupled oscillatory units described earlier, and so on.

4.4 Summary

For any level of neuronal activity (K_p) the system tends to a stable state for high J_{PLC} and oscillates for medium values of J_{PLC}; the amplitude and period of these oscillations increase with neuronal activity (K_p). For a stable unit with high J_{PLC} increasing K_p results in a very small decrease in SMC Ca^{2+} concentration.

For low J_{PLC} and low to medium neuronal activity (K_p) the system tends to a stable state. For low J_{PLC} and high neuronal activity (K_p) the system can also oscillate. The amplitude and period of these oscillations are small compared to the oscillations present for medium values of J_{PLC}.

The behaviour between two coupled units in this model is dependent on their behaviour when uncoupled. They can be catagorised into the following three groups: nonexcitable, excitable and oscillatory. Note that the excitable region in the (J_{PLC}, K_p) parameter space is a section of domain I directly to the left of the line of Hopf bifurcations separating domains I and II.

Two nonexcitable units will remain nonexcitable when coupled and two excitable units will remain excitable when coupled. All coupled oscillatory SMC/EC units have the same type of behaviour and power spectrum, i.e. oscillations that vary in amplitude and increase in complexity for small coupling strength D. The complexity disappears at some value of D and the units synchronise by oscillating at the same frequency. The SMC/EC units with parameters J_{PLC} and K_p in domain V have the most complex trajectories, possibly because of the bistability present in the domain.

A coupled nonexcitable unit and excitable unit will remain stable. A nonexcitable unit coupled with an oscillatory unit will oscillate when weakly coupled and either be stable or oscillatory when strongly coupled depending on the average J_{PLC} of the two units.

An excitable unit coupled with an oscillatory unit will cause the excitable unit to transition through the following stages as the coupling strength is increased: small amplitude oscillations, variable amplitude oscillations, and finally fixed amplitude oscillations when strongly coupled. The oscillatory unit will transition through variable amplitude oscilla-

tions to fixed amplitude oscillations when strongly coupled.

The behaviour of the SMC cytosolic Ca^{2+} concentration of two coupled SMC/EC units (excitable, nonexcitable, and oscillatory) is qualitatively the same as that of two coupled SMCs in Section 3.3 using the model by Goldbeter et al. (1990). The only components present in the SMC/EC model not found in the Goldbeter model are the small amplitude oscillations and bistability for low J_{PLC} and high neuronal activity (K_p), believed to exist due to the stretch activated Ca^{2+} channels not included in the simpler Goldbeter model. Therefore the majority of the dynamics of this coupled SMC/EC model containing a total of 28 individual ordinary differential equations (ODEs) may be explained by the dynamics of the Goldbeter minimal coupled cell model containing only 4 ODEs.

Chapter 5

Wave Propagation in Spatial Media

In this chapter we investigate the dynamics of reaction diffusion systems with propagating waves on a flat two dimensional (2D) plane with periodic boundary conditions (BCs) on all boundaries of the domain. The two models chosen are the generic model by FitzHugh (1961) as it is a classical excitable system and the calcium (Ca^{2+}) dynamics model by Goldbeter et al. (1990) as it is the simplest Ca^{2+} model studied thus far with known excitable properties (Wilkins and Sneyd, 1998), and has the most similarity in behaviour to the more complex SMC/EC model of Chapter 4.

A population of cells will rarely be identical in nature, therefore it is of interest to look at surfaces with the local dynamics of the system varied, controlled by the spatially varied parameter β. Hence this chapter contains simulations on a flat surface with periodic BCs and constant or spatially varying parameter β (controlling the stability and excitability of the system), while in following chapter the models are simulated on a curved surface, namely a torus.

5.1 Method

A 2 variable partial differential equation (PDE) system on a continuous 2D spatial domain is transformed into a set of 2 ordinary differential equations (ODEs) for each mesh point with Fickian diffusion (via the Laplace operator) connecting each point, numerically solved using the method of lines. The spatial coordinates are discretised as follows:

$$x_i = x_0 + i\delta x,\ i = 0, 1, \ldots, I \tag{5.1}$$

$$y_j = y_0 + j\delta y,\ j = 0, 1, \ldots, J \tag{5.2}$$

for an $I \times J$ mesh. Then the ODEs for each mesh point in the FitzHugh-Nagumo (FHN) model are

$$\frac{du_{i,j}}{dt} = 3u_{i,j} - (u_{i,j})^3 - v_{i,j} + D\Delta u_{i,j} \tag{5.3}$$

$$\frac{dv_{i,j}}{dt} = \varepsilon(u_{i,j} + \beta), \tag{5.4}$$

where $u_{i,j} := u(x_i, y_j)$, and similarly for the Goldbeter model. The Laplace operator in Cartesian coordinates is approximated by

$$\Delta u_{i,j} = \frac{\partial^2 u_{i,j}}{\partial x^2} + \frac{\partial^2 u_{i,j}}{\partial y^2} \approx \frac{u_{i+1,j} - 2u^n_{i,j} + u_{i-1,j}}{(\delta x)^2} + \frac{u_{i,j+1} - 2u_{i,j} + u_{i,j-1}}{(\delta y)^2}. \tag{5.5}$$

There are two ODEs per mesh point for both models, producing a $2 * I * J$ dimensional ODE system. This large set of ODEs is solved in C using the library ARKode provided by SUNDIALS (Hindmarsh et al., 2005). ARKode is an adaptive-step additive Runge Kutta solver for initial value problems capable of solving systems both explicitly and implicitly by partitioning the right hand side (RHS) of the system into 'slow' time scale and 'fast' time scale components respectively. Our simulations were run using only the explicit solver; as both models used only contained two state variables it was deemed unnecessary, however if a more complex model were to be used then the runtime of the solver could be optimised by making use of the explicit and implicit additive solver.

Message Passing Interface (MPI) is used to parallelise the code, enabling faster computation by running on multiple cores. MPI is a standardised message passing library designed to function on a variety of parallel computers (Walker, 1994). The spatial domain with mesh size $I \times J$ is split into multiple quads with neighbouring quads exchanging information on their edge points after each time iteration. The number of quads determines how the domain is subdivided using a built in MPI function which decides the optimal way to subdivide the domain. For example a mesh of 200×800 run on 4 cores would be split into quads of size 100×400. Our simulations were reasonably small so they could be achieved on a local computer using only 4 quads. The 2D visualisations are produced in Python. The source code for this project can be found at www.github.com/BlueFern/CRDModel. All generated videos corresponding to the figures in this chapter can be found at the UC High Performance Computing YouTube channel at http://bit.ly/1TgPNgq.

5.1.1 Spatially constant β

To investigate propagating waves using the Goldbeter model where the domain is spatially constant (i.e. when the parameter β is constant) an initial perturbation to the system is simulated by setting the values of the initial conditions (ICs) higher in a small rectangular area (specifically $Z_s + 1, Y_s + 1$ corresponding to a supra-threshold excitation) than on the rest of the plane (set to Z_s, Y_s, the stable fixed point (FP) of the system). This perturbation will cause a wave to propagate throughout the medium if the system is excitable. For simulations with spatially constant β the spatial domain is set to $x \in [0, 40]$, $y \in [0, 40]$.

The x boundary is periodic. There are additional Dirichlet BCs at the lower and upper y boundaries for time $t < T_{BOUNDARY}$, where $T_{BOUNDARY}$ is large enough so that

a backward travelling wavefront generated by an initial perturbation is absorbed by the boundary. This is done so that the forward and backward wavefronts generated do not collide and annihilate one another. The BCs are

$$Z(t < T_{BOUNDARY}, x = 0, y) = Z(t < T_{BOUNDARY}, x = x_{MAX}, y) = Z_s \tag{5.6}$$

$$Y(t < T_{BOUNDARY}, x = 0, y) = Y(t < T_{BOUNDARY}, x = x_{MAX}, y) = Y_s \tag{5.7}$$

with periodic BCs when $t > T_{BOUNDARY}$.

5.1.2 Spatially varied β

To investigate propagating waves in a spatially varied domain for the FHN model, the parameter β is linearly varied over y between 0.7 and 1.7 encompassing the oscillatory, excitable, subexcitable and nonexcitable domains. Our simulations used a linearly varying function of β but a different function could be have used. However at the cell scale, variation in β could be assumed to be linear due to the small scale. With a spatial domain of $x \in [0, x_{max}]$ and $y \in [0, y_{max}]$ the parameter β is given by

$$\beta(y) = \frac{y}{y_{max}} + 0.7. \tag{5.8}$$

When investigating a spatially varied domain for the Goldbeter model the parameter β is linearly varied over y between 0 and 1, i.e.

$$\beta(y) = \frac{y}{y_{max}}. \tag{5.9}$$

For simulations with spatially varied β the spatial domain is set to $x \in [0, 20], y \in [0, 80]$ so that β is varied over a large length y relative to the width x.

When the parameter β is spatially varied the ICs can have a qualitative effect on the resulting dynamics, so three different cases are considered. The first is homogeneous ICs, that is, where the initial values of the entire spatial domain are the same. For the FHN model these arbitrary initial values are chosen to be $u_0 = 1, v_0 = 1$, while for the Goldbeter model these initial values are chosen to be $Z_0 = 0.4, Y_s = 1.6$ (values taken from Goldbeter et al. (1990)).

The second set of ICs simulates an initial perturbation to the system. The initial values in a rectangular area in the centre of the domain are high, while the remainder of the domain has low initial values. In particular for the FHN model the initial values in the rectangular area are $u_0 = 2, v_0 = 2$ while in the remainder of the domain the initial values are $u_0 = 1, v_0 = 1$. When simulating the Goldbeter model the rectangular area has initial values $Z_0 = 1.4, Y_0 = 2.6$ and the remainder has $Z_0 = 0.4, Y_0 = 1.6$.

The third and final set of ICs are randomly generated initial values at each mesh point over the entire surface domain. This set of ICs is not particularly realistic but is used

to demostrate the possible dependence of the system on the ICs. For the FHN model the initial values are randomly generated in $[0, 2]$ and for the Goldbeter model the initial values are in $[0, 1.4]$.

5.2 FitzHugh-Nagumo model

The FHN model is a simple generic excitable model with known dynamics (Kneer et al., 2014); as such it is used as a sort of 'base case' before simulating the more relevant Ca^{2+} dynamics model by Goldbeter et al. (1990). The spatial, temporal and state variables of the model are all nondimensional. The behaviour of the FHN model simulated on a flat surface with spatially constant parameter β is described in Section 2.4.3. In the following subsection we simulate the model with the parameter β spatially varied over the surface. The parameters are set at $D = 0.12, \varepsilon = 0.36$, taken from Kneer et al. (2014).

5.2.1 Spatially varied β

In the following simulations β is linearly varied over the spatial domain with the three different ICs specified in Section 5.1.2.

First consider the homogeneous ICs in Figure 5.1. Recall that the system is oscillatory for $\beta < 1$ and stable for $\beta > 1$. Within the stable domain lies the excitable/subexcitable domain of $1 < \beta < 1.39$ in which waves are able to propagate. The supercritical Hopf bifurcation located where $\beta = 1$ (red dashed line) seperates the lower region where $\beta < 1$ (oscillatory) and the upper region where $\beta > 1$ (stable). Straight waves are continuously initiated in the oscillatory region ($\beta < 1$) and propagate upwards into the excitable region. The wave width and velocity decrease as β increases (corresponding to a decrease in excitability) and the waves break up as they reach the nonexcitable region.

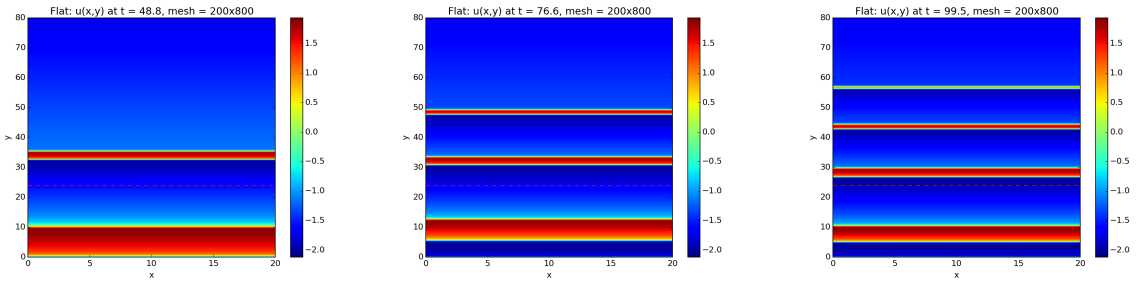

(a) $t = 48.8$ (b) $t = 76.6$ (c) $t = 99.5$

Figure 5.1: Wave propagation where the ICs are homogeneous and β is varied linearly over the surface according to (5.8), based on the FHN model. The Hopf bifurcation at $\beta = 1$ (red dashed line) seperates the oscillatory (lower) and excitable (upper) regions. Waves are generated in the oscillatory region and propagate upwards.

An initial perturbation to the system causes waves to form that are very slightly curved. However this is not enough to affect the dynamics (results not shown). When the ICs are randomly generated initial values at each mesh point the 'noise' produced is also not sufficient to alter the wave propagation in any significant way (results not shown). Hence in the FHN model for $D = 0.12$ the behaviour of the generated waves on a spatially varied surface have no significant dependence on the ICs.

5.3 Goldbeter model

The main interest of our research is on Ca^{2+} dynamics and wave propagation; as such we now apply the Goldbeter et al. (1990) Ca^{2+} model to a 2D spatial domain. We cannot use the FHN model to explain Ca^{2+} wave propagation as some biological excitable systems may behave in qualitatively different ways to classical excitable systems like the FHN model (Sneyd and Atri, 1993). The interaction of ions in the cell cytoplasm forms an inherently excitable system (Wilkins and Sneyd, 1998), but the structure of the Goldbeter model equations are quite different to the FHN model as the nullclines do not have the same shape (Kneer et al., 2014). As shown in Section 3.2 the Goldbeter model is excitable for a range of β near the left Hopf bifurcation (Figure 3.3) due to the shape of the nullclines (Figure 3.2). Like the FHN model there are oscillatory, excitable, subexcitable and nonexcitable regions and some critical wave size S^* seperating the excitable and subexcitable domains; however it has not been calculated for this model. The nondimensional equations for the Goldbeter model in a 2D spatial domain are as follows:

$$\frac{\partial Z}{\partial t} = 1 + v_1\beta - v_2 + v_3 + Y - kZ + D\Delta Z \tag{5.10}$$

$$\frac{\partial Y}{\partial t} = v_2 - v_3 - Y, \tag{5.11}$$

where Z is the cytosolic Ca^{2+} concentration, Y is the Ca^{2+} concentration in the internal stores, the algebraic variables and parameters are explained in Section 2.2.1 and the nondimensionalisation is explained in Section 3.1.2. Note that time is also nondimensional. The nondimensional spatial coordinates x, y are discretised as in Equations 5.1, 5.2 and the ODEs for each mesh point are

$$\frac{dZ_{i,j}}{dt} = 1 + v_1\beta - v_2 + v_3 + Y_{i,j} - kZ_{i,j} + D\Delta Z_{i,j} \tag{5.12}$$

$$\frac{dY_{i,j}}{dt} = v_2 - v_3 - Y_{i,j}, \tag{5.13}$$

with

$$v_2 = V_{M2}\frac{(Z_{i,j})^n}{K_2^n + (Z_{i,j})^n} \tag{5.14}$$

$$v_3 = V_{M3}\frac{(Y_{i,j})^m}{K_R^m + (Y_{i,j})^m}\frac{(Z_{i,j})^p}{K_A^p + (Z_{i,j})^p}, \tag{5.15}$$

where $Z_{i,j} := Z(x_i, y_j)$ and the Laplace operator Δ is specifed in Equation 5.5. The parameter β is the saturation function controlling the rate of inotisol trisphosphate (IP_3) induced Ca^{2+} release. β controls the stability and level of excitability of the system (note that this β is different from the parameter β of the FHN model).

The nondimensional diffusion coefficient D is set to 0.12 for the majority of the simulations as with the previous model, however this is not necessarily a physiologically accurate diffusion rate for Ca^{2+} in smooth muscle cells (SMCs) described by the model. There is some dependence of the solutions on the diffusion rate D: when D is larger the wave velocity will be greater and so the domain where waves are able to propagate is larger. Therefore when D is greater the region of excitability is slightly larger. There is an even larger dependence on D for the case where the parameter β is spatially varied, discussed in Section 5.3.2.

5.3.1 Spatially constant β

In this section we simulate the Goldbeter model on a flat surface with spatially constant β. We implement Dirichlet BCs on the upper and lower boundaries for $t < T_{BOUNDARY}$ so that the downwards travelling wave is absorbed, and an initial perturbation is simulated by a rectangular area with initial values $Z_s + 1, Y_s + 1$ corresponding to a supra-threshold excitation, and Z_s, Y_s everywhere else where Z_s, Y_s is the stable fixed point of the system.

When β is in the nonexcitable domain an initial perturbation will cause no wave propagation, when β is in the subexcitable domain an initial perturbation will generate a wave that shrinks in length until it disappears, and when β is in the excitable domain an initial perturbation will cause a wave to propagate outwards, see Figure 5.2. The wave width is smaller and the wave velocity is lower than that in the FHN model as the area in front of the wave takes longer to reach the excitation threshold. This is because the excitation threshold of the Goldbeter model is greater, a consquence of the shape of the nullclines. Thus the Goldbeter model is inherently less excitable than the FHN model.

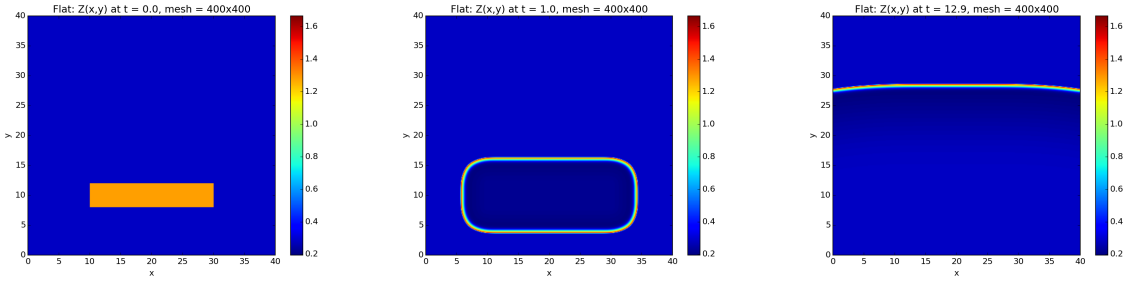

(a) $t = 0$ (b) $t = 1.0$ (c) $t = 12.9$

Figure 5.2: Propagation of a cytosolic Ca^{2+} wave with spatially constant $\beta = 0.25$ in the excitable domain. An initial perturbation generates a propagating wave that grows in length. Generated using the Goldbeter model.

When β in the excitable domain and a wave segment is broken with two open ends, rotating spirals will form from each end, see Figure 5.3. The same result can be achieved with the FHN model (results not shown).

Spiral waves are able to form from open wave ends as follows. After the formation of a broken wave, the wave can propagate in all directions except the waveback where the medium is temporarily nonexcitable, i.e. it can propagate forward and to the sides. This causes the wave to become slightly curved at the ends. The inability to propagate into the waveback causes the broken wave to eventually form spirals as seen in Figure 5.3. Spiral formation is further discussed in Section 2.4.2.

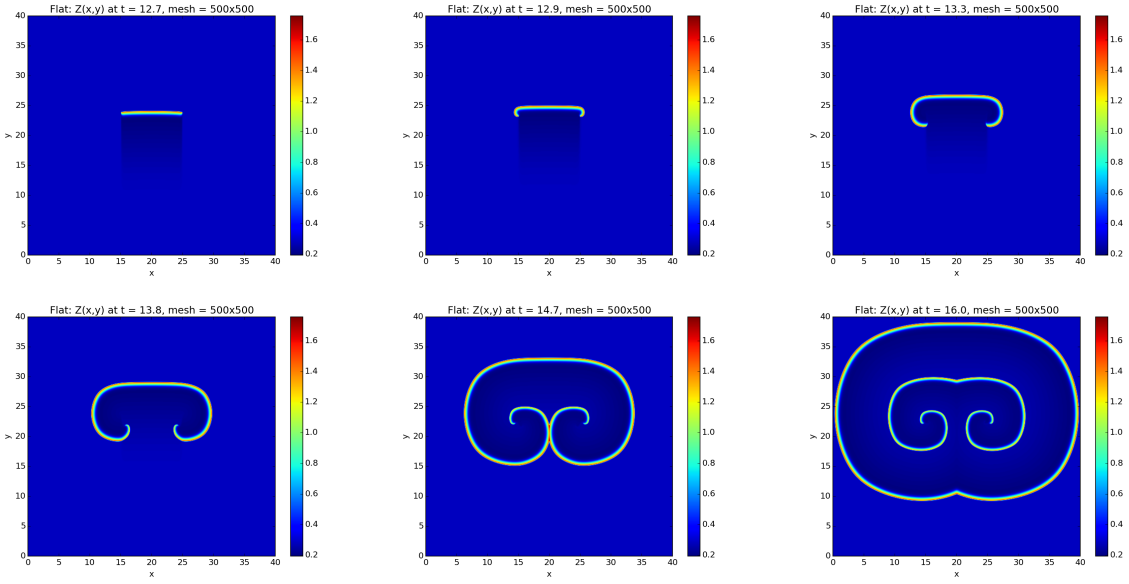

Figure 5.3: Spiral waves of cytosolic Ca^{2+} concentration forming from open wave ends with spatially constant $\beta = 0.25$ in the excitable domain. The wave is unable to propagate into the 'waveback' (dark blue region of low Ca^{2+} concentration) where the cells are temporarily nonexcitable, causing spiral shaped waves to form. Generated using the Goldbeter model.

5.3.2 Spatially varied β

As with the FHN model we consider β (and hence the level of excitability) spatially varied over a surface according to Equation 5.9. This includes the oscillatory, excitable, subexcitable, and two nonexcitable regions shown in Figure 3.3. The three sets of ICs used are detailed in Section 5.1.2.

Figure 5.4 presents the case with homogeneous ICs. The red dashed lines represent the two Hopf bifurcations in the system with the lower line seperating the excitable and oscillatory regions (refer to Figure 3.3). The waves are initiated in the oscillatory region with frequency according to Figure 3.5 (note that frequency is the inverse of period).

Near the lower Hopf bifurcation the frequency is low while near the upper bifurcation the frequency is high. Note that the oscillations of the Goldbeter model are a higher frequency than those in the FHN model (Kneer et al., 2014). The amplitude of the waves are dependent on β as per Figure 3.3; the amplitude is lowest near the upper bifurcation and highest near the lower bifurcation.

The straight waves propagate upwards towards the upper Hopf bifurcation but cease when they reach the nonexcitable region just past the bifurcation, as wave propagation is not possible when the medium is nonexcitable. The waves also propagate downwards towards the lower Hopf bifurcation and into the excitable domain. As they continue to propagate the wave width and velocity decrease as the excitability decreases, before disappearing at the lower nonexcitable domain where waves are unable to propagate (Figure 5.4a).

The high frequency of wave generation results in a high density of waves. When one wave reaches the (temporarily nonexcitable) waveback of a wave travelling in front, the wave behind will disappear. Consequently there will be a brief time period where there are no propagating waves in the excitable region and in the oscillatory region just above the lower Hopf bifurcation (Figure 5.4b). After this a large amplitude wave near the lower bifurcation is generated that travels in both directions, colliding with the wave above (Figure 5.4c). This continues for a short period of time before returning to the normal state and the cycle begins again.

Figure 5.5 shows the behaviour when the system has an initial perturbation to the system. The difference in initial values within the medium causes a curve in the nearby generated waves (Figure 5.5b). The high density of waves and the wave curvature from the initial perturbation results in some waves colliding with one another. This eventually causes waves to break and form open ends. If these open ends lie in the oscillatory or excitable regions then they will grow in length and curl. These open ends will form full spiral rotors as long as they do not collide with any other waves (Figure 5.5c).

When the ICs are randomly generated initial values at each mesh point we observe similar behaviour, shown in Figure 5.6. The 'noise' created causes uneven propagating waves (Figure 5.6b) that collide and break. The resulting asymmetric pattern (Figure 5.4c) is due to many open wave ends forming spiral waves that interact with one another, causing further open wave ends and hence more spirals.

There are multiple theories to explain the fascinating patterns generated by our models with the parameter β spatially varied. One possibility considered was Turing instability. While diffusion alone tends to create uniform stable states, when coupled with chemical reactions as in reaction-diffusion systems spatial patterns can appear (Biosa et al., 2006). Turing instability requires different nonzero diffusion rates for each state variable (Kapral,

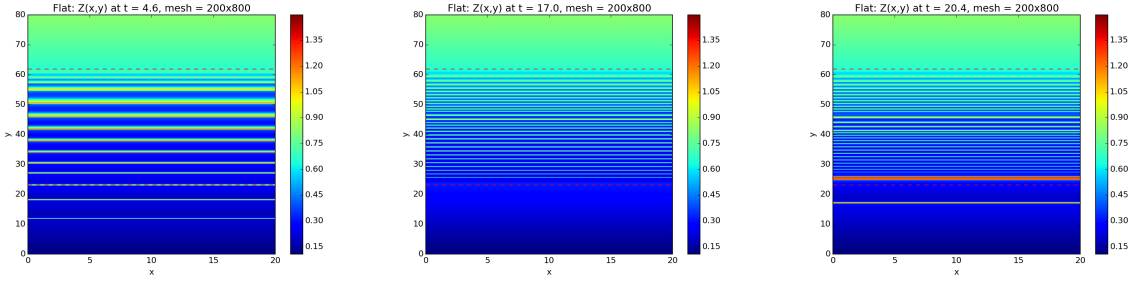

(a) $t = 4.6$ (b) $t = 17.0$ (c) $t = 20.4$

Figure 5.4: Cytosolic Ca^{2+} wave propagation with spatially varied β according to (5.9) and homogenenous ICs, based on the Goldbeter model. The red dashed lines denote the two Hopf bifurcations enclosing the oscillatory region. Waves are generated in the oscillatory region and propagate downwards into the excitable region.

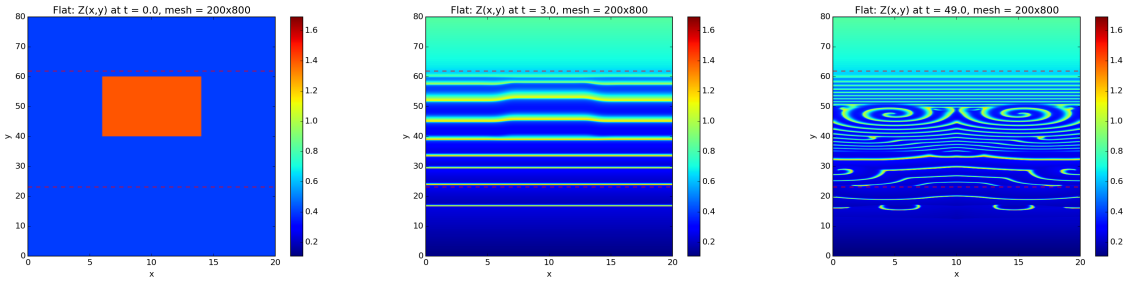

(a) $t = 0$ (b) $t = 3.0$ (c) $t = 49.0$

Figure 5.5: Cytosolic Ca^{2+} wave propagation with spatially varied β according to (5.9) and an initial perturbation to the centre of the domain, based on the Goldbeter model. The perturbation creates a curve in the generated waves which eventually collide with one another, producing open wave ends and then spiral waves.

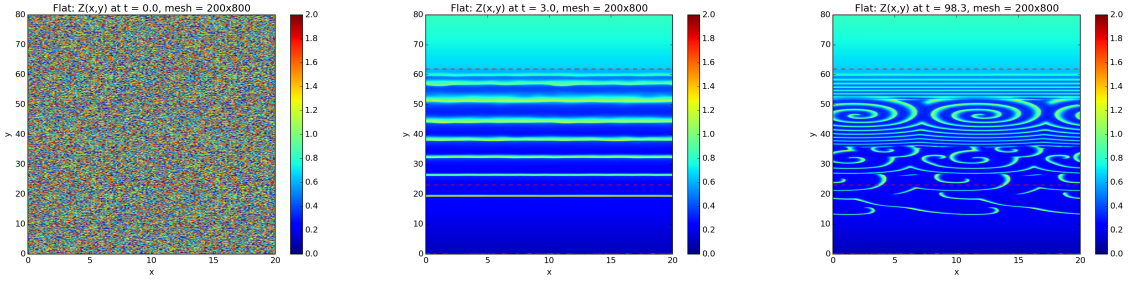

(a) $t = 0$ (b) $t = 3.0$ (c) $t = 98.3$

Figure 5.6: Cytosolic Ca^{2+} wave propagation with spatially varied β according to (5.9) and randomly generated initial values at each mesh point, based on the Goldbeter model. The ICs result in asymmetric waves that are not entirely straight causing them to eventually collide and spiral waves form.

1995), however both the FHN and Goldbeter models contain a zero diffusion coefficient. As such it is unlikely that either of these systems demostrate Turing instability.

An alternative possibility is that the dependence on ICs, particularly in the Goldbeter model, could indicate spatiotemporal chaos. This can occur when spiral waves collide with other wave fronts, causing new wave ends that form spirals and interact among each other (Sinha and Sridhar, 2014). The dynamics of individual elements is not chaotic and spatiotemporal chaos can only develop as a result of interactions between the elements.

Effect of Diffusion Coefficient D

For our main simulations using the Goldbeter et al. (1990) model the diffusion coeffcient D was set at 0.12, however other values were also tested (Figure 5.7). This diffusion coefficient determines the wave velocity in both the direction of propagation and perpendicular to propagation (the growth rate of open wave ends).

When $D = 0.05$ (Figure 5.7a) the behaviour when the ICs are randomly generated initial values is as follows. The 'noise' produced by the random ICs is dominant causing the waves generated to almost immediately collide and break. This produces many open wave ends that slowly grow and interact with other waves, however spiral rotors that continuously produce outwardly rotating spiral waves do not fully form as the growth rate of the open ends is too low (as a result of the low diffusion).

When $D = 0.12$ (Figure 5.7b) the diffusion rate is low enough to cause the waves to collide and break, but high enough that the open wave ends grow fast enough to fully form spiral rotors.

When $D = 0.25$ (Figure 5.7c) then the high wave velocity due to high diffusion rate is dominant causing the waves to quickly smooth out so the resulting pattern is similar to the case with homogeneous ICs in Figure 5.4.

Note that this behaviour is also true for the FHN model. The value of $D = 0.12$ is too high for any spirals to form in our previous simulations but when D is lowered we obtain open wave ends curling and spirals are able to form (results not shown). The the behaviour of propagating waves on a spatially varied surface becomes less regular as D decreases, however when $D = 0$ then no waves can propagate. Therefore there must be some point for $D << 1$ where this change occurs (not yet determined).

The mesh size also has an effect on our results. A smaller mesh has a similar effect to lowering the diffusion coefficient, and vice versa for a larger mesh (results not shown). This mesh dependency is an issue discussed further in Section 7.1.3.

5.4 Summary

In conclusion, an initial perturbation (in the form of a localised input of Ca^{2+} when simulating the Goldbeter et al. (1990) model) will form a propagating wave when the spatial

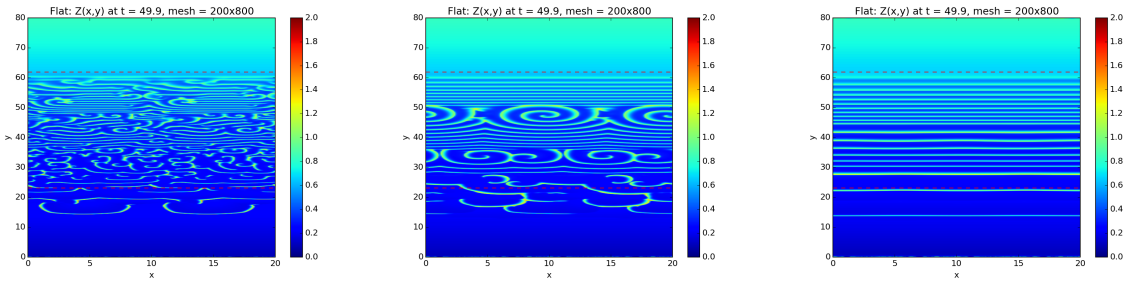

(a) $D = 0.05$ (b) $D = 0.12$ (c) $D = 0.25$

Figure 5.7: The Goldbeter model simulated on a flat surface with spatially varied β and random ICs for different diffusion coefficients D. The spatial behaviour is more regular for higher values of D while the behaviour is less regular and prone to what seems like spatiotemporal chaos when D is low. Spiral rotors form when D is in some mid range of D.

medium is excitable (determined by the parameter β), a propagating wave that shrinks in length when the medium is subexcitable, and no propagating wave when the medium is nonexcitable. In addition when a spatial medium is excitable and a propagating wave is broken the open end will curl and is able to form a spiral rotor, generating outwardly rotating spiral waves.

The excitability of a system can be varied over a surface via the parameter β of the FHN or Goldbeter model which determines whether the system is oscillatory, excitable, subexcitable or nonexcitable. Waves will be generated where the system is oscillatory. If the ICs are homogeneous then the generated waves will be straight and when they collide will leave no open ends. If the ICs are inhomogeneous then the offset in the waves caused by the ICs will make the waves curved and may eventually cause them to collide and form open wave ends. These ends will grow in length if the system is oscillatory or excitable, leading to curled wave ends and possibly spatiotemporal chaos from the interaction of the open wave ends. Spiral rotors will form if the difffusion coeffcient is neither too low (the growth rate of an open end will be too low) nor too high (waves will travel fast and collide before a spiral can form).

Chapter 6

Geometry

In this chapter we introduce the concept of spatial curvature to our 2D spatial domain simulations using the FitzHugh-Nagumo (FHN) and Goldbeter models. To do so we simulate our models on a torus, a surface with both negative and positive Gaussian curvature. A torus was also chosen as it can be mapped to a global isothermal coordinate system, meaning that it can be mathematically interpreted as a flat surface with spatially dependent diffusion. Global isothermal coordinates are more difficult to find for other types of surfaces.

Spatial curvature is especially relevant to our work on calcium (Ca^{2+}) wave propagation in smooth muscle cells (SMCs) as arteries and arterioles are curved structures, and in particular the cerebral cortex of the brain is a strongly curved structure. The pathology cortical spreading depression (CSD) associated with functional hyperaemia occurs in the cerebral cortex, where functional hyperaemia is controlled by neurovascular coupling involving the intercellular communication between SMCs and other cells in the brain tissue.

Our analysis is initially based off of the work of Kneer et al. (2014) who simulated the FHN model on a torus and found that positive and negative Gaussian curvature have opposite effects on the effective diffusion rate, resulting in new wave solutions such as stable propagating wave segments as discussed in Section 2.5.2.

6.1 Method

The computation of a model on a torus is identical to on a flat surface in the previous chapter, with the exception of the spatial coordinates and Laplace operator. See Section 5.1 for full details on the method of computation. The Laplace-Beltrami operator in torus coordinates (θ, φ) is

$$\Delta_{LB} = -\frac{\sin\theta}{r(R + r\cos\theta)}\frac{\partial}{\partial\theta} + \frac{1}{r^2}\frac{\partial^2}{\partial\theta^2} + \frac{1}{(R + r\cos\theta)^2} + \frac{\partial^2}{\partial\varphi^2}. \tag{6.1}$$

where R and r are the major and minor curvature radii respectively. The spatial coordinates are discretised as follows:

$$\theta_i = \theta_0 + i\delta\theta,\ i = 0, 1, \ldots, I \tag{6.2}$$

$$\varphi_j = \varphi_0 + j\delta\varphi,\ j = 0, 1, \ldots, J \tag{6.3}$$

so that the Laplace-Beltrami operator is calculated using the following derivative approximations:

$$\frac{\partial u}{\partial \theta} \approx \frac{u_{i+1,j} - u_{i-1,j}}{2\delta\theta} \tag{6.4}$$

$$\frac{\partial^2 u}{\partial \theta^2} \approx \frac{u_{i+1,j} - 2u_{i,j} + u_{i-1,j}}{\delta\theta^2} \tag{6.5}$$

$$\frac{\partial^2 u}{\partial \varphi^2} \approx \frac{u_{i,j+1} - 2u_{i,j} + u_{i,j-1}}{\delta\varphi^2} \tag{6.6}$$

for a function $u_{i,j} := u(\theta_i, \varphi_j)$. In our simulations we use $r = 20/2\pi$ so that the minor circumference is 20, with $R = 80/2\pi$ and $R = 40/2\pi$ for weakly and strongly curved torii, respectively. The boundary conditions (BCs) are periodic for both θ and φ. The diffusion coefficient is set to $D = 0.12$.

The 2D plots of the (θ, φ) spatial domain are produced in Python while the solutions on a 3D torus are produced using the Visualisation Toolkit (VTK) (Schroeder et al., 2006) and visualised in Paraview (Ahrens et al., 2005). The source code can be found at www.github.com/BlueFern/CRDModel. All generated videos corresponding to the figures in this chapter can be found at the UC High Performance Computing YouTube channel at http://bit.ly/1LOPTDM.

6.1.1 Spatially constant β

To investigate propagating waves on a torus using the Goldbeter model where the surface is spatially constant (i.e. when the parameter β is constant) an initial perturbation to the system is simulated by setting the values of the initial conditions (ICs) higher in a small rectangular area of (θ, φ) (specifically $Z_s + 1, Y_s + 1$ corresponding to a supra-threshold excitation) than on the rest of the domain (set to Z_s, Y_s, the stable fixed point (FP) of the system). This perturbation will cause a wave to propagate throughout the surface of the torus if the system is excitable.

The θ boundary is periodic. There are additional Dirichlet BCs at the lower and upper φ boundaries for time $t < T_{BOUNDARY}$, where $T_{BOUNDARY}$ is large enough so that a backward travelling wavefront generated by an initial perturbation is absorbed by the boundary. This is done so that the forward and backward wavefronts generated do not collide and annihilate one another. The BCs are

$$Z(t < T_{BOUNDARY}, \theta = 0, \varphi) = Z(t < T_{BOUNDARY}, \theta = x_{MAX}, \varphi) = Z_s \tag{6.7}$$

$$Y(t < T_{BOUNDARY}, \theta = 0, \varphi) = Y(t < T_{BOUNDARY}, \theta = x_{MAX}, \varphi) = Y_s \tag{6.8}$$

with periodic BCs when $t > T_{BOUNDARY}$.

6.1.2 Spatially varied β

To investigate propagating waves on a torus with the domain spatially varied using the FHN model, the parameter β is linearly varied over φ between 0.7 and 1.7 encompassing the oscillatory, excitable, subexcitable and nonexcitable domains. Our simulations used a linearly varying function of β but a different function could be used. However at the cell scale, variation in β could be assumed to be linear due to the small scale. With a spatial domain of $\theta \in [0, 2\pi]$ and $\varphi \in [0, 2\pi]$ the parameter β is given by

$$\beta(\varphi) = \frac{\varphi}{2\pi} + 0.7. \tag{6.9}$$

When investigating a spatially varied domain for the Goldbeter model the parameter β is linearly varied over φ between 0 and 1, i.e.

$$\beta(\varphi) = \frac{\varphi}{2\pi}. \tag{6.10}$$

When the parameter β is spatially varied the ICs can have a qualitative effect on the resulting dynamics, so three different cases are considered. The first is homogeneous ICs where the initial values of the entire domain are the same. For the FHN model these are $u_0 = 1, v_0 = 1$, and for the Goldbeter model these are $Z_0 = 0.4, Y_s = 1.6$ (values taken from Goldbeter et al. (1990)).

The second set of ICs simulates an initial perturbation to the system. The initial values in a rectangular area in the centre of the (θ, φ) domain are high, while the remainder of the domain has low initial values. When simulating the FHN model the initial values in the rectangular area are $u_0 = 2, v_0 = 2$ while in the remainder of the domain the initial values are $u_0 = 1, v_0 = 1$. When simulating the Goldbeter model the rectangular area has initial values $Z_0 = 1.4, Y_0 = 2.6$ and the remainder of the domain has $Z_0 = 0.4, Y_0 = 1.6$.

The third set of ICs are randomly generated initial values at each mesh point over the entire surface domain. For the FHN model the initial values are randomly generated in $[0, 2]$ and for the Goldbeter model the initial values are in $[0, 1.4]$. These three sets of ICs are described further in Section 5.1.2.

6.2 Effect on Diffusion

To visualise the effect of spatial curvature on diffusion itself we solve the basic heat equation (a.k.a the diffusion equation) $\frac{\partial u}{\partial t} = D\Delta u$ on a torus. Figure 6.1 shows the heat equation on the (θ, φ) spatial domain with diffusion coefficient $D = 0.12$. The rate of diffusion is greatest on the inside of the torus ($\theta = \pi$) and weakest on the outside of the torus ($\pi = 0$).

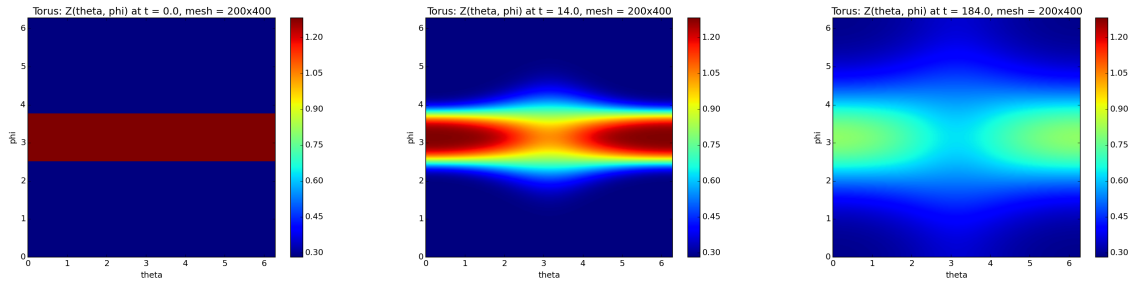

(a) $t = 0$ (b) $t = 14.0$ (c) $t = 184.0$

Figure 6.1: Diffusion on a strongly curved torus with $r = 20/2\pi$, $R = 40/2\pi$, $D = 0.12$ visualised on the (θ, φ) spatial domain. Diffusion is greatest at $\theta = \pi$ on the inside of the torus.

The difference in the rate of diffusion can be explained by a transformation in coordinate system to the so called toroidal coordinates $(\tilde{\theta}, \tilde{\varphi})$ (discussed in Section 2.5.1), a global isothermal orthgonal coordinate system.

The Laplace-Beltrami operator in toroidal coordinates is

$$\Delta_{LB} = \frac{(\cosh \eta - \cos \tilde{\theta})^2}{a^2} \left(\frac{\partial^2}{\partial \tilde{\theta}^2} + \frac{\partial^2}{\partial \tilde{\varphi}^2} \right) \tag{6.11}$$

where a and η are given by equations 2.31, 2.32 respectively. Therefore the implicit spatial dependence of diffusion on curvature can be expressed explicitly by this function $C(\theta) = (\cosh \eta - \cos \tilde{\theta})^2 / a^2$ (where $\tilde{\theta}$ is a function of θ according to equation 2.33), so that diffusion can be expressed as $DC(\theta)$ where the parameter D is the diffusion strength.

The Gaussian curvature $G(\theta)$ given in equation 2.21 is positive on the outside of the torus ($\theta = 0$) and negative on the inside of the torus ($\theta = \pi$), see Figure 2.5. The coupling strength $C(\theta)$ is lowest on the outside of the torus and strictly increasing to the inside of the torus. A more strongly curved torus (in this case whre $R = 40/2\pi$) has a larger gradient of $C(\theta)$, meaning it has higher coupling strength at the torus inside and slightly lower coupling strength at the torus outside than a weakly curved torus ($R = 80/2\pi$).

Therefore when the Gaussian curvature is strongly negative the coupling strength is high, when the curvature is strongly positive the coupling strength is low, and when there is no curvature the coupling strength is equal to one. This means diffusion is greater in areas of more negative curvature and weaker in areas of more positive curvature.

6.3 FitzHugh-Nagumo model

In this section we apply the FHN excitable model to the surface of a torus and investigate the effect of the surface curvature on wave formation and propagation. This model is detailed in Section 2.4.3. The spatial, temporal and state variables of the model are all nondimensional. The results for constant β are explained in Section 2.5.2 and originally found by Kneer et al. (2014). There exists an additional wave solution on a torus, namely

a stable propagating wave segment not found when the model is simulated on a flat surface with no spatial curvature.

6.3.1 Spatially varied β

Here we consider the FHN model on the surface of a torus with the parameter β controlling the excitability varied linearly over the spatial domain.

When using homogeneous ICs the generated waves are curved outwards (convex) due to the higher rate of diffusion on the torus inside (and hence greater wave velocity), but aside from the wave curvature there is little difference from the case on a flat medium in Figure 5.1. The remaining two sets of ICs produce similar results.

As with a flat surface, when D is low enough (less than 0.05) then spirals and/or complex patterns will form. In particular they will form even from homogeneous ICs as the spatial variation in diffusion causes the waves to travel at different velocities in different areas of the torus, creating curved waves which eventually collide and form open wave ends when the wave velocity is low (results not shown).

6.4 Goldbeter model

In this section we apply the Goldbeter Ca^{2+} model to a torus and compare the results to both the FHN model simulated on a torus in the previous section and the Goldbeter model on a flat medium in Section 5.3. This model is detailed in Section 2.2.1.

6.4.1 Spatially constant β

When β is spatially constant over the surface of the torus the solutions found on a flat surface with periodic BCs in Section 5.3 also exist on a torus. In particular a ring wave when β is excitable, a propagating wave that shrinks in length when β is subexcitable, and no wave propagation when β is nonexcitable. In addition there exists a stable propagating wave segment solution with constant wave size and shape on the inside of the torus for a range of β in the subexcitable domain, shown in Figure 6.2. A wave centred on the inside of the torus has higher diffusion rate $DC(\theta)$ at the centre ($\theta = 0$) than at its ends, causing enhanced growth of the wave ends as it propagates in the φ-direction. At the same time, when β is in the subexcitable parameter regime then a perturbation will shrink in length. Therefore this stable wave segment solution exists because of the balance between the subexcitable nature of the medium (from β in the subexcitable domain) causing the wave to shrink in length, and the growth induced by the gradient in diffusion rate over the length of the wave segment. See Section 2.5.2 for further details.

The propagating wave is much thinner than those found in the FHN model because of the high excitation threshold and hence relatively low excitability of the Goldbeter

model.

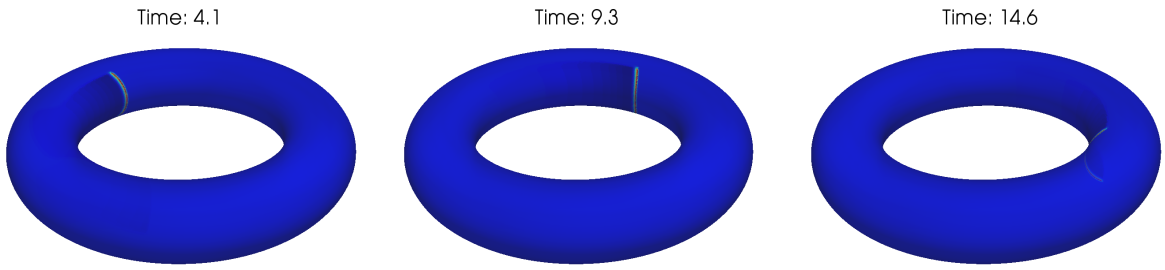

Figure 6.2: Propagation of a stable cytosolic Ca^{2+} wave segment on the inside of a torus with $R = 80/2\pi$, spatially constant $\beta = 0.14$ in the subexcitable domain and $D = 0.12$. Generated using the Goldbeter model. The stable wave segment is a new solution not found on a flat surface.

In the FHN model the stable wave segment solutions are only found on the outside of the torus for β in the excitable domain and for the Goldbeter model the stable wave segments are only on the inside of the torus for β in the subexcitable domain. It is unclear why these models differ in this respect. There may exist unstable solutions (such in the FHN model found by Kneer et al. (2014)) on the outside of the torus but these have not been found for this model.

6.4.2 Spatially varied β

Consider the Goldbeter model with the parameter β varied linearly over the surface of the torus with both homogeneous and inhomogeneous ICs. Figure 6.3 visualises the simulation with homogeneous ICs on the (θ, φ) spatial domain and on the surface of a weakly curved torus ($R = 80/2\pi$). As in Section 5.3 the waves are generated in the oscillatory domain between the two Hopf bifurcations (red dashed lines).

The generated waves are curved as they travel faster in areas of high diffusion rate, specifically the torus inside ($\theta = \pi$). The waves are generated with high frequency and eventually the curvature of the waves causes them to collide and break, forming open wave ends. If these ends lie in the oscillatory or excitable regions of the surface then they will grow in length and curl. However the weak surface curvature of the torus is not enough to perturb the waves sufficiently and as a result there are almost no curled wave ends that form.

The case with homogeneous ICs on a more strongly curved torus ($R = 40/2\pi$) is shown in Figure 6.4. The curvature of the waves is much more pronounced than on the weakly curved torus in Figure 6.3, as there is a higher gradient of coupling strength from the torus outside ($\theta = 0$) to inside ($\theta = \pi$) on the strongly curved torus and hence a greater difference in diffusion rate over the surface. Since the waves are strongly curved

they collide faster and form many more open wave ends and curls compared to on the weakly curved torus.

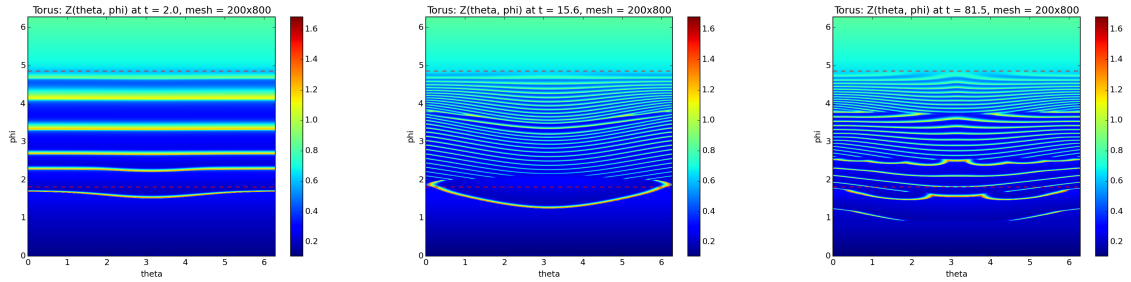

(a) (θ, φ) spatial domain.

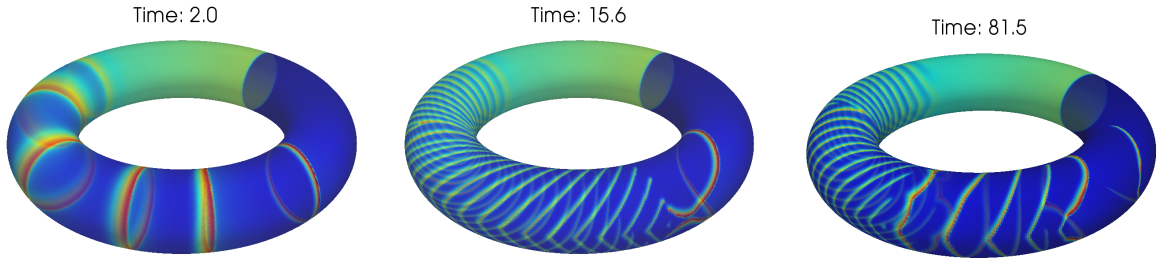

(b) Torus.

Figure 6.3: Cytosolic Ca^{2+} wave propagation on a weakly curved torus with $R = 80/2\pi$, $D = 0.12$, β spatially varied according to (6.10) and with homogeneous ICs. Generated using the Goldbeter model. The weak spatial curvature produces curved waves that ocassionally collide but are mostly regular.

When the ICs are inhomogeneous with an initial perturbation in the centre of the spatial domain on both a weakly curved (Figure 6.5a) and strongly curved (Figure 6.5b) torus, there is no significant difference from homogeneous ICs as the effect of the surface curvature is dominant. Howvever the offset in the generated waves produced by the initial perturbation on the weakly curved torus will have a slight effect on the system so that there are a small number of open ends curling, but no spiral rotors form. Figure 6.6a shows a weakly curved torus with random ICs instead. In this case the ICs perturb the system enough so that the resulting pattern is asymmetric and multiple spiral rotors have fully formed in the oscillatory region of the torus. A strongly curved torus with random ICs is shown in Figure 6.6b. The pattern is again asymmetric but the overall behaviour is similar to the cases with other ICs as the strong surface curvature has the dominant effect.

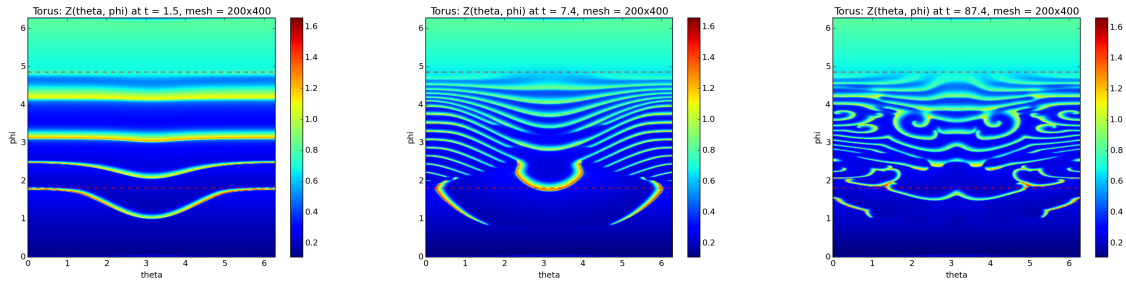

(a) (θ, φ) spatial domain.

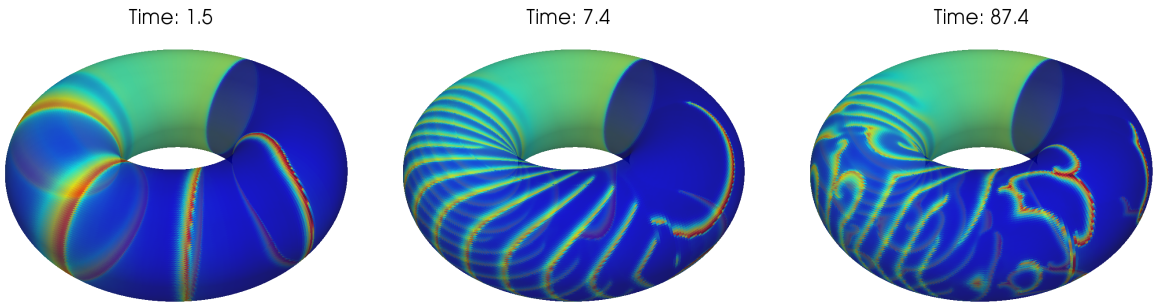

(b) Torus.

Figure 6.4: Cytosolic Ca^{2+} wave propagation on a strongly curved torus with $R = 40/2\pi$, $D = 0.12$, β spatially varied according to (6.10) and with homogeneous ICs. Generated using the Goldbeter model. The strong spatial curvature produces strongly curved waves which collide and produce open wave ends that curl and can form spirals.

6.5 Summary

In conclusion, surface curvature can cause areas of different diffusion rates and hence areas of different wave velocity. When β is constant, initial perturbations are more inclined to grow in the areas of negative curvature (higher diffusion) and more inclined to shrink in areas of positive curvature (lower diffusion). This produces a new solution of the spatial Goldbeter model in the form of a propagating wave segment on the inside of the torus for subexcitable β. This solution is not found in the FHN model; consequently the generic FHN model should not be used to describe the dynamics of SMC Ca^{2+} wave formation and propagation.

When β is linearly varied, the spatial variation in diffusion causes curved waves to form and collide forming open wave ends if the diffusion rate is low enough and the surface curvature great enough, with any ICs. This is in contrast to a flat surface where inhomogeneous ICs are required to obtain any open wave ends when β is linearly varied over the surface. These open ends will grow and curl if they lie in either the oscillatory or excitable regions of the surface. Spiral rotors will form if a wave is able to fully curl before colliding with another wave. This is possible if the surface is large enough and the diffusion is neither too low (the growth rate of an open wave end will be too low)

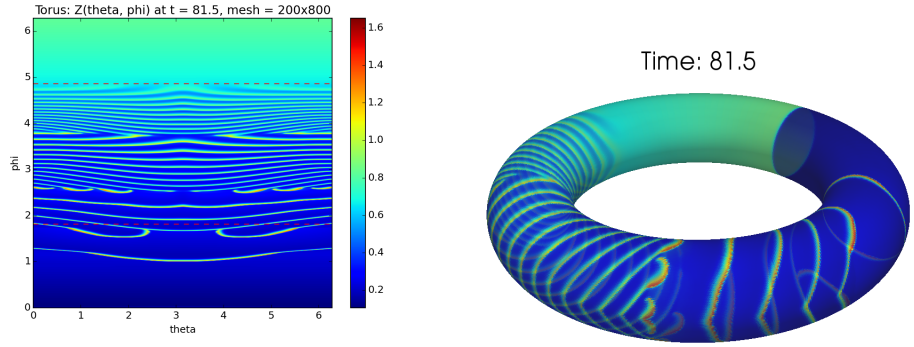

(a) Weakly curved torus, $R = 80/2\pi$.

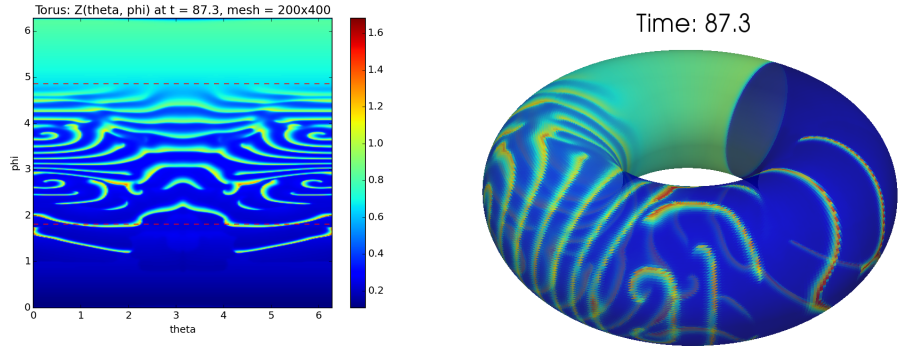

(b) Strongly curved torus, $R = 40/2\pi$.

Figure 6.5: Cytosolic Ca^{2+} wave propagation with β spatially varied according to (6.10) and an initial perturbation in the centre of the domain with $D = 0.12$. Generated using the Goldbeter model. The initial perturbation will create a curve in the generated waves (see Figure 5.5b) but will not be enough to induce any significant difference in behaviour from the case with homogeneous ICs in Figures 6.3, 6.4.

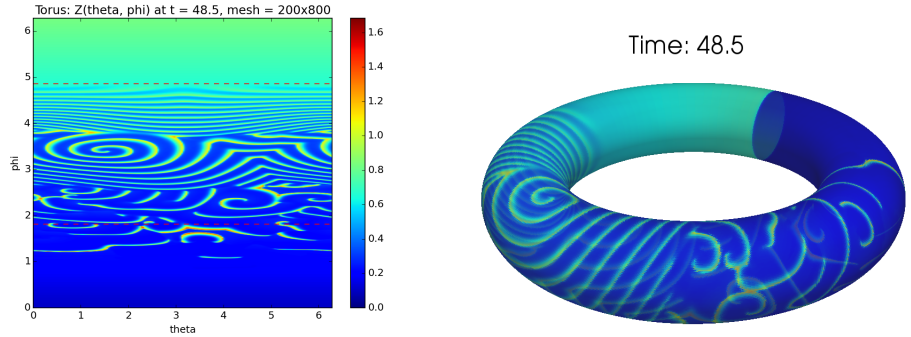

(a) Weakly curved torus, $R = 80/2\pi$.

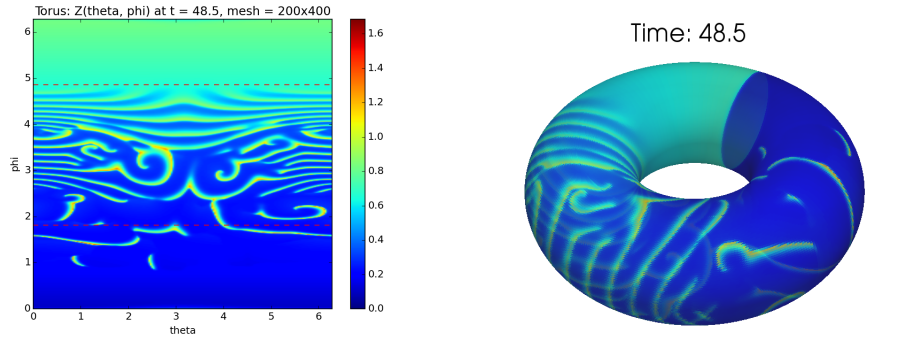

(b) Strongly curved torus, $R = 40/2\pi$.

Figure 6.6: Cytosolic Ca^{2+} wave propagation with β spatially varied according to (6.10) and randomly generated initial values at each mesh point with $D = 0.12$. Generated using the Goldbeter model. The strongly inhomogeneous ICs perturb the system enough so that the waves generated are irregularly shaped (see Figure 5.6b) and consequently will collide and form open wave ends leading to spiral rotors and asymmetric wave patterns regardless of the spatial curvature.

nor too high (waves collide before spirals can form). The waves will quickly collide and form open wave ends when the waves are more strongly curved. This will occur when the surface curvature is strongly curved or the ICs are inhomogeneous.

As with a flat surface, increasing the diffusion coefficient from $D = 0.12$ will increase the wave velocity and the generated waves will be more regular. Decreasing the diffusion coefficient will decrease the wave velocity and any inhomogeneous ICs will have the dominant effect causing the generated waves to be less regular and more seemingly 'chaotic'.

Chapter 7

Conclusions

7.1 Discussion

In this thesis the dynamics of calcium (Ca^{2+}) within a single and coupled smooth muscle cell (SMC)system and the propagation of intercellular Ca^{2+} waves were studied. The first was achieved using the minimal model by Goldbeter et al. (1990) based on Ca^{2+} induced Ca^{2+} release (CICR). By varying a single parameter of the model, qualitatively different dynamics (stable or oscillatory) were produced. Two other minimal models by Gonzalez-Fernandez and Ermentrout (1994) and Meyer and Stryer (1988) based on different mechanisms in the cell were also briefly studied and compared.

The dynamics of these minimal models were then compared to the complex and more realistic model based on the work of Farr and David (2011) and Dormanns et al. (2015) of a SMC and endothelial cell (EC) 'unit', the model of which includes the influence of neuronal activity on the Ca^{2+} dynamics via the process of neurovascular coupling (NVC).

The models were then extended to two adjacent coupled SMCs (or coupled SMC/EC units) via a linear coupling term, where the cells/units have different parameter values and with variable rate of diffusion of Ca^{2+} between the two.

The formation and propagation of Ca^{2+} waves was simulated in a two dimensional (2D) spatial domain using the minimal model by Goldbeter et al. (1990), where the domain was either constant or spatially varying in its local dynamics (oscillatory, excitable, subexcitable or nonexcitable). This was compared to the generic excitable FitzHugh-Nagumo (FHN) model (FitzHugh, 1961; Nagumo et al., 1962) with known spatial dynamics (Kneer et al., 2014).

Finally the concept of spatial curvature was introduced to the 2D spatial domain via simulations on a toroidal surface containing both negative and positive Gaussian curvature. Both the Goldbeter et al. (1990) and FHN models were simulated on a torus to study the effects of spatial curvature on the dynamics of Ca^{2+} waves in SMCs.

7.1.1 Non Spatial Models

The bifurcation structure of the SMC cytosolic Ca^{2+} concentration in each of the four models are of a similar form even though each model has a different bifurcation parameter varied. Excluding the Gonzalez-Fernandez and Ermentrout (1994) model the different parameters all serve a similar function, that is, raising the inotisol trisphosphate (IP_3) induced Ca^{2+} flux from the internal stores (sarcoplasmic reticulum (SR) or endoplasmic reticulum (ER)) into the cytosol of the cell. When these parameters are either low or high the system tends to a steady state (stable), otherwise the system variables oscillate. Within the stable domain lies the excitable subdomain adjacent to the oscillatory domain. Therefore a single cell or SMC/EC unit will be either nonexcitable, excitable or oscillatory.

In particular the bifurcation structure of the Goldbeter et al. (1990) model is the most comparable to that of the more complex SMC/EC model. The oscillatory domain of both models are enclosed by Hopf bifurcations and there is a steep increase in both the amplitude and period of oscillations directly after the lower Hopf bifurcation. There also exists an excitable domain below the lower Hopf bifurcation in both models. The Goldbeter model is only two dimensional and yet the dynamics produced in a SMC are very similar the dynamics of the 14 dimensional SMC/EC model. The only additional components present in the SMC/EC model are the small amplitude oscillations and bistability when J_{PLC} is low and neuronal activity high, believed to exist due to the stretch activated Ca^{2+} channels not included in the minimal Goldbeter model.

The dynamics of a system of two coupled cells or SMC/EC units are seemingly independent of the model implemented, dependent only on their dynamics when uncoupled (either excitable, nonexcitable or oscillatory). The behaviour of two coupled cells/units when strongly coupled is determined by where the average of their two parameters lie in the parameter space. For example using the Goldbeter et al. (1990) model, two coupled cells with $\beta_1 = 0.5$ and $\beta_2 = 0.6$ will both behave like a cell with $\beta = 0.55$ (behaviour determined by the bifurcation diagram in Figure 3.3).

Identical coupled cells/units will remain the same. Two nonidentical nonexcitable cells/units will remain nonexcitable and two nonidentical excitable cells/units will remain excitable when coupled. Two nonidentical oscillatory cells/units will oscillate with variable amplitude when weakly coupled and when strongly coupled they synchronise by oscillating at the same frequency.

A coupled nonexcitable and excitable cell/unit will remain stable. A coupled nonexcitable and oscillatory cell/unit will both oscillate when weakly coupled and either be stable or oscillatory when strongly coupled depending on their average J_{PLC}. A coupled excitable and oscillatory cell/unit will cause the excitable one to oscillate with small amplitude when weakly coupled. When the coupling strength reaches some threshold value the excitable cell/unit experiences a large amplitude oscillation when the coupling

strength (and hence the intercellular Ca^{2+} flux) is enough to cause the SMC Ca^{2+} concentration of the excitable cell/unit to exceed the excitation threshold; as the coupling strength increases the cells/units exhibit variable amplitude oscillations, and finally synchronisation when strongly coupled.

Therefore when weakly coupled it appears the movement of ions between two cells can produce new complex behaviour fundamentally different from what one would predict looking at either cell in isolation, in particular two coupled oscillatory cells or an excitable coupled with an oscillatory cell.

While these models have similar bifurcation structure for a single cell/unit and similar behaviour for two coupled cells, it must be noted that their respective spatial models of many cells or units simulated on some surface may have qualitatively different behaviour to one another.

7.1.2 Spatial Models

The formation and propagation of waves in a flat spatial medium with spatially constant local dynamics is dependent on the nature of those dynamics, specifically whether the medium is oscillatory, excitable, subexcitable or nonexcitable (determined by the parameter β of the Goldbeter et al. (1990) model). An initial perturbation in the form of a localised input of Ca^{2+} will form a propagating wave when the spatial medium is excitable and a propagating wave that shrinks in length when the medium is subexcitable. When a propagating wave is broken and the medium is excitable then the open wave end will curl and is able to form a spiral rotor, generating outwardly rotating spiral waves.

The local dynamics of a system can be varied over a surface via the parameter β as a linear function of the spatial coordinate y. Waves will be generated where the system is oscillatory and propagate into the excitable domain. If the initial conditions (ICs) are homogeneous then the generated waves will be straight and when they collide will leave no open ends. If the ICs are inhomogeneous then the offset in the waves caused by the ICs will make the waves curved and may eventually cause them to collide and form open wave ends. These ends will grow in length if the system is oscillatory or excitable, leading to curled wave ends and possibly spatiotemporal chaos from the interaction of the open wave ends. Spiral rotors will form if a wave is able to fully curl before colliding with another wave. This is possible if the surface is large enough and the diffusion is neither too low (the growth rate of an open wave end will be too low) nor too high (waves collide before spirals can form).

Including the concept of spatial curvature via a toroidal surface can produce areas of different diffusion rates (low diffusion when the surface has positive curvature and high diffusion for areas of negative curvature), and hence areas of different wave velocity. When the local dynamics are spatially constant (via the parameter β), initial perturbations are

more inclined to grow on the torus inside (negative curvature and thus higher diffusion) and more inclined to shrink on the torus outside (positive curvature and thus lower diffusion). This produces a new solution of the spatial Goldbeter model in the form of a propagating wave segment with stable wavesize on the inside of the torus when the medium is subexcitable. This solution is not found when the FHN model is simulated on a torus; consequently the dynamics of the generic FHN model should not be used to describe the dynamics of SMC Ca^{2+} wave formation and propagation.

When the local dynamics are varied over the toroidal surface via the parameter β as a linear function of the spatial coordinate φ, the spatial variation in diffusion causes outwardly curved waves to form as the waves travel faster on the torus inside. When the waves are strongly curved they will collide and interact, forming open wave ends. This will occur when the surface curvature is strongly curved and/or the ICs are inhomogeneous. This is in contrast to a flat surface where inhomogeneous ICs are required to obtain any significant wave interaction.

Therefore wave interaction (causing complex wave patterns such as spiral waves and possibly spatiotemporal chaos) on a spatially varied domain will occur if the diffusion rate is low enough, and either the spatial domain is strongly curved or the ICs are inhomogeneous.

Low coupling strength in the coupled cell models of Chapters 3, 4 lead to complex behaviour such as variable amplitude oscillations. Low diffusion rate in the spatial models of Chapters 5, 6 lead to low wave velocity causing irregular propagating waves with ample wave interaction. High coupling strength in the coupled cell models caused synchronisation between the two cells. High diffusion rate lead to high wave velocity causing regular propagating waves with little to no wave interaction. In both cases the 'interesting' behaviour was found when the coupling/diffusion strength was low.

7.1.3 Limitations and Future Work

A limitation of our work is the use of a simple linear coupling term corresponding to Fick's Law, i.e. the Ca^{2+} moves from high to low concentration. A more complex coupling mechanism such the Goldman Hodgkin Katz (GHK) equation for the movement of ions and membrane potential may be used. This describes the ionic flux carried by an ionic species across a cell membrane as a function of the membrane potential (as ions are electrically charged) in addition to the concentrations of the ion inside and outside of the cell. An example of this coupling mechanism is used by Kapela et al (Kapela et al., 2009) to model the flow of ions (specifically Ca^{2+}, K^{+}, Na^{+} and Cl^{-}) between two cells. A similar coupling expression could be applied to examine whether a more accurate and complex coupling term would affect the underlying dynamics of the system.

Our simulations on a flat and curved surface in Chapters 5, 6 were computed on

a relatively small mesh (200×800) in order to have a feasible runtime on our local computer. However increasing or decreasing this mesh size resulted in a qualitative change in behaviour; decreasing the mesh to 100×400 caused the same effect as decreasing the diffusion coefficient and increasing the mesh to 300×1200 was similar to increasing the diffusion coeffcient. This is known as mesh dependency, a problem well known in areas such as compuational fluid dynamics. Future work may involve increasing the mesh until the solution converges and there is no further dependence on the mesh size. These large mesh simulations will most likely require parallel architecture to run with a feasible runtime.

The diffusion coefficient D for the spatial simulations using the Goldbeter et al. (1990) model was chosen to be consistent with the FHN model, however it is not physiologically accurate for Ca^{2+} diffusion through SMCs even though the Goldbeter model is nondimensional. In reality the diffusion coefficient is likely to be much smaller than the value of $D = 0.12$ used in the majority of our results; such a coefficient would make our simulations more physiologically accurate as the patterns resulting from wave propagation and interaction on a surface with spatially varied local dynamics are dependent on the rate of diffusion.

Our spatial simulations implementing the Goldbeter et al. (1990) model used a linear function for the spatial variation in local dynamics (via the bifurcation parameter β), however it would be interesting to run our simulations with a more realistic parameter distribution. As an example, Zakkaroff et al. (2015) applied the SMC/EC model by Shaikh et al. (2012) (originally based on the model by Koenigsberger et al. (2005)) to the surface of an arterial bifurcation; both a synthetic agonist map of J_{PLC} (based on the wall shear stress) and a computational fluid dynamics (CFD) based J_{PLC} map were used in their simulations.

It would be worthwhile simulating the complex SMC/EC model on a spatial domain, in particular a curved surface since this model includes the influence of neuronal activity on SMC Ca^{2+} dynamics and the brain cortex is a strongly curved medium. As this model contains a total of 14 state variables it is much more complex than the previously simulated Goldbeter et al. (1990) model and any simulations on a 2D spatial domain would most likely require parallel architecture in order to have a feasible runtime. In addition the system is stiff so the full capabilities of the ARKode additive solver could be implemented by partitioning the system equations into 'fast' and 'slow' timescale components, decreasing the runtime. The nonspatial results of a single and coupled system using either the Goldbeter et al. (1990) and SMC/EC models are similar in nature; would this still be true when simulated on a spatial domain?

7.2 Research Summary

The minimal Goldbeter et al. (1990) model of Ca^{2+} dynamics within a SMC produces similar behaviour to that of a more complex and physiologically realistic model of a SMC/EC 'unit' based on the model of a full neurovascular unit (NVU) by Farr and David (2011) and Dormanns et al. (2015). The cell or unit will exhibit excitable, nonexcitable or oscillatory behaviour depending on the rate of IP_3 induced Ca^{2+} release from the internal stores into the cytosol of the cell. However small amplitude oscillations and bistability are found in the SMC/EC model when neuronal activity is high and the rate of IP_3 induced Ca^{2+} release is low; these dynamics are thought to be a result of the stretch activated Ca^{2+} channels not found in the Goldbeter et al. (1990) model.

The behaviour of two coupled cells or SMC/EC units are seemingly model independent; an excitable coupled with an oscillatory cell or two nonidentical coupled oscillatory cells will exhibit qualitatively different behaviour when weakly coupled such as variable amplitude oscillations.

When the Goldbeter et al. (1990) model is simulated on a 2D spatial domain with the local dynamics of the system spatially varied, Ca^{2+} waves are initiated where the domain is oscillatory and propagate where the domain is excitable. The curvature of a spatial domain can have an effect on the local rate of diffusion; positive curvature decreases the rate of diffusion, negative curvature increases the rate of diffusion. This produces a new wave solution of the Goldbeter et al. (1990) model in the form of a propagating wave segment of constant wave size and shape. Wave interaction causing patterns such as spiral waves and seemingly spatiotemporal chaotic behaviour on a spatially varied domain will occur if the diffusion rate is low enough, and either the spatial domain is strongly curved or the ICs are inhomogeneous.

As the single and coupled Goldbeter et al. (1990) model produces similar behaviour to the SMC/EC model based on a NVU, it is possible that the dynamics of the Goldbeter model simulated on both a flat and curved 2D spatial domain may provide some insight into the dynamics of Ca^{2+} wave formation and propagation of the more complex and physiologically realistic SMC/EC model.

Bibliography

Ahrens, J., Law, C., Geveci, B., James Ahrens, and Charles L. B. Geveci (2005). Paraview: An end user tool for large data visualization. *The visualization handbook*, 836:717–731.

Biosa, G., Bastianoni, S., and Rustici, M. (2006). Chemical waves. *Chemistry - A European Journal*, 12(13):3430–3437.

Champneys, A. R., Kuznetsov, Y. a., Paffenroth, R. C., Fairgrieve, T. F., Oldeman, B. E., and Wang, X. (2002). AUTO 2000: Continuation And Bifurcation Software For Ordinary Differential Equations.

Chang, S. J., Tzeng, C. R., Lee, Y. H., and Tai, C. J. (2008). Extracellular ATP activates the PLC/PKC/ERK signaling pathway through the P2Y2 purinergic receptor leading to the induction of early growth response 1 expression and the inhibition of viability in human endometrial stromal cells. *Cellular Signalling*, 20(7):1248–1255.

Dormanns, K., van Disseldorp, E. M. J., Brown, R. G., and David, T. (2015). Neurovascular coupling and the influence of luminal agonists via the endothelium. *Journal of Theoretical Biology*, 364:49–70.

Farr, H. and David, T. (2011). Models of neurovascular coupling via potassium and EET signalling. *Journal of Theoretical Biology*, 286:13–23.

FitzHugh, R. (1961). Impulses and Physiological States in Theoretical Models of Nerve Membrane. *Biophysical Journal*, 1(6):445–466.

Girouard, H. and Iadecola, C. (2006). Neurovascular coupling in the normal brain and in hypertension, stroke, and Alzheimer disease. *Journal of applied physiology (Bethesda, Md. : 1985)*, 100:328–335.

Goldbeter, A., Dupont, G., and Berridge, M. J. (1990). Minimal model for signal-induced Ca2+ oscillations and for their frequency encoding through protein phosphorylation. *Proceedings of the National Academy of Sciences of the United States of America*, 87(February):1461–1465.

Golubitsky, M., Knobloch, E., and Stewart, I. (2000). Target Patterns and Spirals in Planar Reaction-Diffusion Systems. *J. Nonlin. Sci.*, 10:333–354.

Gonzalez-Fernandez, J. M. and Ermentrout, B. (1994). On the origin and dynamics of the vasomotion of small arteries. *Mathematical Biosciences*, 119:127–167.

Gorelova, N. A. (1983). Spiral Waves of Spreading Depression in the Isolated Chicken Retina. 14(5):353–363.

Haddock, R. E. and Hill, C. E. (2005). Rhythmicity in arterial smooth muscle. *The Journal of physiology*, 566(3):645–656.

Hahn, C. and Schwartz, M. A. (2009). Mechanotransduction in vascular physiology and atherogenesis. *Nature reviews Molecular cell biology*, 10(1):53–62.

Hai, C. M. and Murphy, R. A. (1988). Cross-bridge phosphorylation and regulation of latch state in smooth muscle. *American Journal of Physiology - Cell Physiology*, 254(1):C99—-C106.

Hill, D. and Morgan, T. (2014). Pattern Formation and Wave Propagation in the Belousov-Zhabotinskii Reaction. *University of California, San Diego Physics Department 1: 12. Physics 173/BGGN 266.*

Hindmarsh, A. C., Brown, P. N., Grant, K. E., Lee, S. L., Serban, R., Shumaker, D. E., and Woodward, C. S. (2005). SUNDIALS: Suite of Nonlinear and Differential/Algebraic Equation Solvers. *ACM Trans. Math. Softw.*, 31(3):363–396.

Hodgkin, A. and Huxley, A. (1990). A quantitative description of membrane current and its application to conduction and excitation in nerve. *Bulletin of Mathematical Biology*, 52(1-2):25–71.

Kapela, A., Bezerianos, A., and Tsoukias, N. M. (2009). A mathematical model of vasoreactivity in rat mesenteric arterioles: I. Myoendothelial communication. *Microcirculation*, 16(8):694–713.

Kapral, R. (1995). Pattern formation in chemical systems. *Physica D: Nonlinear Phenomena*, 86(1-2):149–157.

Keener, J. P. (1986). A Geometrical Theory for Spiral Waves in Excitable Media. *Society for Industrial and Applied Mathematics*, 46(6):1039–1056.

Kneer, F., Schöll, E., and Dahlem, M. a. (2014). Nucleation of reaction-diffusion waves on curved surfaces. *New Journal of Physics*, 16.

Koenigsberger, M., Sauser, R., Bény, J.-L., and Meister, J.-J. (2005). Role of the endothelium on arterial vasomotion. *Biophysical journal*, 88(June):3845–3854.

Meyer, T. and Stryer, L. (1988). Molecular model for receptor-stimulated calcium spiking. *Proceedings of the National Academy of Sciences of the United States of America*, 85(July):5051–5055.

Milton, J. and Jung, P. (2013). *Epilepsy as a dynamic disease*. Springer Science & Business Media.

Nagumo, J., Arimoto, S., and Yoshizawa, S. (1962). An Active Pulse Transmission Line Simulating Nerve Axon*. *Proceedings of the IRE*, 50(10):2061–2070.

Østby, I., Øyehaug, L., Einevoll, G. T., Nagelhus, E. a., Plahte, E., Zeuthen, T., Lloyd, C. M., Ottersen, O. P., and Omholt, S. W. (2009). Astrocytic mechanisms explaining neural-activity-induced shrinkage of extraneuronal space. *PLoS Comput Biol*, 5(1):e1000272.

Schroeder, W., Martin, K., and Lorensen, B. (2006). *The Visualization Toolkit: An Object-Oriented Approach to 3D Graphics*. Kitware Inc., fourth edition.

Shaikh, M. a., Wall, D. J. N., and David, T. (2012). Macro-scale phenomena of arterial coupled cells: a massively parallel simulation. *Journal of The Royal Society Interface*, 9(70):972–987.

Sinha, S. and Sridhar, S. (2014). *Patterns in Excitable Media: Genesis, Dynamics, and Control*. CRC Press.

Sneyd, J. and Atri, A. (1993). Curvature dependence of a model for calcium wave propagation. *Physica D*, 65(93):365–372.

Walker, D. W. (1994). The design of a standard message passing interface for distributed memory concurrent computers. *Parallel Computing*, 20(1994):657–673.

Weise, L. D. and Panfilov, A. V. (2012). Emergence of Spiral Wave Activity in a Mechanically Heterogeneous Reaction-Diffusion-Mechanics System. *Physical Review Letters*, 108(22):228104.

Wilkins, M. and Sneyd, J. (1998). Intercellular spiral waves of calcium. *Journal of theoretical biology*, 191(3):299–308.

Zakkaroff, C., Moore, S., Dowding, S., and David, T. (2015). 3D time-dependent simulations of Ca 2 + dynamics in coupled arterial cells : a massively parallel implementation. *Submitted for publication*, pages 1–27.